Pretreatments of Al-2024 T3 Alloy for BTSE Silane Deposition

by

Michael Che-Chiang Lee

B.Sc. (Hons), The University of Western Ontario, 1999

A THESIS SUBMITTED IN PARTIAL FULFILLMENT OF

THE REQUIREMENTS FOR THE DEGREE OF

MASTER OF SCIENCE

in

THE FACULTY OF GRADUATE STUDIES

Department of Chemistry

We accept this thesis as conforming

to the required standard

THE UNIVERSITY OF BRITISH COLUMBIA

August 2002

In presenting this thesis in partial fulfilment of the requirements for an advanced degree at the University of British Columbia, I agree that the Library shall make it freely available for reference and study. I further agree that permission for extensive copying of this thesis for scholarly purposes may be granted by the head of my department or by his or her representatives. It is understood that copying or publication of this thesis for financial gain shall not be allowed without my written permission.

Department of CHEMISTRY

The University of British Columbia
Vancouver, Canada

Date 31 July 2003

Abstract

Work in this thesis studied different alkaline etching procedures performed on Al-2024 alloy prior to deposition of bis-triethoxysilylethane (BTSE). X-ray photoelectron spectroscopy and scanning electron microscopy were used to study the chemistry and morphology of the surfaces formed after the various pretreatments and coatings have been applied. The corrosion performance of these samples were assessed using polarisation curve measurements and immersion testing. Sonicating tests were performed to determine, semi-quantitatively, the adhesion of BTSE to Al-2024 panels after application of the various pretreatments.

Alkaline etching of the coated and uncoated Al-2024 panels was performed using 10% NaOH in deionised water, varying the duration of the treatment from 1 minute to 10 minutes. It is shown on uncoated Al-2024 that longer etching times increase surface roughness of the substrate, but also reduce corrosion resistance, cause copper enrichment at the surface, and form loosely-bonded etching products which affect the subsequent silane deposition steps.

BTSE solutions varying from 1% to 10% (v/v) BTSE were used to coat the pretreated panels. It is found that BTSE-coated samples perform better than their uncoated counterparts in corrosion testing, and that more-concentrated BTSE solutions on identically prepared panels produce thicker coatings, with better passivation. It is also found that, while increasing the alkaline etching time may lead to conditions where more BTSE is deposited to the surface, this "enhanced" silane layer is not as securely-bonded to the surface and will not aid in the passivation of the substrate.

Finally, the effects of the HNO_3 desmutting step were studied by varying the treatment times that the Al-2024 panels received in 10% HNO_3 after 1 minute of alkaline etching. It is found that for up to 30 minutes of treatment, HNO_3 is beneficial to silane deposition as it removes the etching product created during the NaOH treatment, builds up the oxide layer and creates more sites for the silane bonding. However, with longer exposure, HNO_3 acts as a corrosion agent removing previously-built oxide layer which reduces the amount of securely-bonded BTSE.

Table of Contents

List of Tables

List of Figures

List of Abbreviations

η	Overpotential
λ	Inelastic mean free path
AE	Alkaline etching
AES	Auger electron spectroscopy
Al-2024	Al-2024 T3 alloy
AMPEL	Advance Materials and Process Engineering Laboratory
γ-APS	γ-Aminopropyltrimethoxysilane
BTSE	Bis-triethoxysilylethane
CAA	Chromic acid anodising
CHA	Concentric hemispherical analyzer
CRT	Cathode ray tube
DND	Department of National Defence
E_{corr}	Free corrosion potential
ESCA	Electron spectroscopy for chemical analysis
FEG	Field-emission electron gun
FWHM	Full-width-at-half-maximum
GNP	Gross national product
γ-GPS	γ-Glycidopropyltrimethoxysilane
i	Current density
i_o	Exchange current density (at equilibrium)
IMFP	Inelastic mean free path
MAX 200	Leybold MAX 200 system

MP	Mechanical polish
PAA	Phosphoric acid anodising
SEM	Scanning electron microscopy
SIMS	Secondary ion mass spectrometry
TEM	Transmission electron microscopy
UHV	Ultra-high vacuum
v/v	Volume by volume (100% (v/v) = 100 mL/100 mL)
VS	Vinyl silane
w/v	Weight by volume (100% (w/v) = 1000 g/1000 mL)
XPS	X-ray photoelectron spectroscopy
ZPO	Zinc phosphating

Acknowledgements

I would like to thank my supervisor, Professor K. A. R. Mitchell, for accepting me to his research group and introducing me to the areas of analytical chemistry and surface science. I am grateful for his sponsorship of this work as well as his invaluable advice and guidance throughout my tenure in his laboratory.

I am especially grateful to Dr. X. Sun for introducing me to the area of corrosion science, for his assistance throughout his tenure in this laboratory, and for the invaluable discussions; to Dr. K. C. Wong for helping with the XPS measurements and interpretations; and to Dr. P. C. Wong for the wonderful discussion of many topics including XPS, surface chemistry, interpretation of results, and experimental design.

I also greatly appreciate the interaction with other members of this group, including: Ms. L. Shi, Ms. R. Li, Ms. D. Susac, Dr. M. Kono, Dr. M. Saidy, Mr. H. Fourtier, Ms. J. Jing, Mr. W. H. Kok, Mr. J. T. K. Kim, Mr. M. Y. C. Teo, and Ms. A. Akhtar.

I am thankful to Professor D. Tromans, Dr. T. M. Ahmed, and Mr. A. Tshilombo for their assistance with the electrochemical polarisation curve measurements. I would also like to acknowledge the guidance of Mr. J. Mackenzie and Mr. A. Schmaltz for the operation of the SEM in Professor Tiedje's laboratory. To Professor D. Bizzotto, for various conversations regarding polarisation curve measurements and electrochemistry.

I am grateful to my friends for their support, friendship, and encouragement during my time of studies here, including: Ms. C. J. Leung, Ms. T. L. Winterbottom,

Ms. A. Wong, Mr. D. Wong, and especially Mr. N. K. Y. Wong for proof reading my thesis. Last, but not least, I would like to thank my family for their support and encouragement throughout my studies. To them, I dedicate this thesis.

Chapter 1 Corrosion and Passivation of Aluminum Alloys

1.1 Introduction

1.1.1 Aluminum

Aluminum is widely distributed in the oxide form called *Alumina* (Al_2O_3). It comprises 15% of the Earth's crust and is second only to silica in abundance. Thus, there is a virtually unlimited supply of aluminum [1.1].

Aluminum was discovered by Sir Humphrey Davy in 1809, but was not isolated as a metal until 1825 by H. C. Oersted. An economical industrial process was found in 1886 when two scientists, Hall and Héroult, independently developed the same electrolytic process to reduce alumina to aluminum metal and this process is still widely used today [1.1].

Aluminum has many properties that make it desirable for applications in the automotive, aerospace, and marine industries. It has a low density (2.7 g/cm^3), good conductivity (thermal and electrical), high ductility, low cost compared to comparable metals due to its abundancy, and the high-purity form of the metal has good corrosion resistance in the ambient atmosphere [1.2]. The corrosion resistance is due to an amorphous oxide layer that naturally forms on aluminum metal upon exposure to atmosphere and this layer is responsible for passivating the metal. However, the oxide layer has a limited thickness (1 – 3 nm) and flaws exist in the natural oxide film, which can act as sites for film breakdown [1.1, 1.3 – 1.5].

1.1.2 Alloys and Alloy Nomenclature

High-purity aluminum generally has insufficient mechanical strength, making it impractical to use for commercial applications. Several treatments are possible to

improve this including cold working, heat treating, and alloying. Alloying implies adding and dissolving one or more dissimilar metals into the aluminum. Major elements used for alloying aluminum include copper, magnesium, silicon, manganese, nickel, and zinc. Aluminum alloys can be classified as *Cast Alloys*, since they are cast directly into their desired forms by one of three methods (sand casting, gravity die casting, or pressure die casting); or the *Wrought Alloys* class, where the alloy is made into ingots or billets. These are then hot or cold-worked mechanically into extrusions, forgings, sheets, foils, tubes, and wires [1.1].

The specifications and properties of aluminum and its alloys are covered by standard codes, which allow standardization for specific applications. This also covers temper designations to signify any cold or heat working applied to the alloy [1.6]. Table 1.1 shows the various classes of wrought and cast alloys. Briefly, these classes are summarized as follows: The high-strength Al-Cu alloys (2000 series), used mainly in the aerocraft industry; Al-Mn alloys (3000 series), used mainly in the canning industry; Al-Mg alloys (5000 series), used for structural and architectural applications; Al-Mg-Si alloys (6000 series), the most common of extrusion alloys, used in the building industry; and finally, the Al-Zn-Mg alloys (7000 series) used mainly in the construction of aerocraft and military vehicles [1.1].

This work uses the wrought alloy Al-2024 T3 (Al-2024). Its composition by weight is 93.5 % Al, 4.4 % Cu, 1.5 % Mg, 0.6 % Mn, and trace amounts of Si, Fe, Zn, Zr, and Cr. The T3 designation indicates that the alloy has been thermally treated after precipitation hardening [1.6].

Table 1.1 Aluminum alloy designation according to the Aluminum Association (AA) designation numbers [1.6]

Wrought Alloy Designations	
Aluminum, 99.00% purity minimum or greater	1xxx
Aluminum Alloys Grouped by Major Alloying Elements	
Copper	2xxx
Manganese	3xxx
Silicon	4xxx
Magnesium	5xxx
Magnesium and Silicon	6xxx
Zinc	7xxx
Other Elements	8xxx
Unused Series	9xxx
Cast Alloy Designations	
Aluminum, 99.00% purity minimum or greater	1xx.x
Aluminum Alloys Grouped by Major Alloying Elements	
Copper	2xx.x
Silicon with Copper and/or Magnesium	3xx.x
Silicon	4xx.x
Magnesium	5xx.x
Zinc	7xx.x
Tin	8xx.x
Other Elements	9xx.x
Unused Series	6xx.x

1.2 Corrosion and Solutions to the Problem

1.2.1 Introduction and Definition

Alloying aluminum may increase the mechanical strength, making it more useful for industry; but the corrosion resistance of the alloy is often decreased substantially. *Corrosion* is defined as the destructive and unintentional oxidation of a metal [1.2]. This process is electrochemical in nature and usually begins at the surface.

Corrosion is a very significant problem in a modern industrial society. An industrial nation spends up to 5% of its GNP for corrosion prevention, maintenance, and replacement of products lost or contaminated by the effects of corrosion. This is just the tip of the proverbial iceberg [1.2]. Other indirect costs such as planning and development, plant shutdowns, and over-design must also be factored into the economic scenario [1.7].

1.2.2 Characteristics of Aluminum Corrosion

The corrosion characteristics of pure aluminum are shown in the potential-pH (E-pH or Pourbaix) diagram seen in Figure 1.1 [1.8]. The Pourbaix diagram shows the thermodynamic stability of a species as a function of the variables plotted. It is used to predict the spontaneous direction of a reaction. Because it is a thermodynamic diagram, the Pourbaix diagram gives no information on the kinetics of a reaction. Lines (a) and (b) are called the *a-line* and *b-line* respectively. They represent the stability of water at 25 °C and 1 atm. of pressure. Below the a-line, water is reduced to H_2; above the b-line, water is oxidized to O_2. The stability region of water in the absence of aluminum is between the a-line and b-line. In Figure 1.1, it is seen that the whole domain of aluminum metal stability lies below that of water. If conditions are sufficiently acidic, the metal will

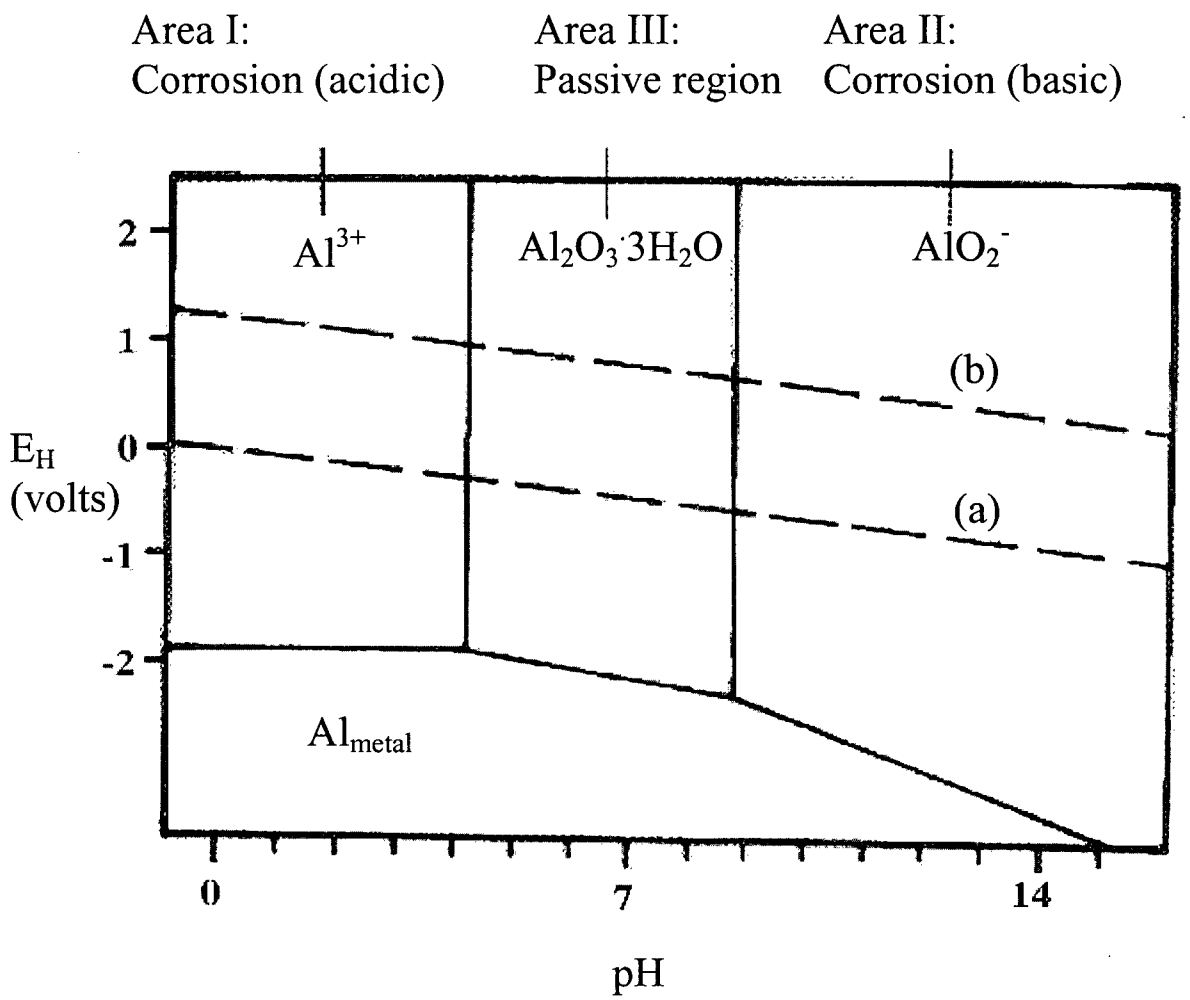

Figure 1.1 Pourbaix diagram for Al-H_2O system at 1 atm. pressure and 25 °C [1.8]

decompose the water with evolution of H_2 and form Al^{3+}, seen in Area I. If conditions are sufficiently alkaline, the metal will decompose the water with the evolution of H_2 and form aluminate ions (AlO_2^-), seen in Area II. A third intermediate condition occurs between pH 4 and 9. In this case, the aluminum becomes covered with an oxide film ($Al_2O_3 \cdot 3H_2O$). This is the natural oxide film mentioned previously. It can act to protect the metal from a surrounding corroding medium and provide kinetic stability. This region is known as the *Passive Region* and is seen in Area III.

The molecular volume of the oxide film is stoichiometrically 1.5 times that of the metal. This results in the oxide film being under compressive stress, but, in practice, some deformation can occur before rupturing [1.1].

Breakdown of the oxide film can result from mechanical rupture or chemical attack via anions. It has been proposed that, in solution, flaws in the oxide layer are continuously being developed and repassivated. Corrosion of aluminum can occur when the oxide film is damaged or removed and the surrounding conditions prevent the reformation of this protective oxide film, allowing attack on the exposed metal. It has been suggested that the presence of aggressive ions such as Cl^- may hinder the repassivation of the oxide layer, allowing corrosion sites to be generated on the exposed metal. Further, electrochemical and microscopic studies have demonstrated that pre-existing flaws in the oxide film can act as nucleation sites for film breakdown [1.1, 1.3 - 1.5].

One mechanism proposed for the alloying element to lower the corrosion resistance involves galvanic coupling. As observed in Al-2024, because copper is a more noble metal relative to aluminum, this causes the preferential dissolution of aluminum

metal [1.7]. A second mechanism suggested for the poor corrosion performance of alloys involves the differences in the properties and thickness of the oxide film on the alloy compared to more pure forms of the metal. It has been shown that the oxide layer above the second-phase particles (compounds containing Al-Cu-Mg, and Al-Cu-Fe-Mn-Si, for example) in this alloy may be thinner or non-existent, which leaves these areas more prone to attack [1.9,1.10].

1.2.3 Solutions to the Problem

As the corrosion of metal represents a big challenge in modern industry and society, much research has aimed at developing methods for corrosion inhibition. Several solutions currently exist such as (i) Cathodic protection, or lowering the potential sufficiently, so that corrosion will not occur according to the Pourbaix diagram either by placing the system in the stable region or placing it in the passive region; (ii) Using sacrificial anodic coatings, such as metal sprays like zinc; or painting to protect the metal surface from being exposed to a corrosive environment; (iii) Anodising, which artificially builds a thicker, but porous, passive oxide layer that acts similarly to the natural oxide layer of the metal; and (iv) Chemical conversion coatings involving simple chemical treatments to build protective coatings. Traditionally, these conversion coatings are made from chromate solutions to form Cr(VI) and Cr(III) moieties on the surface, although newer methods involve using phosphate-based solutions to form phosphate coatings [1.1].

Unfortunately, these solutions may not be acceptable in practical applications for various reasons. While cathodic protection of a metal surface is effective and environmentally friendly, creating little or no waste products, it is too expensive to

supply the electric current for large exposed samples, so making it impractical for commercial applications. Painting metals, or using sacrificial coatings, not only serves as an esthetic treatment of the metal, but also serves to form a coating or barrier against the elements of corrosion. However, if the metal is not pre-treated sufficiently to accept the coating, the coating will be poorly bonded to the metal surface making it ineffective as a corrosion inhibitor. Anodising gives thicker, but more porous, oxide layers which have to be plugged. Chromic acid anodising (CAA) as well as phosphoric acid anodising (PAA) have been very successful as corrosion inhibitors and aiding as primers in paint adhesion, solving the primer problem mentioned above as the chromium-containing complexes are excellent sealants and bond well with paint. These methods are currently used in the automobile industry [1.11 – 1.13]. Similar solutions for the problems with paint adhesion have been achieved with chromate and phosphate-based conversion coatings. However, all four methods make use of chromium-containing complexes, either as the primary step, or as a sealant in subsequent steps. Stricter environmental laws concerning the waste and disposal of hard metals, and the toxic and carcinogenic effects of the Cr(VI) species have spawned a desire to search for an effective, yet more environmentally-friendly alternative to the current CAA and PAA processes used [1.14].

Our laboratory has been working on zinc-phosphate (ZPO) processes for several years in conjunction with the Department of National Defence (DND) to develop alternative coating processes in attempts to minimize the amount of chromium used in these processes [1.15 – 1.20]. There has also been a push to find organic alternatives as certain painting processes may be more effective when the paint is applied to organic functional groups rather than to inorganic salts, and forego the chromating steps

completely. Over the past several years, organofunctional silanes, which are well known as coupling agents for metals, have been given more consideration as a "green" corrosion inhibitor alternative [1.21 – 1.29]. These organofunctional silanes are known as *Silane Coupling Agents* or *Silanes*. This thesis will describe new research directed at using a silane as a corrosion inhibitor for Al-2024.

1.3 Silane Coupling Agents

1.3.1 Definition and Basic Properties

Coupling Agents are defined as materials that improve the chemical resistance (especially to water) of the bond across the interface [1.30 – 1.32]. Silane coupling agents are molecules that often have the formula of type: Y-R'-Si-$(OR)_3$ when they are monofunctional i.e. having only one silicon moiety. Y is an organofunctional group, R' is a hydrocarbon link, and OR are hydrolysable alkoxy groups, which upon contact with water will produce silanol (Si-OH) groups as seen in Figure 1.2. Although the mechanism is not fully understood, the generally accepted theory suggests that these silanol groups form direct chemical bonds with metal hydroxide groups present in the metal oxide via condensation reactions [1.30 – 1.32]. The silicon moiety gives the metal-bonding ability as well as the possibility for polymerization via condensation of excess silanol groups not bonded to the metal. The more silanol groups the hydrolyzed silane has, the better the possibility for stronger adhesion of the silane to the metal.

It is desired that the silanol groups are the functional groups which interact with the metal oxide surface, leaving the Si-R'-Y side of the silane to be free to react in subsequent steps such as adding a second silane or painting [1.33]. This is known as

1. Hydrolysis of silane:

$$(OR)_3—Si—R'Y + 3\ H_2O \rightarrow (OH)_3—Si—R'Y + 3\ ROH$$

2. Condensation bonding and polymerization of silane to free hydroxyls in oxide layer:

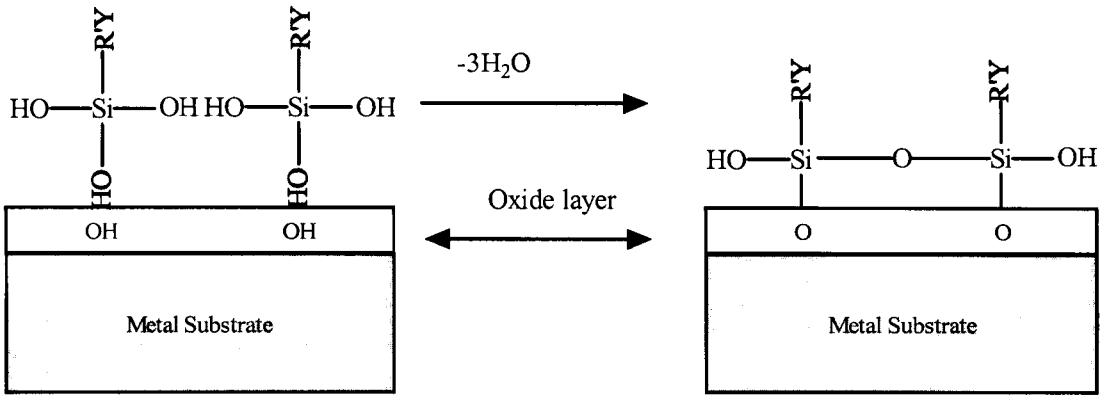

Figure 1.2 Proposed mechanism for silane bonding

Right-Side-Up bonding and is seen in Figure 1.2. *Upside-Down* bonding occurs when the organofunctional group Y is bonded to the metal oxide, leaving no functional group other than the silanol groups for further reaction [1.34]. It is not known whether other bonding motifs, such as a bound Si atom having more than one Si-O-Metal interaction, exist.

Silanes with varying Y groups may be chosen for subsequent steps. Examples of different silanes are shown in Table 1.2. If an appropriate functional group is chosen, it may participate in further bonding with other silanes, producing a more cross-linked film which aids in the hydrophobic properties of the silane film. It may also bond with paints in subsequent steps.

1.3.2 History and Applications

There is a long history of considering the binding of two dissimilar materials, with philosophical thoughts recorded by Plato [1.35]. Organosilanes first received attention as coupling agents in the 1940's when there was a major need for new techniques to bond glass fibers as reinforcements in organic resins. A water-resistant bond was needed. In 1947, Witt and co-workers submitted a report to the U.S. Navy Bureau of Ordnance observing that allyltriethoxysilane on glass fibers gave polyester composites with twice the bond strength of those fibers treated with ethyltrichlorosilane [1.31]. In 1962, it was found that the effectiveness of the silane as a coupling agent paralleled the reactivity of its organofunctional group with the resin [1.36].

Since then, many papers have been published on the subject of silanes for the role of a coupling agent or a primer for painting [1.37 – 1.47]. However, it was not until the early 1990's that silanes were considered as corrosion inhibitors for metals. This idea

Table 1.2 Representative silane coupling agents

Monofunctional silanes		
Organofunctional group	Name	Chemical structure
Vinyl	Vinyl silane (VS)	$CH_2=CHSi(OC_2H_5)_3$
Epoxy	γ-Glycidopropyltrimethoxy silane (γ-GPS)	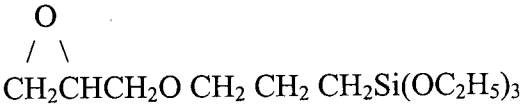
Primary amine	γ-Aminopropyltrimethoxy silane (γ-APS)	$H_2N\ CH_2\ CH_2CH_2Si(OC_2H_5)_3$
Phenyl	Phenyl silane	$C_6H_5Si(OCH_3)_3$

Bisfunctional silanes		
Organofunctional group	Name	Chemical structure
--	Bis-triethoxysilyl ethane (BTSE)	$(H_5C_2O)_3SiCH_2CH_2Si(OC_2H_5)_3$
Amine	Bis-(triethoxysilylpropyl) amine (BTSPA)	$(H_5C_2O)_3Si(CH_2)_3NH(CH_2)_3Si(OC_2H_5)_3$
Sulfur	Bis-(triethoxysilylpropyl) tetrasulfide (BTSPS)	$(H_5C_2O)_3Si(CH_2)_3S_4(CH_2)_3Si(OC_2H_5)_3$

depends on fine-tuning the nature of the silane to create a well-bonded, hydrophobic, cross-linked barrier, which can protect the metal in an aqueous environment. Much of this work has been done primarily on hot-dipped steel, galvanised steel, iron, zinc, and various alloys of aluminum using monofunctional silanes such as γ-APS and γ-GPS [1.48 – 1.52]. Early results have been mixed as to the effectiveness of these coatings for the corrosion inhibition of metals, as it depends not only on the choice of silane used, but also on the choice and state of the metal being coated [1.53]. However, there have been reports that show that certain metal/silane combinations are promising and that they may even rival the durability of current chromating processes [1.54]. In this thesis, bis-triethoxysilylethane (BTSE) is examined as a corrosion inhibitor on Al-2024.

1.3.3 BTSE

The structure of BTSE is $(H_5C_2O)_3SiCH_2CH_2Si(OC_2H_5)_3$ [1.55]. The monomer is bi-functional i.e. it has two silicon moieties. Because of its bis-functionality, lack of traditional organofunctional group Y, and the presence of six silanol groups in the hydrolyzed form, it is a much stronger acid than the monofunctional silanes that obey the formula $Y\text{-}R'\text{-}Si(OR)_3$ [1.33, 1.56]. This may help form more covalent bonds with the metal. As well, due to the six possible silanol groups present after hydrolysis, further cross-linking between the monomer units may result in a less-porous film, with better water-resistance. These six silanol groups may also be available for bonding to a second silane having an organofunctional group Y which may not have been strongly adhered to the substrate on its own [1.33, 1.56]. Based on the nature of the silane itself, however, it has been demonstrated that BTSE alone may be sufficient to act as an inhibitor [1.49, 1.50, 1.53, 1.54, 1.56].

1.4 Pretreatment of the Substrate Surface

1.4.1 Introduction

Before any coating can be applied to a metal substrate, the substrate must be sufficiently pretreated i.e. it must be cleaned and prepared to receive the coating and ensure durable bonding to the substrate. Surface contamination has been shown to cause problems with the durability of this bond [1.57 – 1.59]. A pretreatment can build up a fresh, uncontaminated oxide layer [1.1]. A pretreatment may also serve to change the morphology of the surface, making the surface rougher, which may aid the mechanical interlocking of a subsequent coating [1.52, 1.60].

In addition to the flaws that pre-exist in the thin, natural-borne oxide, Wernick and Pinner, as well as Kozma, have also suggested that the original oxide layer is not conducive for the bonding of organic coatings, as it is usually amorphous with few metal hydroxide sites. A pretreatment is generally needed to increase the number of metal hydroxyls on the surface [1.1, 1.61]. This can involve chemical, mechanical, electrochemical means, or a combination of the three [1.62]. All may serve to clean any contamination off the surface and alter the oxide layer to make it more suitable for bonding. The literature contains various descriptions of pretreatments for metals and alloys, with some specifically for Al-2024 [1.62 – 1.64].

1.4.2 Alkaline Etching

Mechanical polishing is used to create a microscopically rough surface which is shown to create a large surface area that may improve adhesion, and is frequently used prior to any chemical etching [1.65]. According to van Ooij and co-workers, additional

steps prior to silane deposition are essential for the above-mentioned reasons, but most importantly for creating free hydroxyls for optimum silane bonding [1.33, 1.56, 1.57].

Alkaline etching, in general, increases surface roughness. Van Ooij has claimed that it also increases the amount of free metal basic hydroxyls compared to other forms of metal pre-treatment such as acidic or neutral chemical cleaners [1.33, 1.56]. These hydroxyls are believed to be necessary for silane bonding according to Pape and Pluddemann [1.30 – 1.32]. The current literature reports various times and concentrations that panels be placed in the NaOH solution when etching is performed [1.1, 1.66, 1.67]. However, no standard time, or concentration is set, nor have the effects of longer alkaline etching times on the metal been documented.

As well, Hulser and Ijomah have both suggested that etching products are created after the NaOH step in the alkaline etching pretreatment according to the reaction [1.66, 1.67]:

$$2\ Al + 2\ NaOH + 2\ H_2O \rightarrow 2NaAlO_2 + 3\ H_2 \qquad (1.1)$$

AlO_2^- in solution can then react with water or acid to form one of the two following forms of etching product:

$$2\ NaAlO_2 + 4\ H_2O \rightarrow 2\ Al(OH)_{3\,(s)} + 2\ NaOH \quad \text{(in alkaline media)} \qquad (1.2)$$

or

$$AlO_2^- + H_3O^+ \rightarrow AlOOH_{(s)} + H_2O \quad \text{(in acidic media)} \qquad (1.3)$$

Both forms of etching product contain the OH group, required for silane bonding, and are also known to be poorly-bonded to the surface. Hulser has suggested that the etching product is a site of nucleation for a coating, rather than the substrate oxide layer [1.66].

The alkaline etching pretreatment suggested for silane deposition has advantages and disadvantages. While this process may be necessary to create free hydroxyls needed for bonding, and to increase the total surface area, it may have the side effect of creating etching products that may create a poorly-bonded silane film. If this method of pretreatment is to be used, it must be optimized so that a maximum number of metal hydroxide groups, in the substrate oxide layer, can be created while limiting the amount of etching product formed.

1.5 Objectives and Aims of This Thesis

The purpose of this work stems from the need to develop basic knowledge about the effects of alkaline etching pretreatments on Al-2024 alloy prior to silane deposition for corrosion inhibition. Van Ooij and co-workers have started research using BTSE as a corrosion inhibitor and have demonstrated, using electrochemical and salt-spraying tests, its potential as an alternative to chromating methods. However, their studies had an engineering perspective and did not provide information about the effects of pretreatment, cleaning, and optimization of any pretreatment methods specifically for silane deposition. In addition, there is no information in the literature on the effects of alkaline etching time, or the effects of each step in an alkaline etching procedure for silane deposition, to support Van Ooij's claim that the alkaline etching method for metal pretreatment is essential in creating the free hydroxyl groups needed for silane bonding [1.33, 1.56, 1.57].

The work in this thesis investigates steps in an industrial-style alkaline etching procedure in relation to silane deposition onto Al-2024. Characterizations are made by X-ray photoelectron spectroscopy and scanning electron microscopy. These surface

chemical techniques give chemical information and visual records of the surfaces involved. In addition, techniques used in corrosion engineering such as polarisation curve measurements and immersion testing are used to evaluate the corrosion performance of samples after various pretreatments and processes. The background to the instrumentation used in this thesis is discussed in Chapter 2.

Chapter 3 discusses three sets of measurements. The first discusses the effects of various alkaline etching conditions on polished, uncoated Al-2024, with an emphasis on how etching time affects the chemical nature, morphology, and corrosion performance of the metal. This information is needed in order to gain additional understanding for the observations made by Van Ooij regarding substrate preparation and the effects on subsequent deposition steps [1.33, 1.56]. The various characterization techniques discussed in Chapter 2 are employed here to investigate these claims. The second set of measurements study the effects of silane solution concentration on the corrosion resistance of the treated alloy and on the silane film thickness. Finally, the interrelationships of alkaline etching times and silane solution concentration are studied to observe the effects on the silane deposition and corrosion performance of the coated samples.

In Chapter 4, the effects of nitric acid used during the alkaline etching procedure are studied, by varying the treatment time, to see the effects it has on the bonding durability of the silane.

Chapter 5 summarizes conclusions from this research, and addresses possible future directions.

Chapter 2 Instrumentation

2.1 X-Ray Photoelectron Spectroscopy (XPS)

2.1.1 Introduction

X-Ray photoelectron spectroscopy (XPS), also known as electron spectroscopy for chemical analysis (ESCA), is one of the most versatile and widely used techniques for the chemical analysis of materials. Its popularity as a technique for surface analysis is due to the high information content, its flexibility in accepting a wide variety of sample types, and a sound theoretical basis for its operation [2.1]. XPS obtains the chemical information desired by using X-rays to eject electrons from core energy levels in the material via the photoelectric effect. An example is shown in Figure 2.1 (a). Electrons from different energy levels of atoms within the material will leave the sample with different kinetic energies, which are measured by the spectrometer. An XPS spectrum is commonly presented as a plot of photoelectron intensity versus binding energy for the electrons inside the sample.

XPS can provide quantitative as well as qualitative information for all chemical elements (except H and He) in the surface region of any material that is stable within a vacuum, or can be made as such. Besides the chemical composition of a sample, information about the organization of atoms on the surface can also be obtained [2.1 – 2.4].

2.1.2 Basic Principles

An explanation of the photoelectric effect is essential to understand XPS.

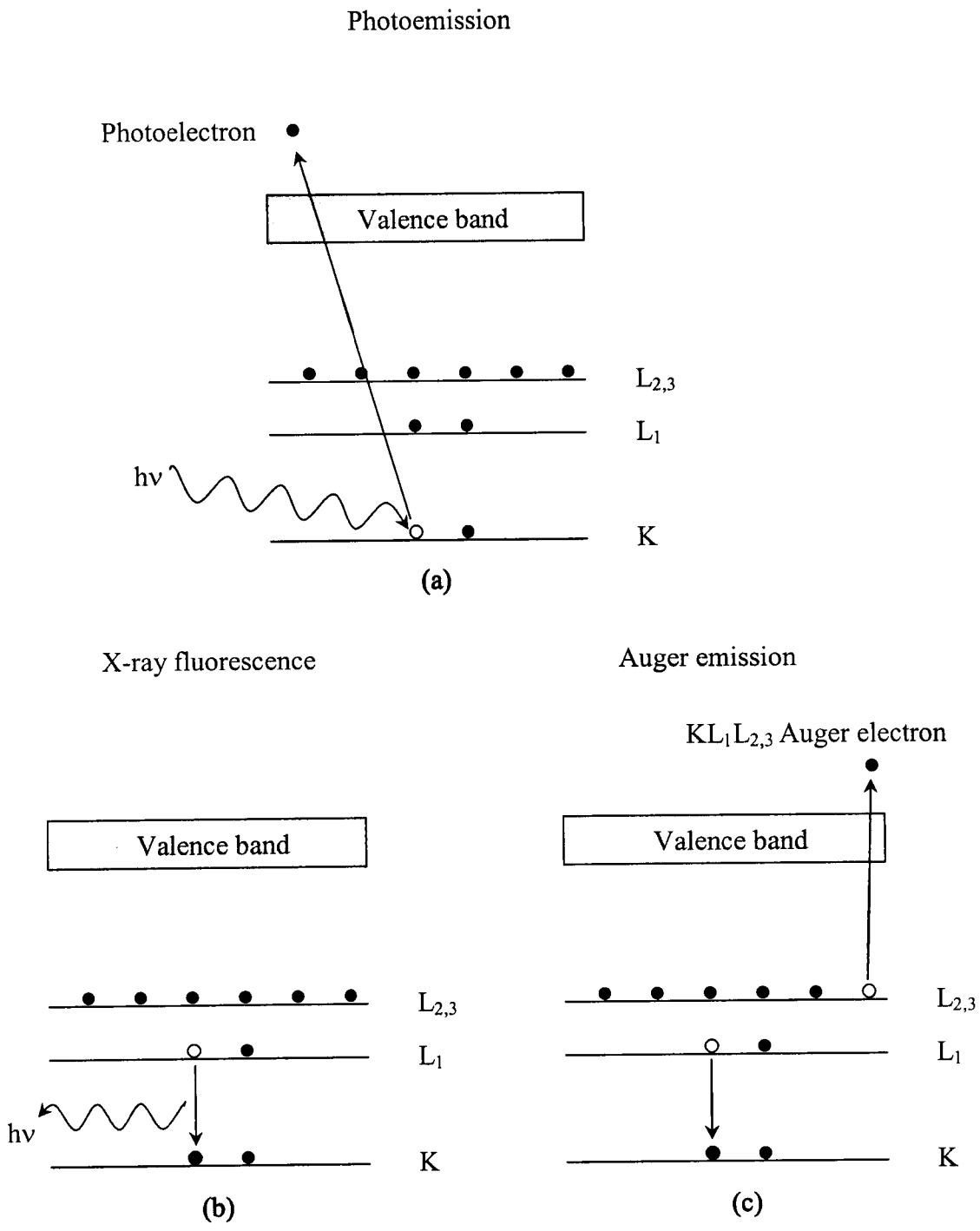

Figure 2.1 Schematic diagram for (a) the photoelectric effect (b) X-ray fluorescence and (c) emission of an Auger electron

Figure 2.1 (a) schematically shows the emission of photoelectrons from a solid as a result of the transfer of energy from impinging X-rays to electrons inside the sample being analyzed. A key equation is:

$$E_k = h\nu - E_b \qquad (2.1)$$

where E_k is the kinetic energy of the ejected photoelectron, $h\nu$ is the photon energy of the X-ray source, and E_b is the binding energy of the electron of interest [2.1, 2.3, 2.4]. The binding energies measured are characteristic of specific atoms and will usually increase as the atomic number (Z) of an atom increases. This is the basis for the use of XPS in qualitative analytical work.

Since the energy levels occupied by the electrons are quantized, the photoelectrons have a kinetic energy distribution N(E) which consists of a series of discrete bands that reflect the orbital structure of the sample. Small variations of the binding energy for a core electron of a particular atom, by up to 5 eV, may occur as a result of changes in the valence electronic structure in different chemical environments. These effects do not affect use for qualitative analysis, but they can provide additional information about the specific chemical bonding of the atom concerned [2.4].

After a photoelectron is ejected, the ion created by the photoelectric process is in an excited state. The excited ion can dissipate its excess energy through one of two processes: (i) photon emission (e.g. X-ray fluorescence); or (ii) ejection of an Auger electron. These processes are illustrated in Figures 2.1 (b) and (c), respectively. These two relaxation processes compete and their relative probabilities vary with the atomic number of the atom involved as well as with the binding energy associated with the core

vacancy. However, Auger emission dominates when the initial binding energy is 2 keV or less; indeed, for elements of low atomic number, the Auger process is always more probable than photon emission [2.5, 2.6].

The Auger process is illustrated in Figure 2.1 (c). It is a two-electron process that follows from the initial ionization of a core electron. To a first approximation, the kinetic energy of an Auger electron is given by:

$$E_{KL_1L_{2,3}} = E_K - E_{L_1} - E_{L_{2,3}} \qquad (2.2)$$

where E_K, E_{L_1}, and $E_{L_{2,3}}$ are the binding energies for the levels involved in the example illustrated in Figure 2.1 (c). Kinetic energies of Auger electrons are independent of the excitation source as they are characteristic solely of the binding energies involved. That is, each element has its own set of Auger electron kinetic energies determined from Equation (2.2). As such, Auger lines, seen in an XPS spectrum, can also serve to provide chemical information.

2.1.3 Instrumentation

Figure 2.2 shows a schematic diagram for the layout of the Leybold MAX 200 instrument used for this research [2.7]. The important components of this system include (i) a vacuum pumping system; (ii) a sample manipulator and transfer system; (iii) an X-ray source; and (iv) an energy analyzer system.

A vacuum environment is needed when using XPS to ensure that the photoelectrons reach the detector while meeting as few gas molecules as possible to avoid scattering and subsequent loss. As well, since XPS is a surface-specific technique, it is important that the sample surface maintains a constant state while a measurement is made. From the Kinetic Theory of Gases, it has been shown that one monolayer of

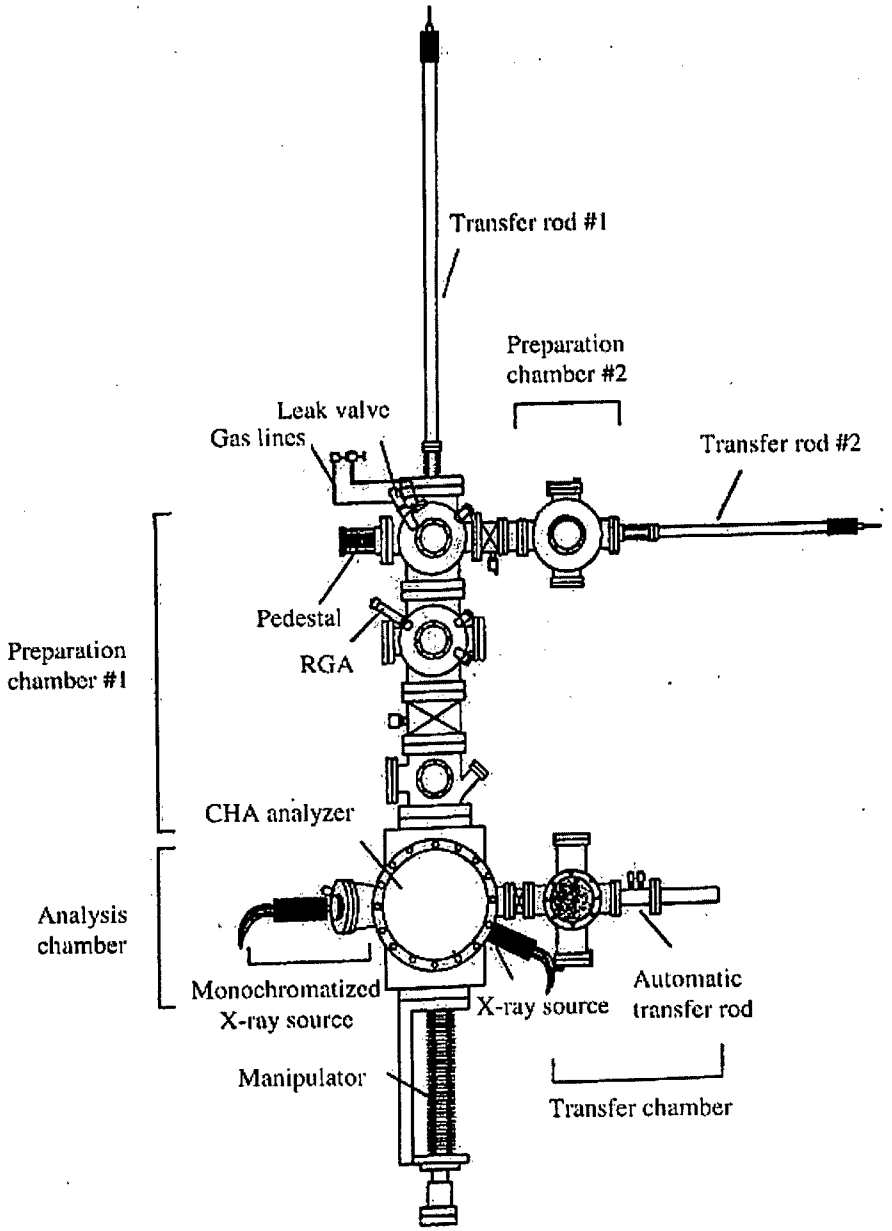

Figure 2.2 Layout of the Leybold MAX 200 XPS system

contamination can cover a surface in 3 s at 10^{-6} torr, assuming each molecular collision results in surface adsorption. This emphasizes the need for pressures in the *Ultra-High Vacuum* (UHV) range (i. e. 10^{-9} torr or less) as the measurements are made [2.5, 2.6].

Samples analyzed in this system are mounted on sample holders using copper tape. The holders are then placed in the transfer chamber. The pressure in the transfer chamber is reduced by the combination of rotary and turbomolecular pumps to around 10^{-7} mbar or less, although a base pressure of around 2×10^{-8} mbar can be obtained with sufficient pumping.

Samples are transferred one by one into the main analysis chamber via an automatic transfer rod. The main analysis chamber is pumped by a turbomolecular pump, backed by a rotary pump. An auxiliary titanium sublimation pump is also present. The analysis chamber has a working pressure of around 10^{-9} mbar, though a base pressure of 2×10^{-10} mbar can be achieved by baking the UHV system from time to time at around 120 °C for 24 hours or more. An ion pump is used for the X-ray source.

The sample holder locks on to the PTM 60 manipulator dock. This provides three linear (x, y, and z) degrees of movement, as well as two rotational degrees of movement, so allowing the sample to be appropriately positioned for analysis.

X-rays are required to create the photoelectrons used for chemical analysis. The Leybold MAX 200 system used for the work in this thesis is equipped with a dual-anode X-ray source which can provide unmonochromatized Kα X-rays using Al or Mg as a source anode. These photons have energies of 1486.6 eV and 1253.6 eV, for Al Kα and Mg Kα respectively; and corresponding linewidths of 0.85 eV and 0.7 eV [2.5]. A simple switch allows for transfer from one source to the other. Because of its higher energy, the

Al Kα source is more frequently used, since it provides spectra with a wider energy range. However, for higher energy resolution, the Mg Kα anode or a monochromatized Al Kα source can be used. Another advantage to having the dual-anode source for XPS analysis is that chance overlap of Auger and XPS peaks can be easily removed.

The X-ray source must be compact enough so that maximum power dissipation can be achieved, while simultaneously allowing the water coolant to remove the heat generated efficiently to avoid any chance of the anode melting [2.5]. The anode is composed of a thick film of source metal on a copper block, and the X-rays produced pass through a thin window of Al foil, which screens stray electrons and contamination from reaching the sample.

A non-monochromatized X-ray source will emit a broad range of radiation known as *Bremsstrahlung Radiation* in addition to the radiation of interest. The Bremsstrahlung radiation can help to reduce charging problems at the sample. However, it necessarily gives lower resolution compared with a monochromatized radiation source.

Figure 2.3 schematically indicates the concentric hemispherical analyzer (CHA) used in the Leybold MAX 200 system to measure the energies of electrons emitted from a sample. This electrostatic analyzer consists of two metal hemispheres and includes collection lenses and a multichannel plate detector. The CHA is a dispersive analyzer where the electrostatic field will only allow electrons within a narrow energy range to reach the detector. The collection and focusing of the photoelectrons towards the entry slit is done in two stages by ramping the voltages on the lens elements. The first stage controls the analysis area (spot size), as well as the collection angle for the electrons coming from the surface of the sample. The second stage is used to retard the electrons to

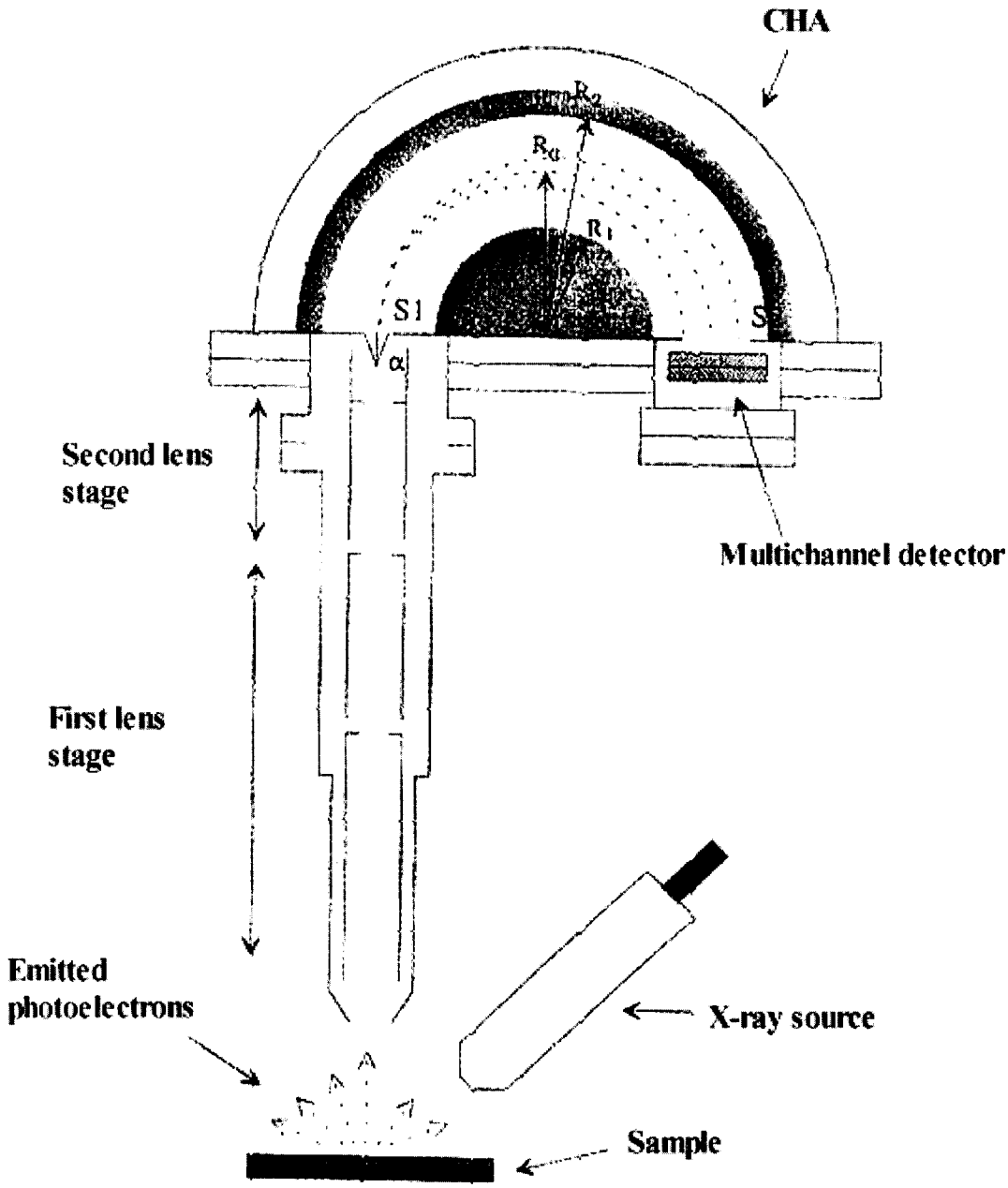

Figure 2.3 CHA energy analyzer and lens system for the Leybold MAX 200 [2.11]

the desired pass energy. It also controls the angle (α) at which the electrons enter the analyzer.

Electrons traveling through the entrance slit can reach the detector only if their kinetic energy (E_o, the pass energy), inside the analyzer satisfies:

$$e\Delta V = E_o(R_2/R_1 - R_1/R_2) \qquad (2.3)$$

where (ΔV) is the potential difference applied between the two concentric hemispheres having fixed radii R_1 and R_2 [2.5]. The MAX 200 can be set for the particular pass energies 24, 48, 96, and 192 eV. The relative analyzer resolution ($\Delta E_{analyzer}/E_o$) is a function of the aperture size, the electron entrance angle, and the electron trajectory radius (R_o). However, these are all constant for a given analyzer setting. Thus, a better energy resolution is obtained if a lower pass energy (E_o) is selected. A trade-off occurs because a lower pass energy chosen will reduce the signal intensity. To obtain an optimum balance between resolution and intensity (counts per second), an appropriate pass energy should be chosen for each type of measurement. For the work done in this thesis, a pass energy of 192 eV was used for survey scans, while 96 eV was used for the higher-resolution scans.

The energy resolution for a peak (ΔE_{peak}) in a measured spectrum is expressed in terms of the full-width-at-half-maximum height (FWHM). This measurement contains contributions from three sources, namely, the analyzer ($\Delta E_{analyzer}$), the natural line width of the X-ray source (ΔE_{source}), and the inherent line width of the atomic level involved (ΔE_{line}). These contributions satisfy:

$$\Delta E_{peak} = (\Delta E_{analyzer}^2 + \Delta E_{source}^2 + \Delta E_{line}^2)^{1/2} \qquad (2.4)$$

provided they all have the Gaussian form [2.5].

Figure 2.4 shows the energy levels for a conducting sample that is in good electrical contact with the spectrometer as well as defining several terms. For a metal sample, the highest occupied energy level, at 0 K, is defined as the *Fermi Level*, while the *Vacuum Level* is the energy of an emitted photoelectron that is at rest just on the vacuum side of a sample. Corresponding levels are also shown for the spectrometer. With good electrical contact, the Fermi levels of the sample and spectrometer are equal, and the binding energy of the sample can be related to the kinetic energy measured by the spectrometer ($E_{k'}$) as follows:

$$E_b = h\nu - E_{k'} - \phi_{sp} \qquad (2.5)$$

ϕ_{sp} is known and is constant for measurements on different samples, although it must be redetermined each time the spectrometer has been exposed to atmospheric pressure. $E_{k'}$ is referenced to the vacuum level of the spectrometer.

Values of binding energies reported in this thesis were referenced to the Au $4f_{7/2}$ peak at 83.8 eV. This peak is chosen because of its high intensity and accurately known position; also, being an inert metal, its binding energy should not be influenced by chemical shifts nor by charging effects. However, the situation is more complicated for a non-conducting sample as it may no longer be in electrical contact with the spectrometer, and then the model shown in Figure 2.4 no longer applies. Real samples, however, always contain some hydrocarbon contamination from the atmosphere. A common approach is to take advantage of this contamination and to calibrate the spectrum by fixing the C 1s peak associated with this contamination at 285.0 eV.

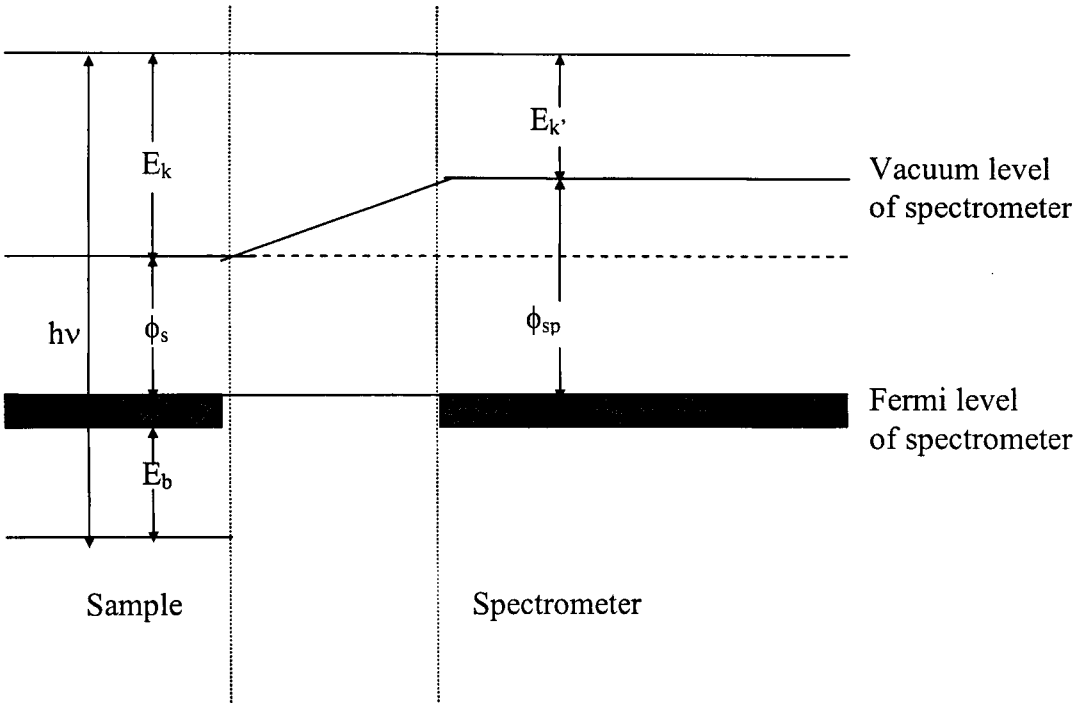

$h\nu$ = Energy of photon

ϕ_s = Work function of sample (i.e. energy difference between Fermi level and Vacuum level)

E_k = Kinetic energy of photoelectron with respect to Vacuum level of sample

E_b = Binding energy of electron in solid with respect to Fermi level

ϕ_{sp} = Work function of spectrometer

$E_{k'}$ = Kinetic energy of photoelectron measured by spectrometer

Figure 2.4 Energy levels for XPS measurements for a conducting sample

2.1.4 Spectral Features

An XPS spectrum is commonly displayed as a plot of intensity (i.e. counts per second) versus binding energy. Measured kinetic energies are converted to the binding energies with Equation (2.5). An XPS analysis is typically performed by first taking a survey scan spectrum which covers an energy range of approximately 1000 eV or more. Figure 2.5 (a) shows a survey scan of a copper sample measured with a high pass energy to identify the elements present [2.3]. Elements of special interest can be studied further with a higher-resolution spectrum measured over a narrower energy range with a lower pass energy. Such a spectrum, typically covers about 10 - 20 eV, and an example is seen in Figure 2.5 (b) [2.1, 2.3].

Peaks in an XPS spectrum can be classified into three types: (i) peaks due to photoemission from valence levels; (ii) peaks due to photoemission from core levels; and (iii) peaks due to Auger electron emission. The low-intensity features seen with binding energies between 0 and 30 eV are due to photoemission of valence electrons (Figure 2.5 (a)). The interpretation of these features may be complex, and this work entirely emphasizes structure from core levels [2.1].

Core-level peaks often reveal the electron orbital structure directly. For the copper example, the 2p, 3s, and 3p levels can be seen in Figure 2.5 (a). In addition, the Auger emissions can also be detected in the survey scan. At higher resolution, doublet structure is observed for states with non-zero orbital angular momentum such as the p and d core levels, due to spin-orbital coupling. Figure 2.5 (b) shows the case for the Cu $2p_{1/2}$ and Cu $2p_{3/2}$ components of such a doublet structure, where the components are characterized by j values.

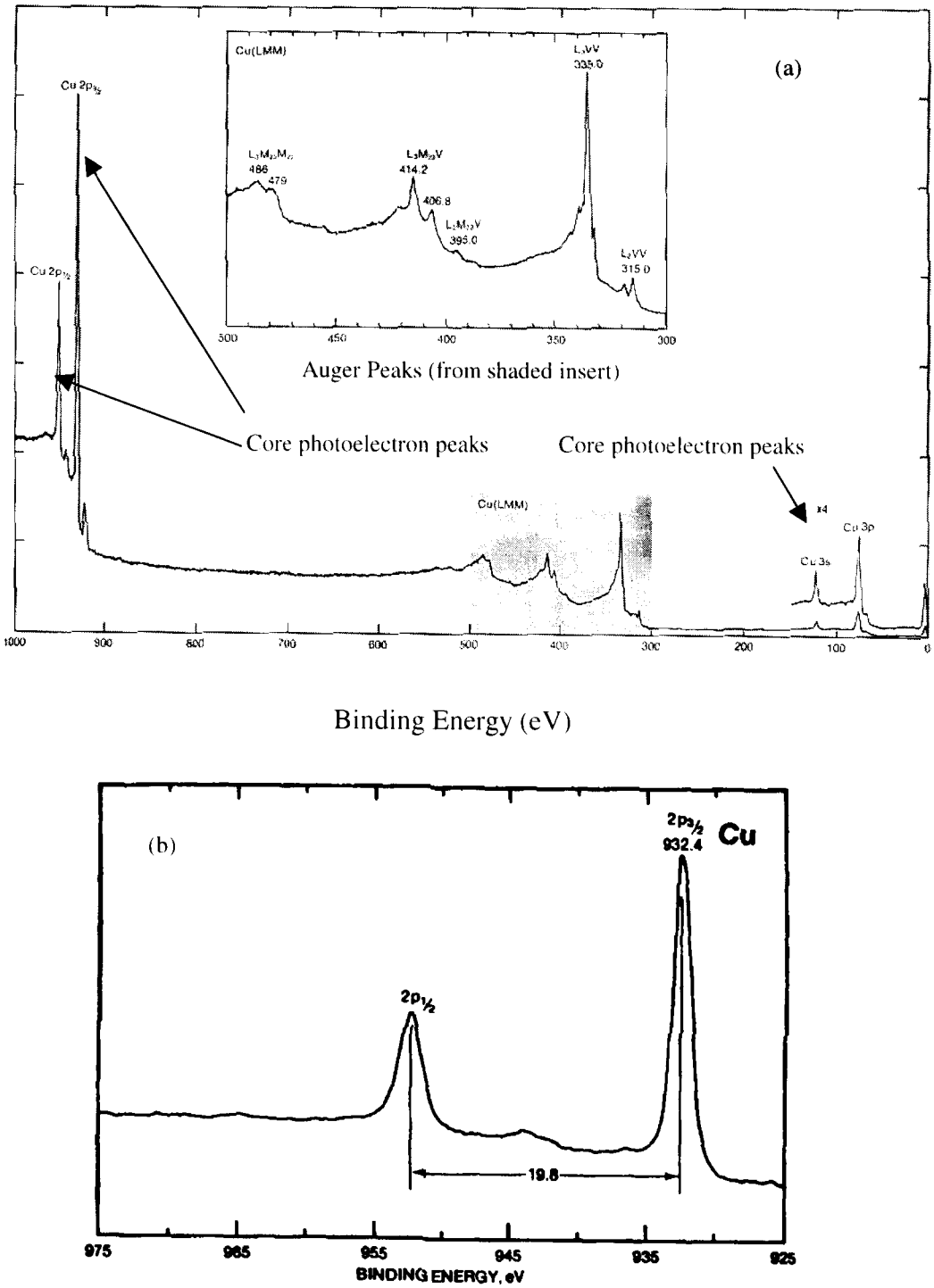

Figure 2.5 XPS spectra of copper excited by Mg Kα radiation [2.3]

(a) Survey scan; (b) Higher-resolution scan of Cu 2p region

2.1.5 Quantitative Analysis

During a measurement, incident photons can penetrate deeply into the solid (e.g. in the μm range), but the photoelectrons emitted from much of this region cannot contribute to the sharp peaks in a spectrum. This is because these electrons have a high probability to lose energy while traveling through the solid. Such electrons contribute to the background or tails of the main signal peaks. The inelastic mean free path (IMFP, or λ) is defined as the mean distance traveled by an electron in the solid without losing energy [2.6]. The IMFP is energy dependent. This can provide information on the sampling depth of the XPS technique. Conventionally, the sampling depth of XPS is taken to equal 3λ, which is the depth from which 95% of the signal in a sharp peak has originated. Empirical values of λ have been reported by Seah and Dench [2.1, 2.7], and Figure 2.6 shows the dependence of this parameter on energy for different materials [2.8, 2.9]. For electron kinetic energies in the range 100 eV to 1500 eV, as used in XPS, λ is generally around 5 to 20 Å. These values indicate that XPS generally probes the top 15 – 60 Å of a sample. This indicates the sense in which XPS (as well as AES) is considered to be a technique that is surface sensitive.

A photoelectron peak intensity consists of the area under the photoelectron peak and can be calculated as follows. The intensity contribution from an infinitesimal thickness (dx), at depth x, in a homogeneous sample can be described by [2.10, 2.11]:

$$dI = f\sigma nAT \exp(-x/\lambda)\, dx \qquad (2.6)$$

where f is the X-ray flux, σ is the photoelectron cross-section, n is the number of atoms per unit volume, A is the area from which the photoelectrons are collected, T is the instrumental transmission factor, and λ is the IMFP. The total photoelectron signal is

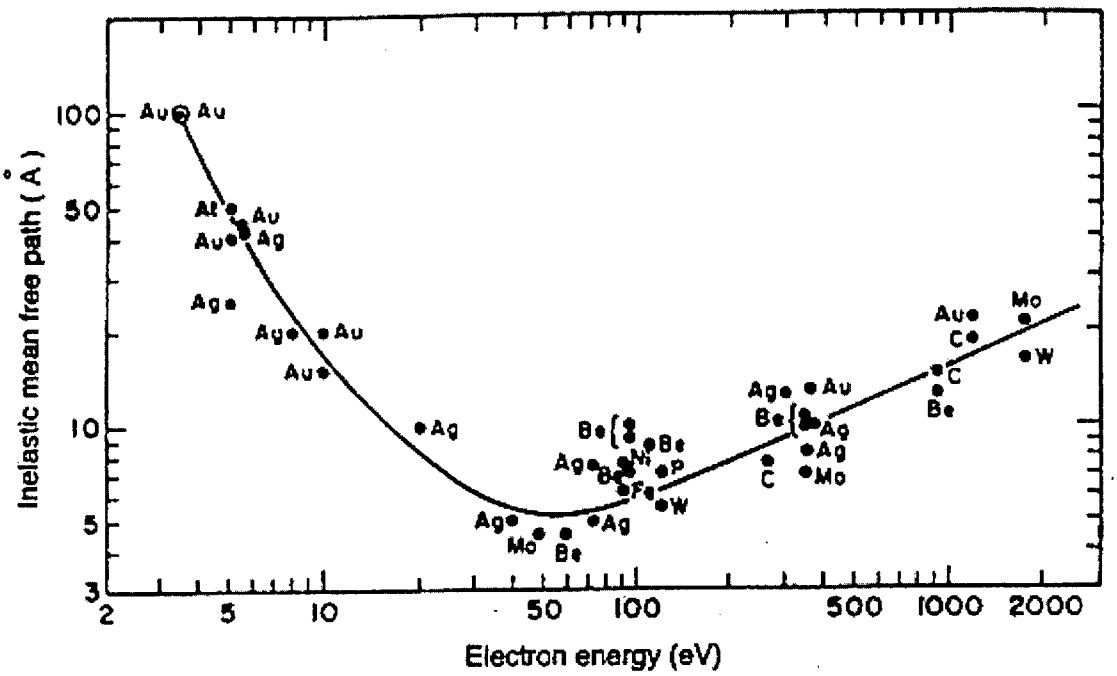

Figure 2.6 Inelastic mean-free path values for electrons with various kinetic energies inside a solid [2.9]

obtained by integrating from x = 0 to x = ∞, which yields:

$$I = f\sigma nAT\lambda \tag{2.7}$$

During a measurement, where instrument settings are fixed, f, σ, A and T are constant and may be grouped to form one constant known as the *Sensitivity Factor* (S). S is determined by particular instrumental settings and the particular peak under study. I is then expressed as follows for this special homogeneous sample:

$$I = n\lambda S \tag{2.8}$$

In principle, this allows comparing corresponding signals from different elements by taking an atomic ratio between two elements, since a complete list of values of S are available for the MAX 200 system. This is done as follows [2.3]:

$$n_1/n_2 = [(I_1/S_1)/(I_2/S_2)][(\lambda_1)/(\lambda_2)] \tag{2.9}$$

Tabulated values of λ_1 and λ_2 are available and can be used, but it is common in semi-quantitative work to keep the ratio $[(\lambda_1)/(\lambda_2)]$ constant at the value of unity. Then, adjusted intensities alone can be used to estimate atomic ratios within the depth probed. That approach was used in this work to estimate relative compositions using XPS.

2.1.6 Data Processing

XPS data generally require processing in order to extract more-detailed chemical information from a photoelectron peak. This starts with a background correction, which involves the non-linear subtraction approach introduced by Shirley [2.12]. An example is shown in Figure 2.7 for an O 1s spectrum. The number of electrons counted at the higher binding energy boundary is greater than that at the lower binding energy boundary. Contributions to the background come from inelastically scattered electrons. The Shirley method assumes that, at any point in the spectrum, the background signal is proportional

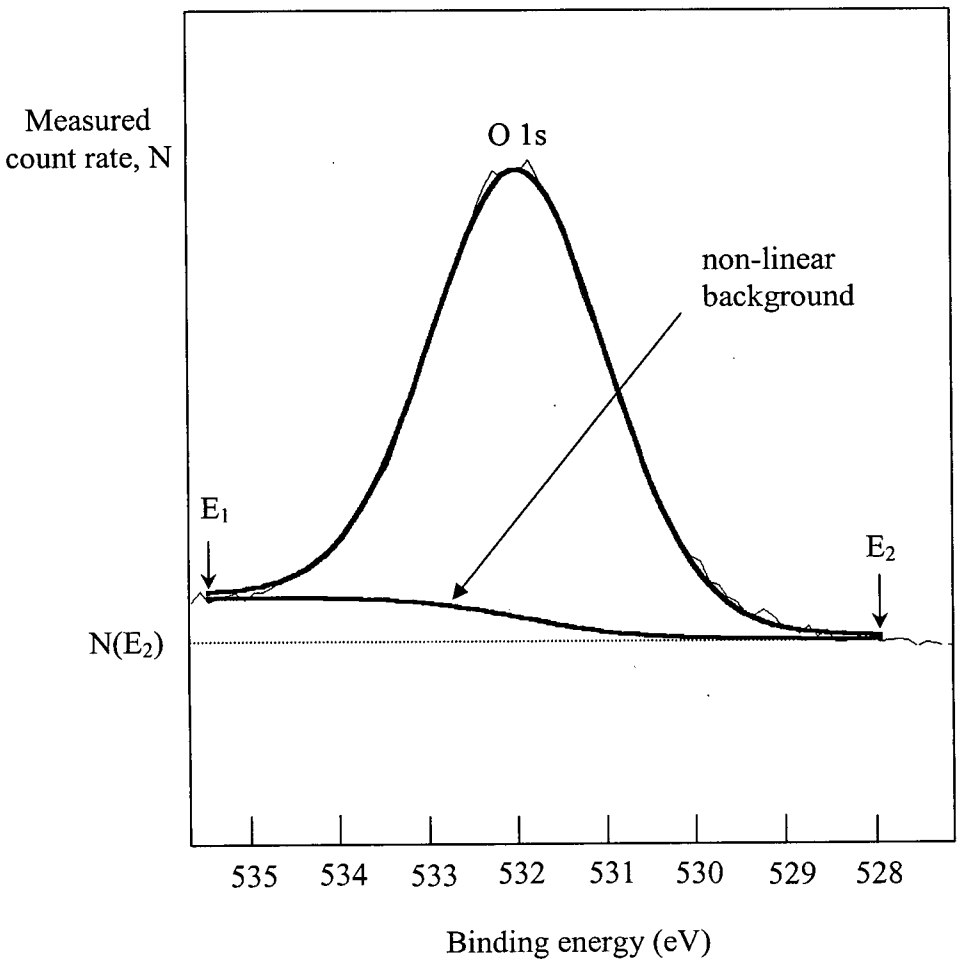

Figure 2.7 Shirley non-linear background subtraction applied to an O 1s spectrum

to the number of electrons elastically scattered at higher kinetic energy. This correction of inelastic contributions over the energy range E_1 to E_2 (lower and upper kinetic energies chosen by the operator) is determined by the iterative algorithm [2.12]:

$$N'_{k+1}(E) = N(E) - N(E_2) - C\int_{E}^{E_2} N'_k(E)dE \qquad (2.10)$$

where N(E) is the measured count rate, $N'_k(E)$ identifies count rates after subtraction of background contributions (the index k indicates the k^{th} iteration). The reference background level is provided by $N(E_2)$, and C is fixed by the requirement that $N'_k(E_1)$ equals 0. The process starts with $N'_1(E)$ equaling 0 and continues until $N'_{k+1} \sim N'_k$. Usually, the functional form of the Shirley background correction converges after three or four iterations. This background is then subtracted from the measured raw spectrum.

Higher resolution spectra after background correction often show structures arising from overlapping chemical species. Figures 2.8 (a) and (b) show examples of an Al 2p narrow scan spectra before and after data processing, respectively. A curve fitting procedure is needed to identify the individual components with regard to the peak position, intensity, and FWHM. The mathematical approach chooses a functional form for each component profile, and simulates a measured spectrum (after subtraction of background) by a sum of the individual components. The computer processing programme for the MAX 200 spectrometer allows each such component to be represented by a mixed Gaussian/Lorentzian functional form [2.7]. The *XPS Peak 4.1* programme, used in addition to the programme for the MAX 200 spectrometer, also performs such calculations [2.13].

After an initial estimation of these parameters for all components needed to fit a spectrum, the programme multiply iterates to optimize the fit between the simulated

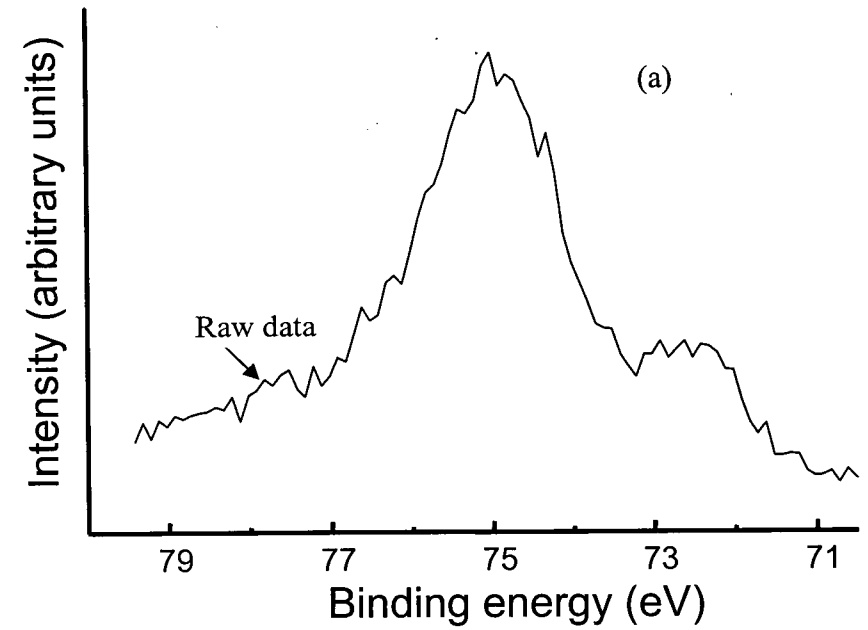

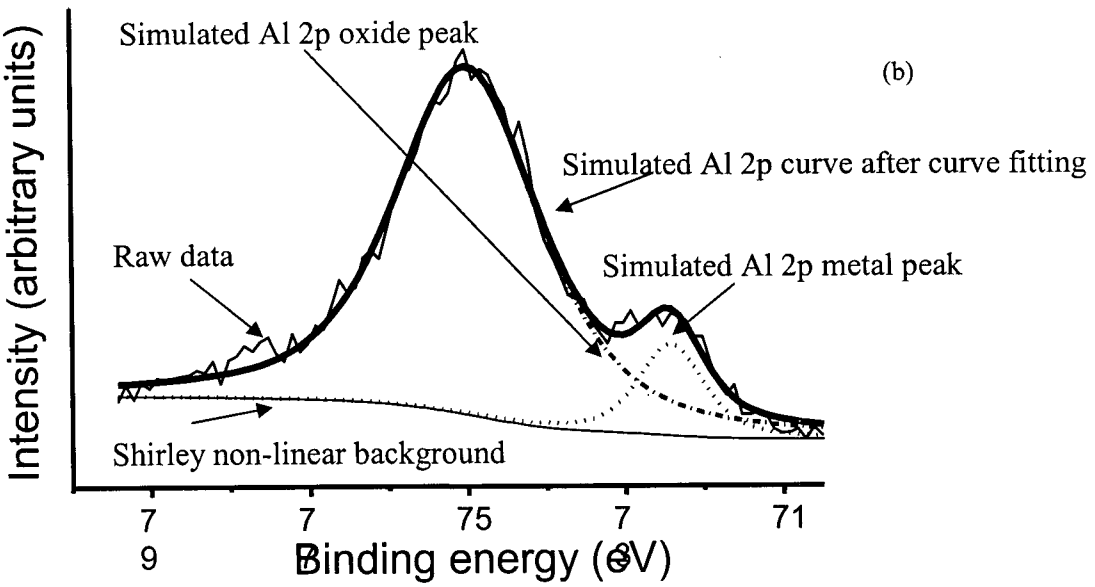

Figure 2.8 Al 2p spectrum (a) before data processing; (b) after data processing

spectrum and the measured spectrum. This involves minimizing the least-squares function (χ):

$$\chi = [(1/N_{free})\Sigma_j(Y_{measured,j} - Y_{fit,j})^2 / Y_{measured,j}]^2 \qquad (2.11)$$

where j ranges from 1 to N, $Y_{measured,j}$ is the measured count rate at the j^{th} data point, $Y_{fit,j}$ is the corresponding value of the simulated function expressed as a sum of the Gaussian/Lorentzian functions, N is the number of data points, and N_{free} is $N - N_{fit}$ (where N_{fit} is the number of parameters to be fitted through the minimizing process). The XPS peak fitting programme *XPS Peak 4.1* has a similar curve-fitting algorithm and is also used in determining information about peak intensities [2.13].

It is important that all components added must meet reasonable chemical criteria for the particular system being studied. A visual comparison of the measured and simulated curves, as well as comparisons to known standards, is also advisable in order to guard against any weaknesses in the numerical fitting routine.

Figures 2.8 (a) and (b) show a comparison of an Al 2p peak before and after data processing, respectively. After sufficient processing, it is clear that there are two peaks present; one peak is centred around 72.6 eV and a second peak is centred around 75.6 eV. FWHM values were also calculated for each peak; values of 1.7 eV and 0.9 eV were obtained for the first and second peak, respectively. Comparing the values of these parameters to established literature values (~ 1.7 eV for the oxide component, ~1 eV for the metal component) reveal that these peaks represent the metallic Al and Al oxide components of a sample [2.3].

2.2 Scanning Electron Microscopy (SEM)

2.2.1 Introduction

Scanning electron microscopy (SEM) provides one of the most important imaging techniques for the surface characterization of materials. Unlike transmission electron microscopy (TEM), samples need not be sectioned as the electron beam does not pass through the sample to form the image. In SEM, the sample is raster scanned by a highly-focused incident electron beam (called the primary electron beam) with energies typically in the range of 10 – 50 keV [2.14, 2.15]. Low-energy secondary electrons emitted from the sample are collected from each area probed, and an image of the whole surface studied is displayed with a cathode ray tube (CRT) by summing images from each area. Each region in the whole secondary electron image matches in a one-to-one fashion to the corresponding area probed by the incident beam, and thus a topographical image of the sample surface can be obtained. With the most advanced equipment, and adequate sample preparation techniques, details can be resolved to better than 10 nm, and a large depth of field can be obtained [2.14].

2.2.2 Basic Principles

When a sample is placed in the microscope and bombarded with the primary electron beam, electrons can be emitted according to various processes. Figure 2.9 shows a general energy distribution curve for the emitted electrons [2.16]. Electrons that contribute to the secondary electron peak (e.g. with kinetic energies less than 50 eV) are studied in SEM [2.17]. They originate from a cascade effect of various complex processes [2.18]. Elastically-scattered electrons are redirected from the primary beam by interaction with the positive ion cores associated with atoms in the solid. These electrons

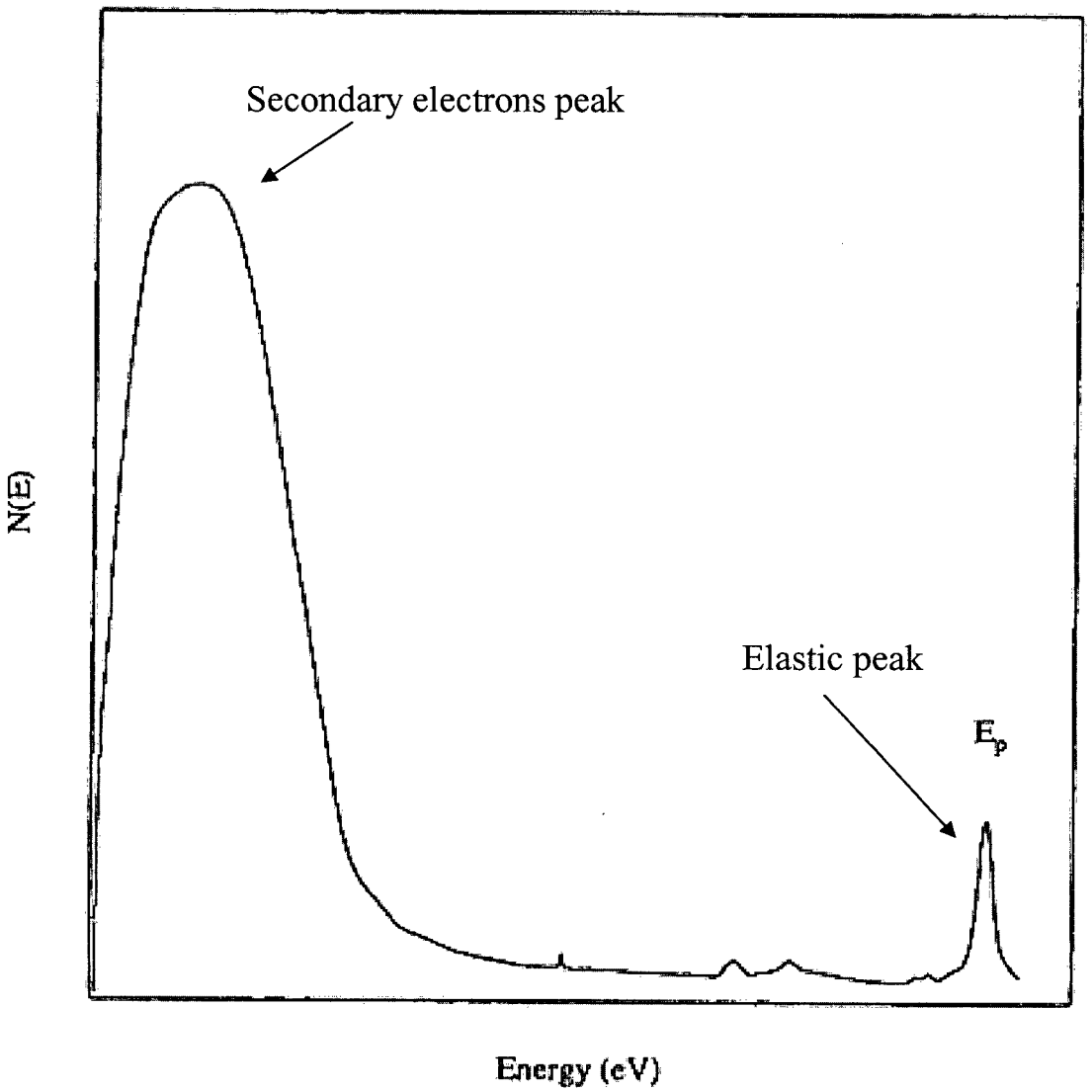

Figure 2.9 Energy distribution of electrons emitted from a sample as a result of impact by a primary electron beam of energy E_p (Modified from [2.16])

can lose energy by plasmon excitation. Auger electrons and X-ray photons may also be emitted. While electrons are emitted over a wide energy range, those in the secondary electron peak are most useful for forming the topographical images [2.14, 2.15, 2.19 – 2.21].

The primary electron beam can penetrate deep into the surface (several μm) and produce many secondary electrons. However, the secondary electron peak carries information especially from the topmost region of the surface, as a result of the strong tendency for inelastic scattering discussed in Section 2.1.5 [2.15].

The image contrast and resolution of SEM images are determined by the number of secondary electrons collected from a scanned site. The more secondary electrons collected, the brighter the spot appears on the CRT. Several factors influence the number of secondary electrons emitted including (i) the accelerating voltage of the primary electron beam; (ii) the surface morphology and angle at which the primary electron beam hits the surface; (iii) the specific element being studied; (iv) the surface chemistry and crystallography of the sample; and (v) local charging on the sample surface [2.17]. The low-energy secondary electrons are considered to be produced over a bulb-like volume. An example is shown in Figure 2.10 indicating how the probability for escaping can be affected by the local morphology [2.20]. According to the model, more secondary electrons escape from the surface at the sides of a protuberance, compared to a flat region. This contributes to the contrast seen in SEM images [2.14, 2.15, 2.17, 2.20, 2.21].

2.2.3 Instrumentation

A schematic of the Hitachi S4100 SEM is shown in Figure 2.11 [2.22]. The main

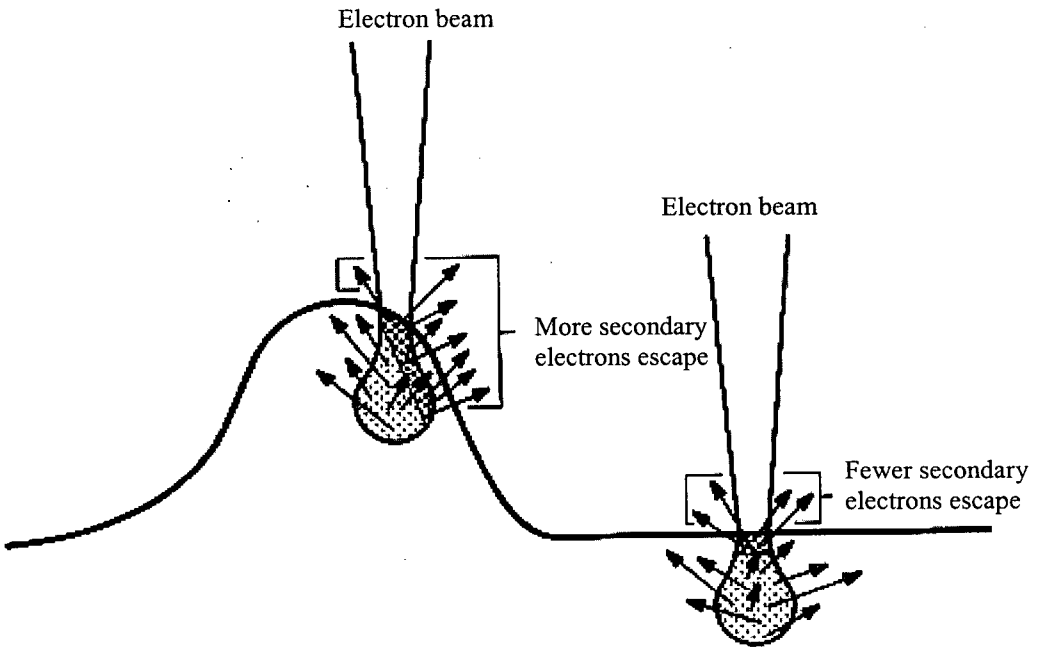

Figure 2.10 Example of morphology influencing the number of escaping secondary electrons [2.20]

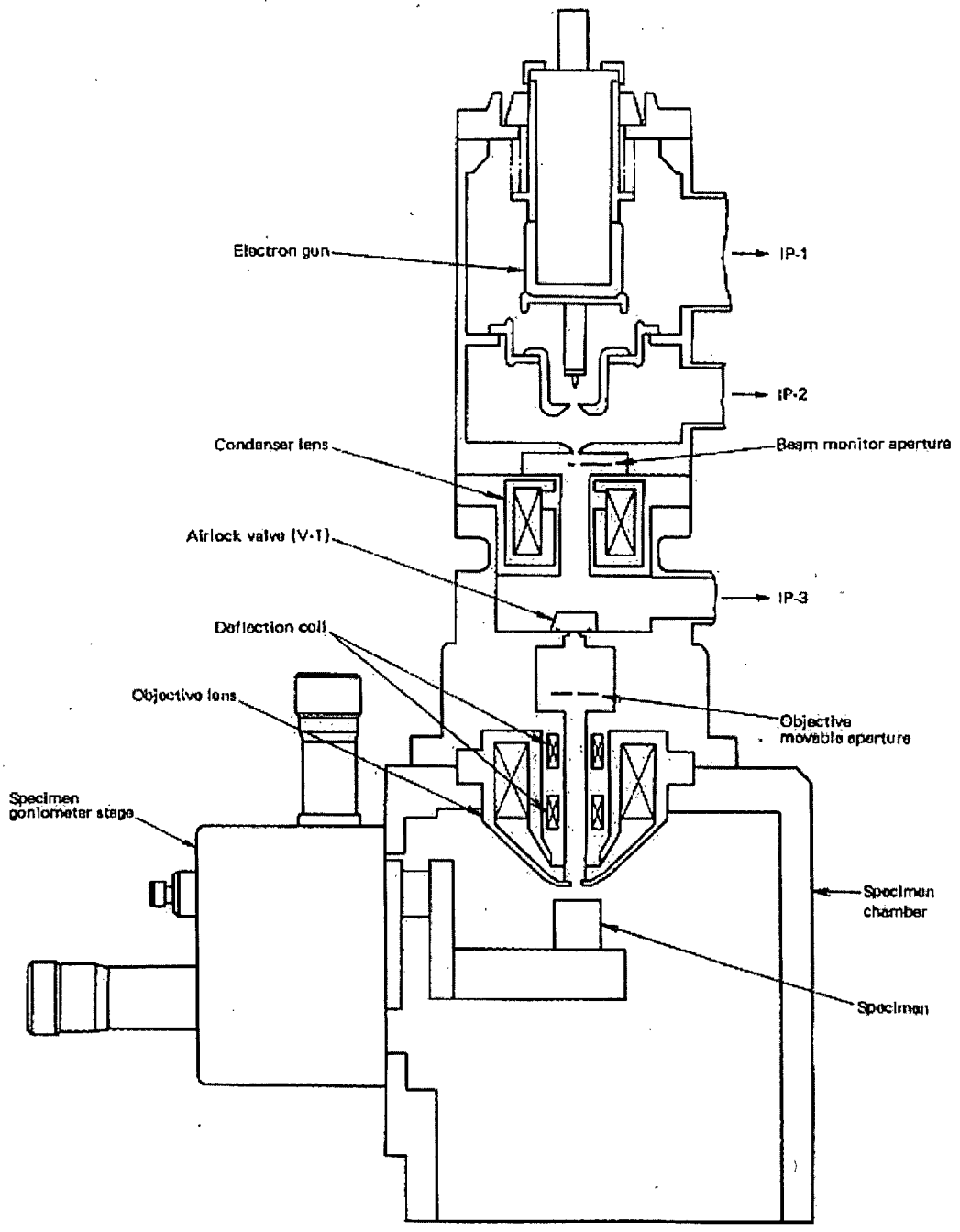

Figure 2.11 Schematic of the Hitachi S4100 SEM [2.22]

components include (i) an electron beam source; (ii) a set of electromagnetic lenses; (iii) an Everhart-Thornley detector; (iv) a vacuum system; and (v) a computer for digital storage of images.

The Hitachi S4100 SEM system in Professor Tiedje's laboratory in AMPEL uses a field-emission electron gun (FEG). With a field-emission system, electrons are physically drawn off a finely-curved W tip by an applied voltage field in ultra high vacuum. The FEG is not heated and this leads to several advantages, including a longer gun life, over other electron beam sources, such as W-hairpin or LaB_6 sources. The major advantage of the FEG, however, is the ability to create a smaller beam diameter. This improves the resolution of the SEM images [2.20].

The electromagnetic lens system, which includes a condenser and an objective lens, and scanning and deflection coils, helps control the focus of the primary electron beam in order to modify the spot size and depth of field. These factors help to control resolution and magnification of the image. The deflection coils are used to raster the beam across the sample area to be imaged [2.23].

The detector has a positive potential to attract secondary electrons to a scintillator connected to a photomultiplier tube, and the image is passed to the CRT [2.20]. The summed SEM images are stored digitally using the *Quartz PCI 5.1* image management system.

The vacuum system used in the Hitachi S4100 SEM is especially important for the FEG which operates at around 1×10^{-9} mbar, and is pumped by a combination of ion, diffusion, and rotary pumps [2.20, 2.22]. The sample chamber is operated under a vacuum of 7×10^{-6} mbar obtained by a diffusion pump backed by a rotary pump [2.22].

2.3 Polarisation Curve Measurements

2.3.1 Introduction

The technique of electrochemical polarisation curve measurement provides a very convenient route for quickly assessing tendencies for corrosion. The approach involves measuring the current density (i) at an electrode-electrolyte interface as a function of an applied overpotential, η (where η is referenced with respect to the equilibrium potential) [2.24 – 2.26].

For an electrode process:

$$M \leftrightarrow M^{+} + e^{-} \qquad (2.12)$$

the forward (anodic) reaction represents metallic oxidation while the back (cathodic) reaction represents reduction. In general, both reactions occur simultaneously, and each reaction rate can be correlated with an associated current density [2.24 – 2.26]. At equilibrium, the rates of the anodic and cathodic reactions are equal, and this can be expressed as:

$$i_a = i_c = i_o \qquad (2.13)$$

For this situation, no net current will be measured since the current densities in the two directions balance. The magnitude of this current is referred to as the *Exchange Current Density, i_o*. As the potential applied to the electrode is changed from the equilibrium value, net current will flow, and this corresponds to a modification in the relative free energies for the reactants and products. An increased positive potential will lower the free energy for the electron side of the reaction, and this will modify the activation barriers.

A standard treatment for how changing the applied potential modifies the activation energy barriers for the forward and back reactions is contained in the Butler-Volmer analysis [25, 27, 28]. The Butler-Volmer equation takes the form:

$$i_{measured} = i_o \{\exp [(\alpha\eta F)/RT] - \exp [(\alpha-1)\eta F/RT]\} \quad (2.14)$$

when the solution is sufficiently stirred or when current densities are low enough that the surface concentrations do not differ appreciably from the bulk concentrations [2.25]. In Equation (2.14), η is the overpotential, F is the Faraday Constant, R is the Gas Constant, T is the temperature, and α is a transfer coefficient with a value between 0 and 1. This value depends on how the applied potential modifies the two activation barriers in the Butler-Volmer treatment [2.27, 2.28].

Equation (2.14) is useful for interpreting measured polarisation curves for the kinetics of irreversible electron transfer such as the example in Figure 2.12. In this example, the lower arm is called the *Cathodic Arm* where the cathodic polarisation measurement is done. The upper arm is called the *Anodic Arm* where the anodic polarisation measurement is plotted. The potential where the anodic and cathodic arms meet defines the equilibrium or *Free Corrosion Potential* (E_{corr}). The corresponding current density is i_o. The example shows Tafel behaviour where the measured polarisation curves, as plotted, have linear dependencies. This corresponds to treating the anodic and cathodic parts of Equation (2.14) separately, with zero contribution from the other [2.24, 2.26].

The general Tafel equation is:

$$\eta = \beta \log (i/i_o) \quad (2.15)$$

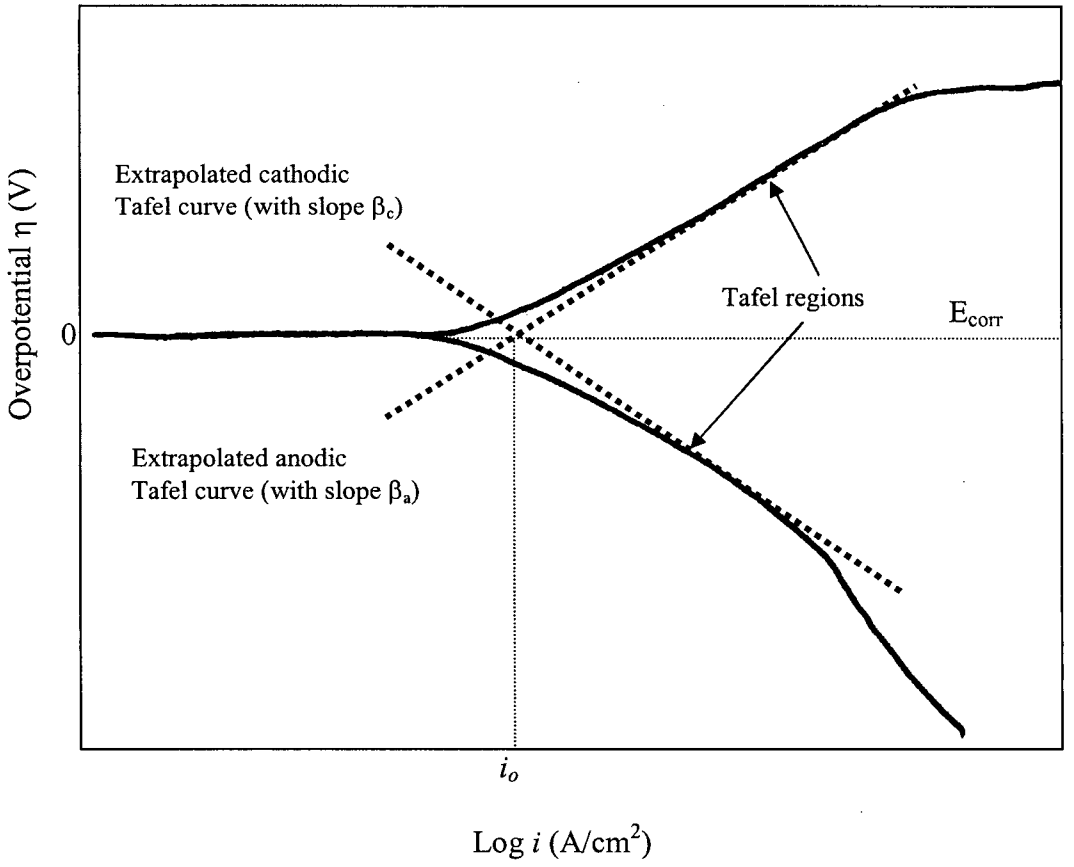

Figure 2.12 Electrochemical polarisation curve for a corrosion system

where i is the measured current density and β is the Tafel constant [2.29]. For the anodic current, β takes the form:

$$\beta_a = 2.303RT/\alpha F \qquad (2.16)$$

and for the cathodic current, β takes the form:

$$\beta_c = 2.303RT/(\alpha-1)F \qquad (2.17)$$

Extrapolation of the two linear Tafel regions yields E_{corr}, and the equilibrium current i_o.

2.3.2 Instrumentation

Figure 2.13 is a schematic of the three-electrode cell with a potentiostat used for measuring electrode current as a result of a changing applied potential. The potential is measured between the electrode of interest, called the *Working Electrode*, and a reference electrode [2.26]. The current is measured between the working electrode and the counter electrode. The potentiostat ensures that no current flows between the working electrode and the reference electrode as the applied potential is changed. In this work, the counter electrode is composed of Pt, and the reference electrode is a saturated calomel electrode.

Polarisation measurements were made with a Solartron 1286 Electrochemical Interface (Schlumburger Technologies). The potential between the working and reference electrodes is stepped linearly and the associated current is recorded for each step. *Corrware* and *Corrview* software programmes provided with the potentiostat were used for data acquisition and curve plotting. In this work, i_o is estimated using the *Corrview* software by the extrapolation noted above for plots such as Figure 2.12.

The reference electrode is placed in a Haber-Luggin capillary tube which is then positioned within 3 – 5 mm (the diameter of the capillary tube) from the working

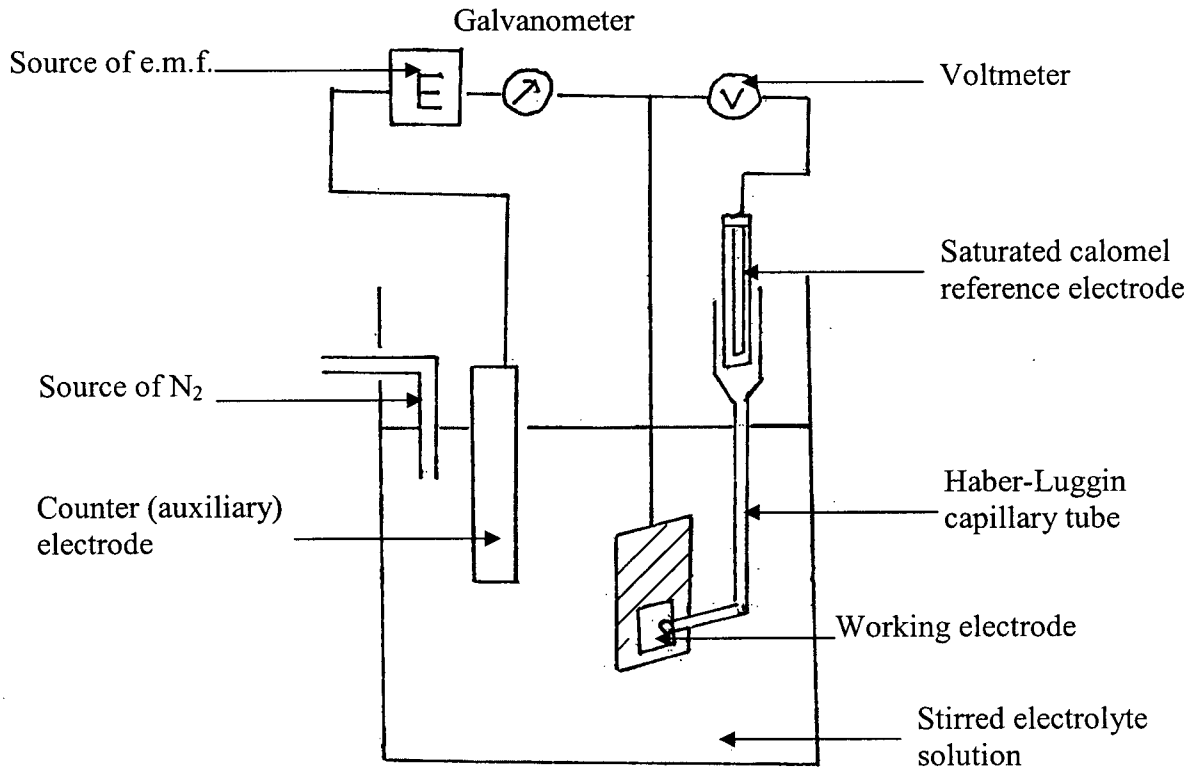

Figure 2.13 Schematic diagram of a three-electrode cell [2.26]

electrode surface. The solution used inside the cell and the capillary tube has the fixed concentration of 35 g of NaCl in 1 L of deionised water. The system is set up to eliminate any extraneous potential drops in the circuit that could otherwise obscure Tafel behaviour [2.26, 2.28, 2.30, 2.31].

The measurement of polarisation curves in the Tafel region directly gives the electron transfer rates, as expressed by i_o for equilibrium. Larger values of i_o correspond to higher probabilities for electron transfer and hence reaction rates in an oxidation-reduction process, such as in corrosion. These measurements do not necessarily identify the actual chemical reactions involved. The polarisation curves measured in this work are used entirely to follow trends in behaviour, shown by comparing values of i_o obtained as changes are made to coatings and pretreatments applied to aluminum alloy surfaces.

Chapter 3 Effects of Alkaline Etching and Silane Concentration on the Deposition of BTSE to Al-2024 Alloy

3.1 Introduction

The importance of surface pretreatment and alkaline etching prior to silane deposition has been previously discussed in Section 1.4.2. In addition, Van Ooij and Child have provided some criteria for what they define as a good silane film for corrosion protection. These authors conclude that such a film should have the following characteristics [3.1, 3.2]: (i) it should be firmly anchored to the metal by Si-O-M bonds formed from Si-OH and M-OH groups; (ii) it should be around 50 – 100 nm thick; (iii) it should form a homogeneous coating; (iv) there should be many functional groups in the film which can react with the polymer that will be coated subsequently on the silane layer; and (v) the film should be stable in the atmosphere (i.e. Si-O-M that bonds do not hydrolyse nor do the functional groups oxidize).

Van Ooij suggests careful preparation of the silane solution is important since coatings formed can be highly dependent on such variables as solution pH, hydrolysis time, and silane concentration. Van Ooij and other research groups have found that most silanes that are useful for coating metals as coupling agents and corrosion inhibitors contain methoxy or ethoxy groups which can hydrolyse in aqueous or aqueous/alcohol solution [3.1 – 3.3].

The pH of the solution is critical for two reasons. The first reason is that the pH should be suitable to allow silanes to have the maximum rate of hydrolysis and minimum rate of condensation. Both reactions occur simultaneously. Pu et al. examined the effects of pH on the rate of hydrolysis of the six ethoxy groups on BTSE and found that a 1%

BTSE solution with pH 4.5 is optimal, and that a pH range between 2 and 5 is suitable for BTSE hydrolysis [3.4]. The second reason is that the solution pH should be adjusted to match the value that gives the isoelectric point for the metal oxide structure. Off-optimal pH values may cause the silane to be adsorbed in an "upside down" manner [3.5 – 3.9]. In the case of BTSE, however, the problem of right-side-up and upside-down bonding is avoided as the monomer is symmetrical and its acidic nature allows for better bonding between the metal oxide and the silane.

Hydrolysis times are known to affect the nature of the coated film. If hydrolysis times are too short, thinner films may result with unhydrolysed functionalities resulting in a lower degree of cross-linking in the film. This leads to a more porous film where water and ions promoting corrosion may penetrate. Premature polymerisation of the silane is also detrimental to the quality of the coating as the pre-polymerized film leads to poorer silane-metal bonding which leads, in turn, to poorer corrosion protection [3.1, 3.2].

Van Ooij and co-workers, Underhill and co-workers, and other groups have shown using the monofunctional silanes γ-APS [3.1, 3.2] and γ-GPS, respectively, that silane concentration is important in determining film thickness [3.10 – 3.14]. A film too thin is not sufficient for corrosion resistance. Increasing the thickness helps to increase corrosion resistance, but a film that is too thick may be brittle and the film may crack.

The objectives of this chapter include the following:

(i) To study the effects longer alkaline etching times have on the chemical and surface morphological properties of Al-2024; and the subsequent effects these changes have on the corrosion performance of the alloy. As mentioned previously in

Section 1.4.2, while procedures are available, no standard time or solution concentration have been established for the alkaline etching process. In addition, several authors have reported that alloy enrichment occurs as a result of alkaline etching. Again, however, no studies have been documented as to whether there is a correlation with the etching duration and the degree of Cu enrichment.

(ii) To study the effects of the concentration of the silane solution used on the deposition of silane onto the alloy substrate, and hence, on the corrosion performance of the coated alloy. Van Ooij and Underhill have demonstrated, for γ-APS and γ-GPS, respectively, on various alloys and other metals that a relationship between concentration and silane film thickness exists which may benefit corrosion protection of the specific alloy used. An attempt will be made to establish similar findings for BTSE on Al-2024.

(iii) The final objective in this chapter is to study the interrelationships of alkaline etching times and silane solution concentration on the silane deposition and corrosion performance of the coated samples. To date, there are no documented studies for such effects. It may be advantageous, for example, to deposit more silane onto the substrate surface using a solution with a lower silane concentration and exposing the substrate to longer alkaline etching times, although it is the degree of corrosion protection that is ultimately most important.

Figure 3.1 shows a flow chart of the various samples tested and their designations. Objective (i) is covered by comparing sample A with samples B, C, and D; objective (ii) by comparing sample B with samples E, F, and G; and objective (iii) by comparing samples E and F with samples H, I, J, and K.

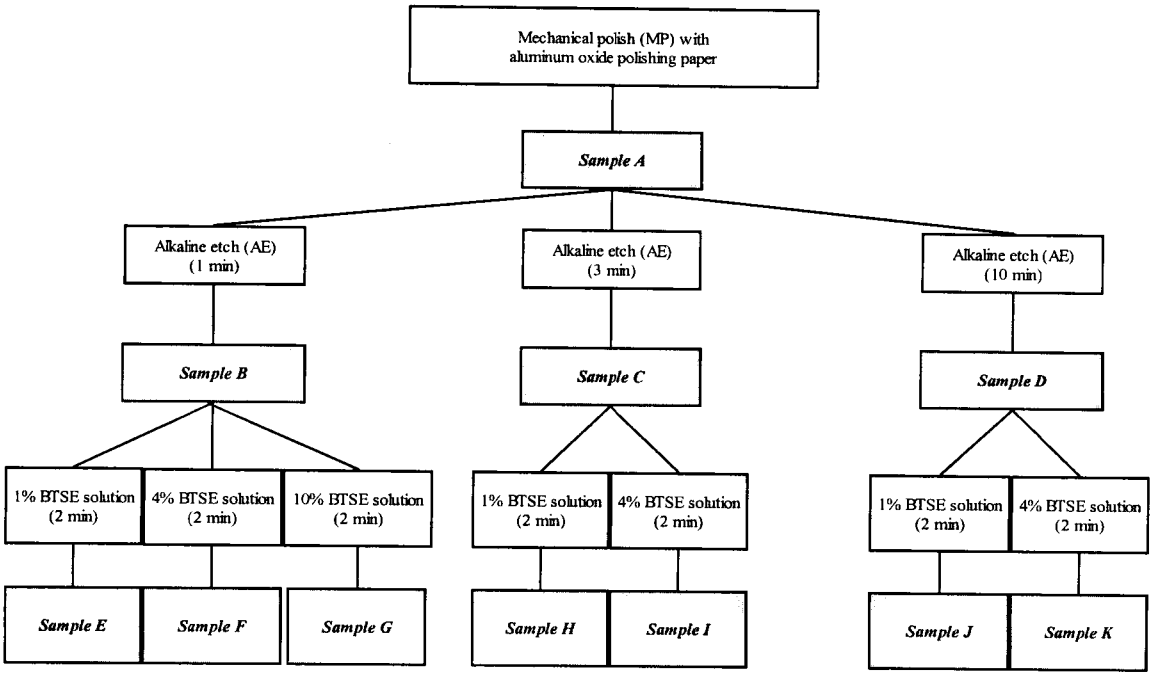

Figure 3.1 Experimental flowchart for pre-treatments, silane treatments, and sample designations used for the work in Chapter 3

3.2 Experimental

Tests with XPS, SEM, and immersion testing were made on treated Al-2024 samples which were first cut into 1 x 1 cm^2 panels, while panels with dimensions of 1 x 5 cm^2 were used for the polarisation curve measurements. All panels were first mechanically polished with 400 grit aluminum oxide polishing paper, and then with 1200 grit aluminum oxide polishing paper (Metaserv Universal Polish). The polished panels were degreased twice in acetone for 10 minutes each and finally immersed in methanol for 10 minutes, all performed in a sonic bath. Alkaline etching was done according to the various procedures outlined in Figure 3.2 [3.15, 3.16].

BTSE solutions of 1, 4, and 10 % (v/v) concentrations were made fresh for each experiment in 100 mL volumes. The solutions were prepared by mixing appropriate volumes of BTSE silane (Aldrich Chemical Co.) and methanol, with six mL of deionised water. The solutions were then stirred continuously for a minimum of five hours prior to use and the solution pH measured. Provided the measured pH agreed with literature values (pH 4.50 for 1% BTSE, 4.00 for 4% BTSE, and 2.70 for 10% BTSE), the silane solution was then used without further testing [3.4].

After the substrate panels had been immediately immersed in the appropriate silane solution for two minutes, they were then laid flat to air-dry overnight in a covered Petri dish to ensure curing of the silane.

XPS spectra from samples were taken using a pass energy of 192 eV for survey scans and 48 eV for the higher-resolution spectra. The Al Kα source (1486.6 eV) was used with an emission current of 20 mA at 10 kV. Spectral analysis was done using the computer programmes discussed in Section 2.1.6.

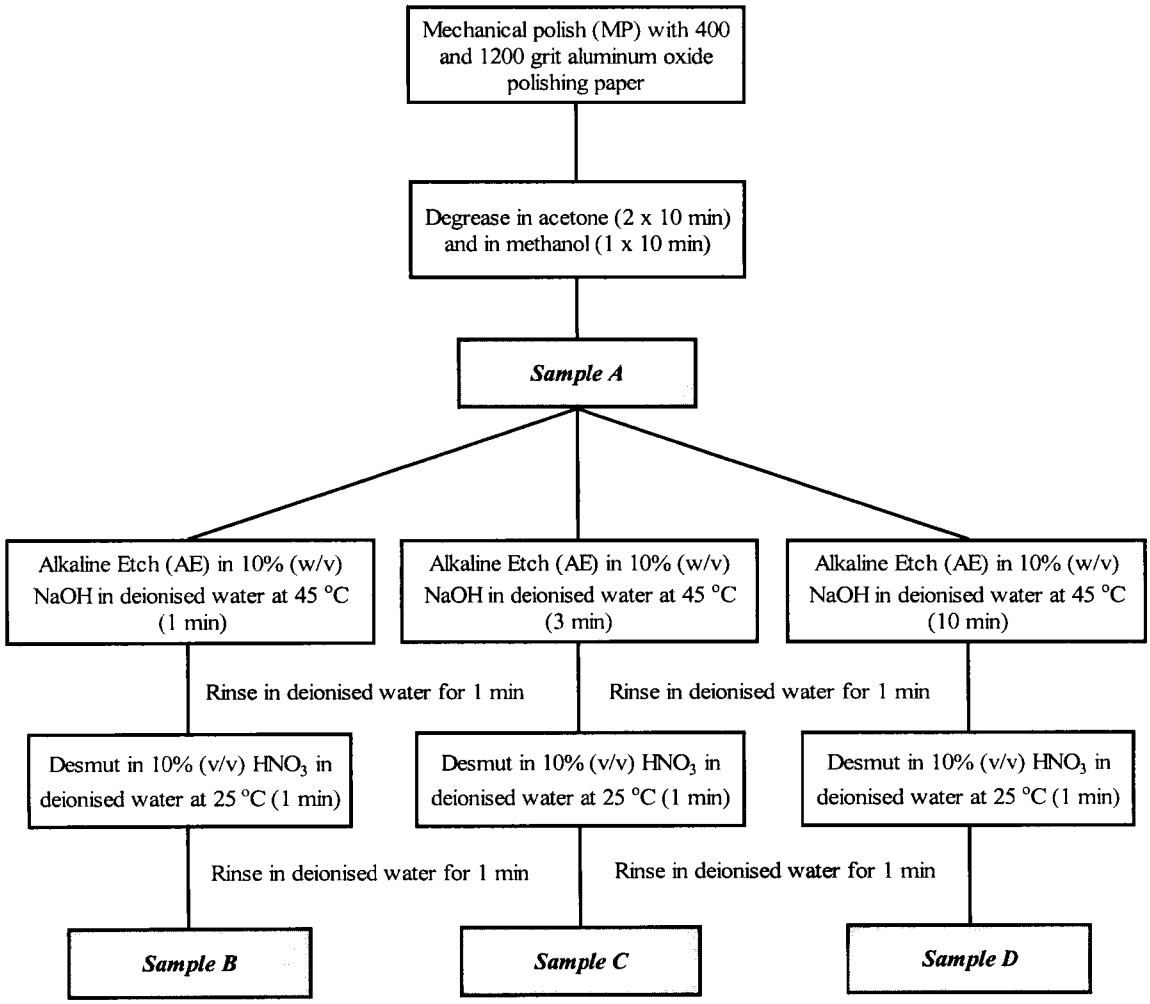

Figure 3.2 Flowchart of procedures and sample designations used to study the effects of alkaline etching time on Al-2024

SEM micrographs were measured using the instrument described in Section 2.2. The accelerating voltage was set at 15 kV, with an emission beam current of 10 μA, and an extraction voltage less than 4.5 kV.

For the polarisation curve measurements, prepared 1 x 5 cm^2 panels were painted with electrical paint to cover all areas of the sample except for the part acting as the working electrode (approximately 1 x 1 cm^2) and the area where the panel was connected to a sample holder via an alligator clip. The holder and sample were then wrapped in Teflon tape and immersed in the NaCl solution described in Section 2.3.2. The solution was deaerated using N_2 for 10 minutes to purge out oxygen. Care was taken to ensure that the alligator clip and the connection area were above solution level and wrapped with Teflon tape to prevent galvanic coupling of the holder and sample. An open circuit potential test was performed for five minutes to determine E_{corr} for each experiment and to stabilize the system. Scans were then completed from 0.25 V below to 0.5 V above E_{corr} at a rate of 1 mV/second. All potentials reported are referenced against a standard calomel electrode.

Immersion testing was performed by suspending panels of interest in 100 mL of the NaCl solution prepared for polarisation testing (35 g NaCl in 1 L deionised water). The panels were suspended for one week and the solutions were changed every 24 hours during that period. At the end, SEM micrographs were measured after rinsing the immersed panels with deionised water.

3.3 Results: Effects of Alkaline Etching on Uncoated Al-2024 Alloy

3.3.1 XPS Studies

The Al-2024 samples studied in this section were prepared according to the procedure shown in Figure 3.2. Figure 3.3 is a survey spectrum from Sample B, which has been alkaline etched for 1 minute. The survey scan shows the presence of Al, O, and C. The latter element is introduced as contamination from the atmosphere, while some O is due to contamination, the rest is attributed to the aluminum oxide. Although difficult to see on the survey scan, Cu from the alloy was detected in the higher-resolution spectrum. Figure 3.4 shows the Al 2p spectra from various samples. After mechanical polishing only (sample A), two peaks are present in the Al 2p spectrum. One peak is at 72.7 eV, which corresponds to metallic Al, while the second peak, at 75.6 eV, indicates an oxide form [3.17]. The detection of the metallic Al peak suggests that the oxide film is no more than about 60 Å thick, assuming that the oxide film is homogeneous.

The alkaline etched samples B and C also show spectra with a peak at 75.6 eV. As the alkaline etching time increases, the metallic Al peak (72.7 eV) decreases, and the oxide peak increases. After 3 minutes of etching, the metallic peak is no longer detected, and it is clear that longer alkaline etching times result in more oxide (more etching product), which masks the metallic Al signal.

Table 3.1 reports the percentage composition of elements on the surface obtained from the XPS experiments performed. The alkaline etching treatments, as shown by samples B, C, and D, result in the Cu 2p peak being detected, so indicating the presence of copper in the top 60 Å of the surface. Cu/Al ratios also appear to increase with increasing alkaline etching times (Cu/Al is 0.1 for 1 minute of alkaline etching, 0.2 for 3

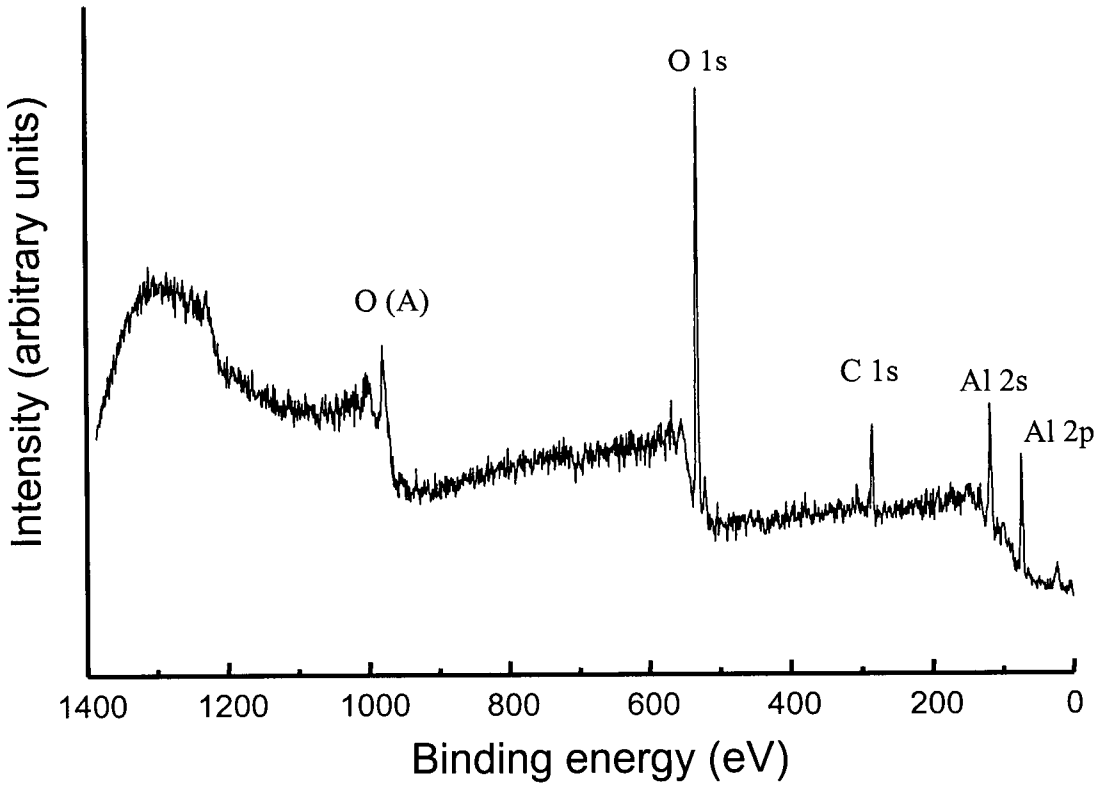

Figure 3.3 XPS survey scan from sample B (Al-2024 alkaline etched for 1 minute)

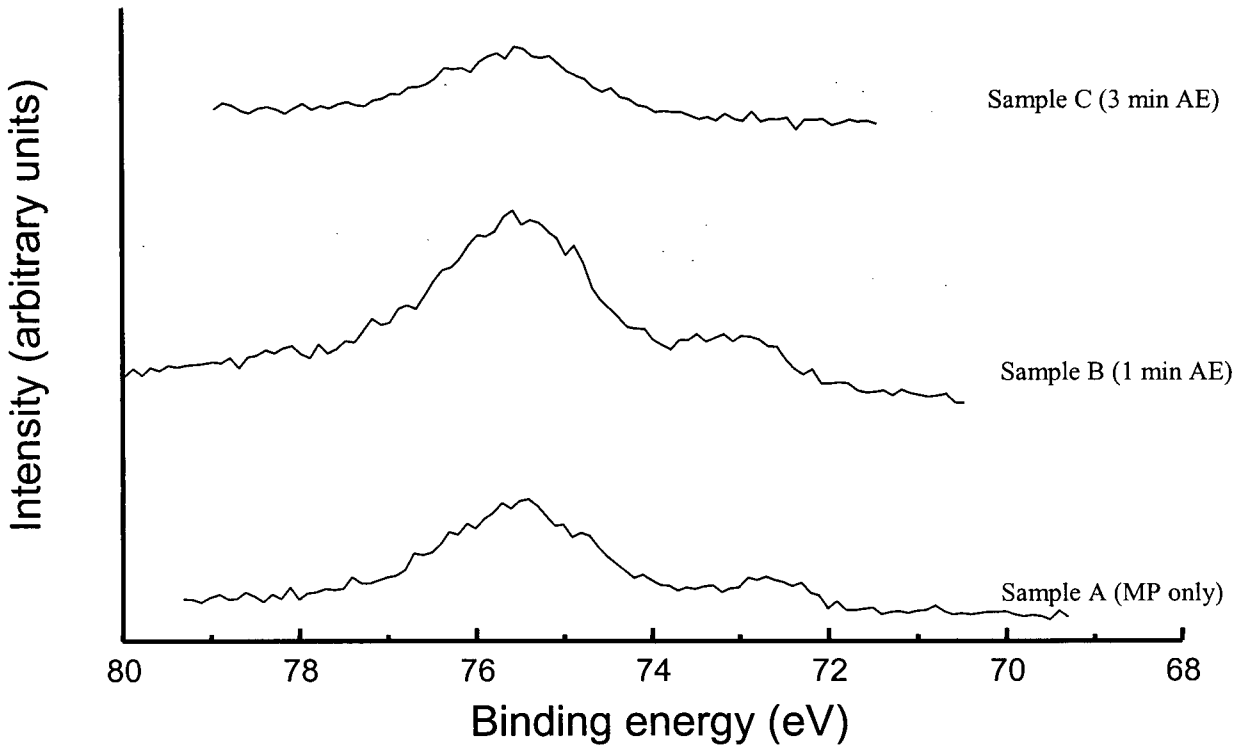

Figure 3.4 Al 2p spectra from Al-2024 after various alkaline etching times

Table 3.1 Percentage elemental compositions from XPS for Al-2024 samples given different treatments as specified in Figures 3.2, 3.8, and 3.12

Sample	Al	Cu	C	O	Si
A	20.2	--	40.1	39.7	--
B	27.8	0.4	20.3	51.5	--
C	25.9	0.5	31.9	41.6	--
D	26.6	0.7	27.6	44.6	--
E	11.9	--	37.1	36.2	15.1
F	--	--	42.3	36.3	21.4
G	--	--	35.2	40.2	24.7
H	--	--	35.2	41.6	23.3

minutes, and 0.3 for 10 minutes). No copper, however, was detected for the mechanically polished sample (sample A). This indicates that the copper enrichment at the alloy surface is directly associated with the alkaline etching step and that a correlation between the duration of alkaline etching and the degree of copper enrichment exists [3.18 – 3.21].

3.3.2 SEM Studies

Figure 3.5 (a) – (d) shows SEM micrographs from samples taken prior to immersion and polarisation testing. Figure 3.5 (a) shows a sample that has been mechanically polished (sample A). Scratch lines from the polishing are evident, but no etching product is seen. Figure 3.5 (b) shows a sample that was alkaline-etched for 1 minute after being mechanically polished (sample B). The scratch lines are still visible, but they are faint in comparison to Sample A. Some pitting and scalloping are also seen, and etching product is detected. Figure 3.5 (c) shows a sample that was alkaline-etched for 3 minutes (sample C). The scratch lines are no longer visible, but more pits and etching product are seen compared to sample B in Figure 3.5 (b). This increase in the amount of etching product explains the inability to detect the Al metallic peak in XPS from the sample that has been alkaline etched for 3 minutes [3.22 – 3.25]. Figure 3.5 (d) shows the SEM micrograph from sample D, which has been alkaline-etched for 10 minutes. Again, more etching product, and an increase in the pitting density, is seen in comparison to the other samples. These results indicate, visually, an increase in surface roughness, and an increase in the amount of etching product, with increasing alkaline etching times; such observations correlate with results seen from XPS.

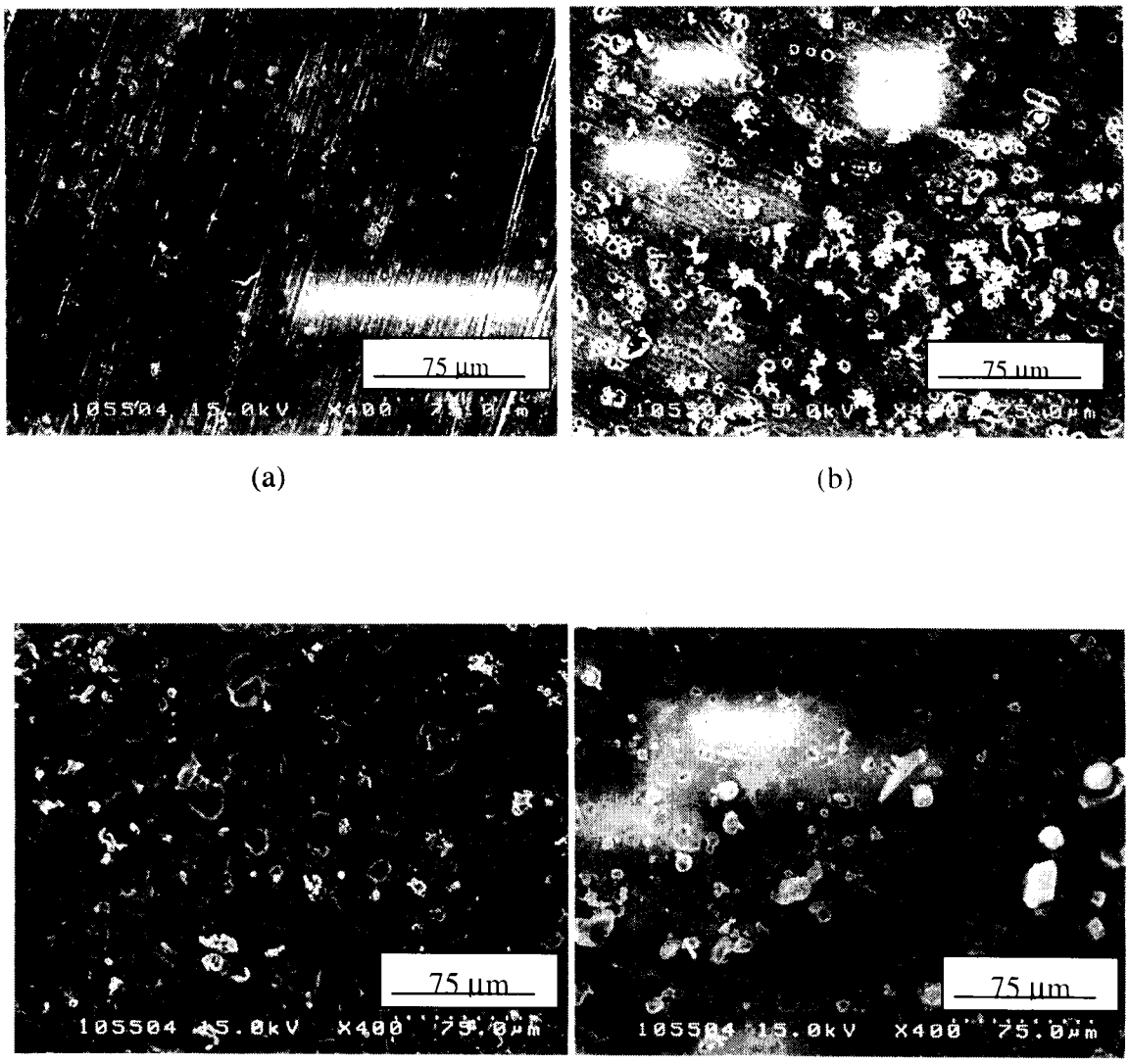

(a) (b)

(c) (d)

Figure 3.5 SEM micrographs from Al-2024 samples before immersion and corrosion tests (400x) (a) Sample A (MP only); (b) Sample B (1 min AE); (c) Sample C (3 min AE); (d) Sample D (10 min AE)

3.3.3 Polarisation Curve Measurements and Immersion Testing

Table 3.2 and Figure 3.6 show the results of the polarisation curve measurements performed on the various alkaline-etched samples (samples B, C, and D). The polarisation curves, for all samples tested, exhibit Tafel-like behaviour in both the anodic and cathodic arms, with E_{corr} below the pitting potential, which is near – 0.675 V. As the duration of the etching in NaOH increases, the measured values of i_o increase. This result indicates that the stability of the Al-2024 panels towards corrosion decrease with increasing alkaline etch times. Variations in the E_{corr} values may relate to differences in the amounts of copper present at the surface.

Immersion testing in 3.5 % (w/v) NaCl was performed on the various alkaline etched samples, and the resulting SEM micrographs are shown in Figure 3.7 (a) – (c). There is a clear trend from sample B (1 minute etch) to sample C (3 minute etch) to sample D (10 minute etch). Clearly, as the alkaline etching time is increased, the amount of corrosion product on the sample surface is also increased. This directly matches the trends observed from the polarisation curve measurements.

3.3.4 Discussion

Several factors caused by the alkaline etching are responsible for the increase in corrosion rate observed in the treated alloys. First, the purpose of the alkaline etching is to accelerate the conversion of the natural-borne aluminum oxide to the hydroxide, which ultimately disrupts the oxide film. This leads to the attack of the metal by the NaOH solution during the etching process, creating changes in the surface morphology as seen in the SEM micrographs taken prior to corrosion testing in Figure 3.5 [3.26, 3.27]. More

Table 3.2 Determined i_o values from polarisation curve measurements for Al-2024 samples given different treatments as specified in Figures 3.2 and 3.8

Sample	i_o (A/cm^2)
B	2.4×10^{-7}
C	3.0×10^{-7}
D	7.1×10^{-7}
E	2.0×10^{-7}
F	1.8×10^{-7}
G	8.0×10^{-8}

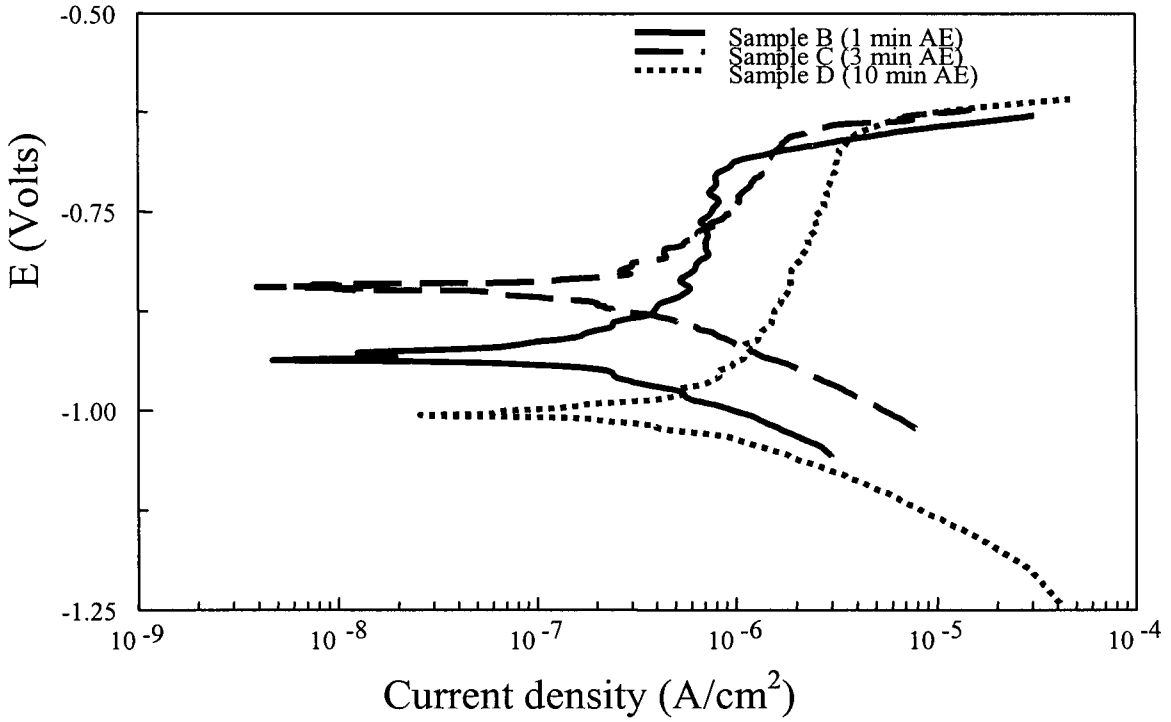

Figure 3.6 Polarisation curves measured for Al-2024 samples after various alkaline etching times

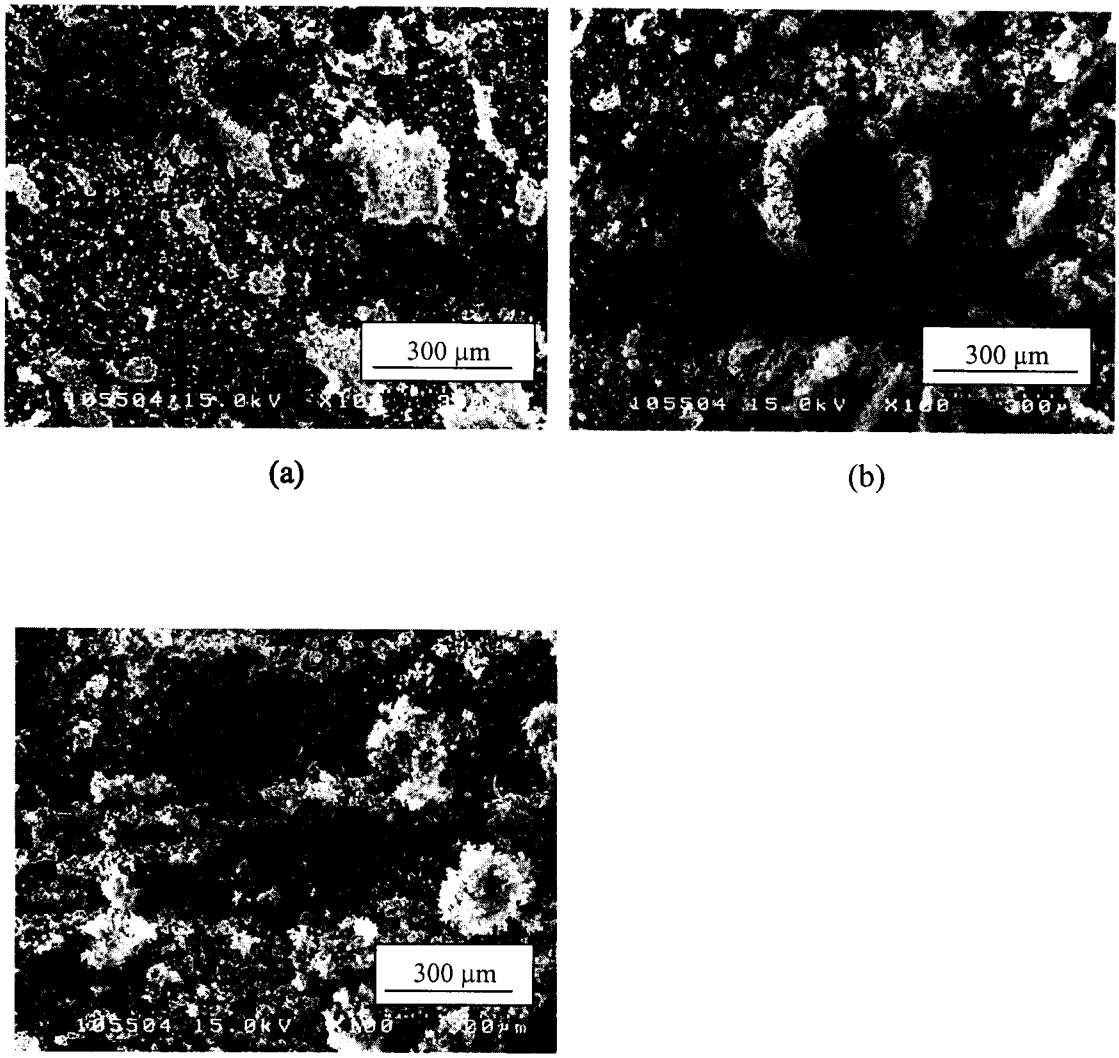

(a) (b)

(c)

Figure 3.7 SEM micrographs of bare Al-2024 alkaline-etched for different times after immersion testing (100x) (a) Sample B (1 min AE); (b) Sample C (3 min AE); (c) Sample D (10 min AE)

pits and crevices are created with longer alkaline etching times. These pits have been shown to promote the auto-catalytic corrosion of aluminum in NaCl solution by causing the H^+ ingress in crevices to counter the excess negative charge of Cl^- [3.26]. The trapped H^+ yields anodic corrosion (Al to Al^{3+}) with the evolution of H_2.

Finally, it has been hypothesized by others that alkaline etching may cause alloy enrichment. XPS results reported in Table 3.1 are consistent with this hypothesis. Several groups have also suspected that the alloy enrichment is a factor in increasing the corrosion rate, due to increased galvanic coupling and the possibility that the oxide film on the alloy provides less passivity. This may be due to the exposure of second-phase particles which have thinner, or non-existent, oxide layers above them, so making these areas more prone to attack [3.18 – 3.21].

However, while it is evident that a correlation between the duration of alkaline etching and the degree of copper enrichment exists, the polarisation test, while giving the electron transfer rates, does not specify the actual reaction occurring. Thus, it is difficult to know whether the auto-catalytic mechanism proposed by Fontana [3.26], or the effects of Cu enrichment is dominant [3.18 – 3.21]. Indeed it may be possible that changes in surface morphology and chemical composition, both as a result of alkaline etching, are responsible for the increase in the overall corrosion rate seen in samples that were pretreated with longer alkaline etching times.

3.4 Results: Effects of Silane Concentration on Silane Deposition onto Al-2024 Alloy

3.4.1 XPS Studies

Al-2024 samples were prepared according to the conditions that create sample B. This provides a "standardized" substrate from which to observe and measure the effects

of silane concentration on the amount of silane deposited and on the corrosion performance of the treated samples. A flowchart for the preparation procedures for the samples considered in this subsection is shown in Figure 3.8.

Figure 3.9 shows survey scans of selected samples prior to polarisation testing. The percent composition of elements on the substrate surface is reported in Table 3.3. For sample E (1% BTSE solution), the Si 2p peak is visible at 103.4 eV so indicating the presence of the adsorbed silane. Also, the oxide Al 2p peak detected at 75.6 eV indicates that the silane coating is less than around 60 Å thick [3.17]. As the concentration of the silane solution is increased with samples F (4% BTSE) and G (10% BTSE), the Al 2p peak is no longer detected, and this is consistent with the production of thicker coatings. Consistently, the Si/Al ratio from the coated samples increases with the BTSE solution concentration.

3.4.2 Polarisation Curve Measurements and SEM Studies

Table 3.2 and Figure 3.10 report the results of polarisation tests performed to assess the corrosion performance of the coated samples E, F, and G compared with sample B. The polarisation curves have cathodic arms that exhibit Tafel behaviour, so enabling values of i_o to be measured. As it is seen from Table 3.2, samples that were coated with a BTSE solution generally have lower exchange current densities, i_o, than samples that were not coated with silane. Further, the corrosion inhibition appears to increase with the BTSE solution concentration, when all other parameters are fixed. This indicates that increasing the amount of silane on the Al-2024 substrate favours passivation, and hence a lowering in the corrosion rate. SEM micrographs taken from

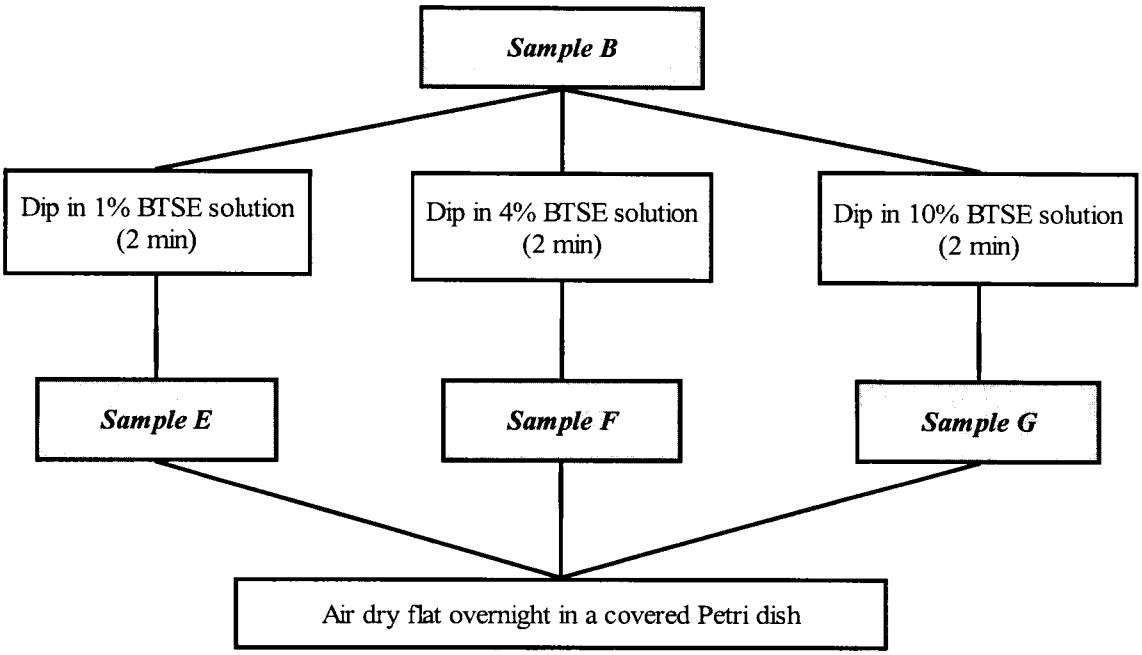

Figure 3.8 Flowchart of procedures and sample designations used to study the effects of different BTSE silane concentrations for deposition on Al-2024

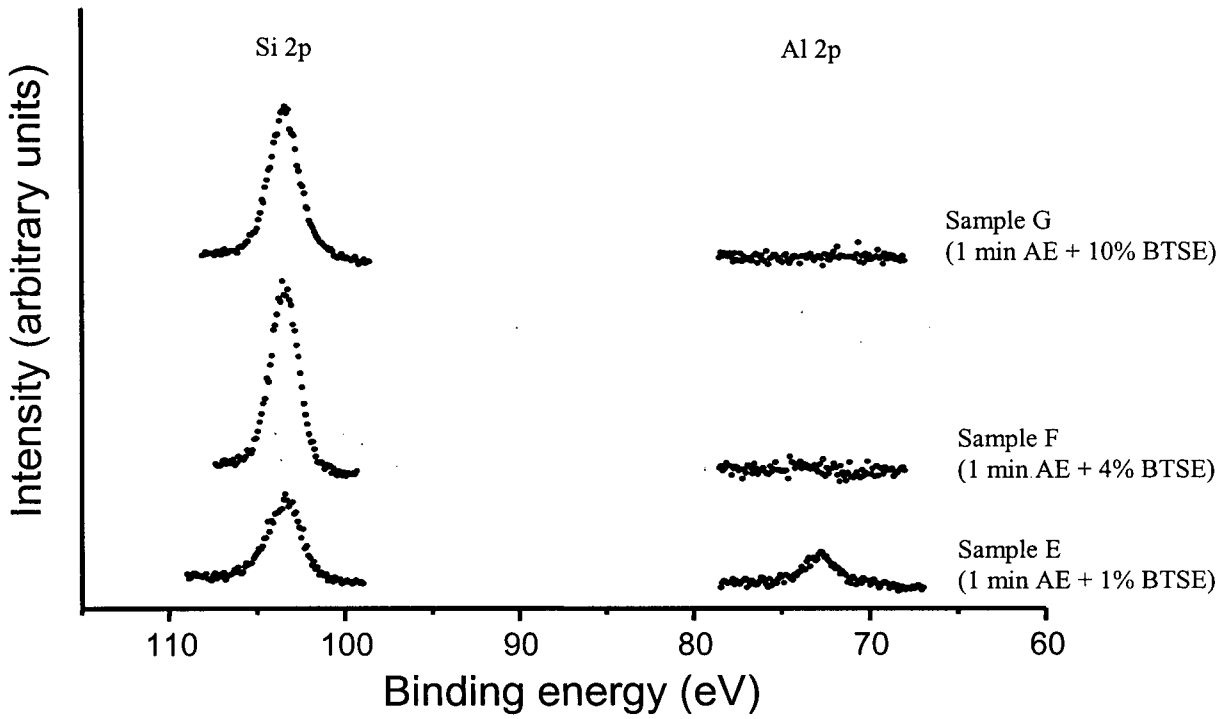

Figure 3.9 Si 2p and Al 2p spectra from Al-2024 samples coated with different silane solutions

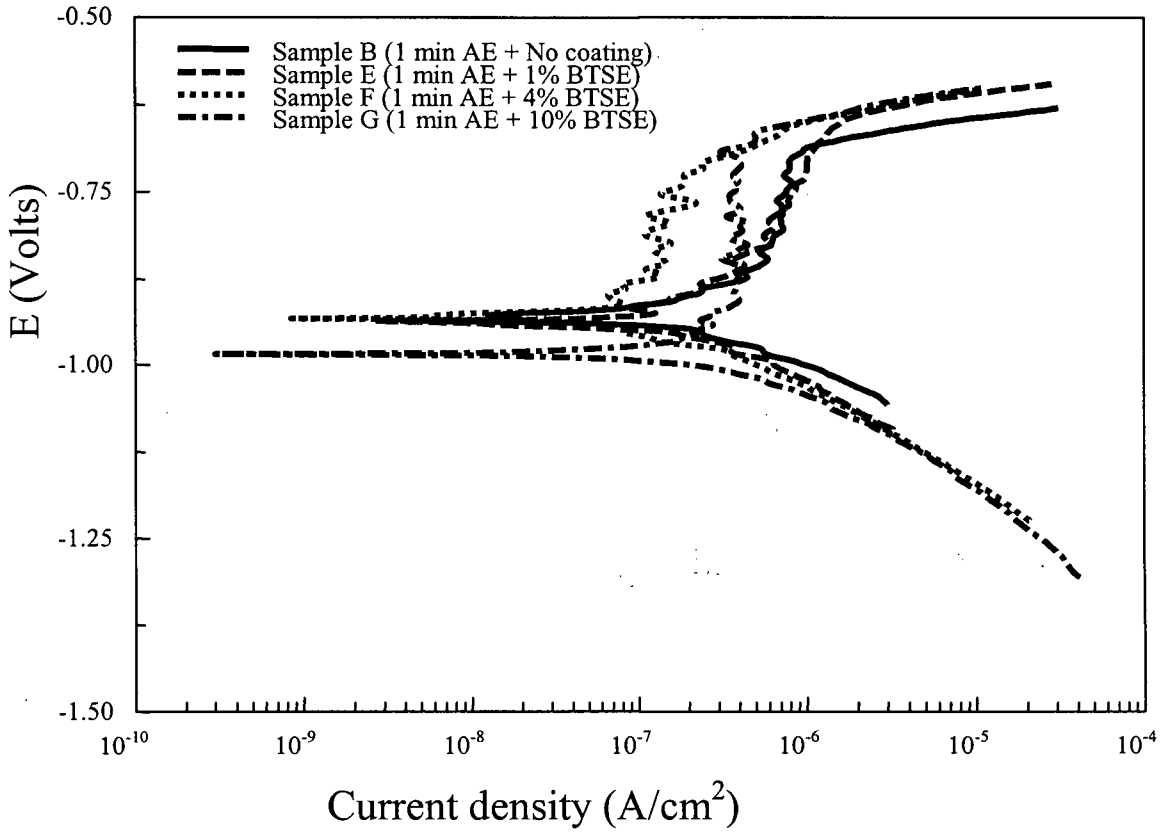

Figure 3.10 Polarisation curves measured for Al-2024 samples after coating with BTSE solutions of different concentrations

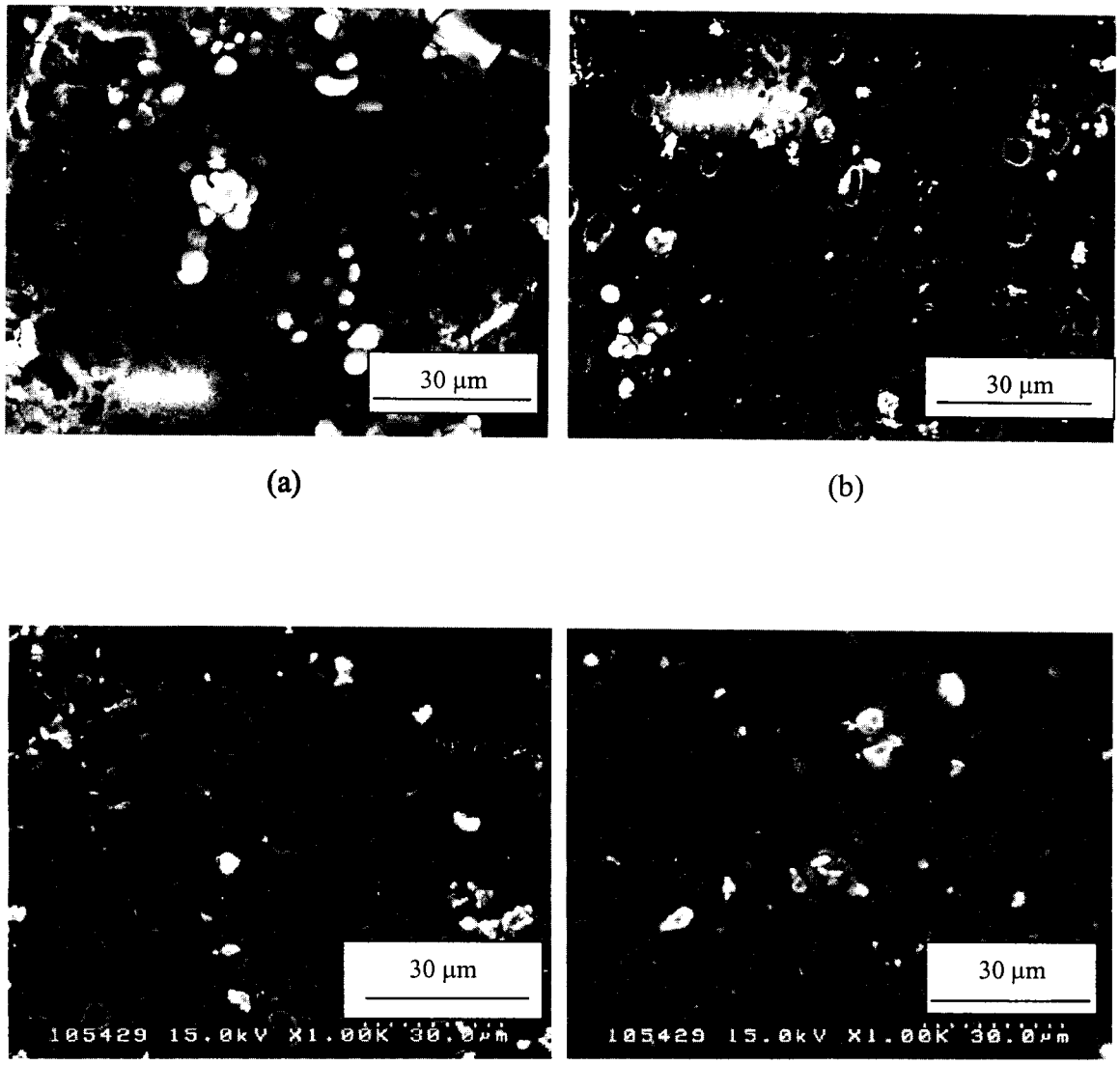

Figure 3.11 SEM micrographs of silane-coated Al-2024 after polarisation tests (1000x) (a) Sample B (1 min AE + No coating); (b) Sample E (1 min AE + 1% BTSE); (c) Sample F (1 min AE + 4% BTSE); (d) Sample G (1 min AE + 10% BTSE)

samples after polarisation curve measurements are shown in Figure 3.11 (a) – (d). By comparing the frequency and severity of the pits, as well as the amount of corrosion product, it is seen that less corrosion product occurs on samples with more silane deposition. This again is fully consistent with the results reported above from the polarisation curve measurements and XPS experiments.

3.4.3 Discussion

Results in this section demonstrate that deposited BTSE can act as a corrosion inhibitor on Al-2024, and that increasing the BTSE concentration in the coating solution will create a thicker film, or at least lead to better coverage on the substrate. All of this is consistent with the collective work of Van Ooij who has demonstrated the potential of BTSE as a corrosion inhibitor for other metals [3.28 – 3.33]. Higher BTSE concentrations in solution are believed to give more cross-linking and thicker films, as demonstrated by the XPS results obtained in this section. These results are consistent with similar observations demonstrated previously by Van Ooij who has shown for γ-APS, using ellipsometry measurements, that the amount of silane deposited on the substrate was dependent primarily on the silane concentration [3.1, 3.2]. Underhill et al. have demonstrated the same concept using γ-GPS [3.9 – 3.13].

3.5 Results: Effects of Different Pretreatments on Silane Coating Effectiveness

3.5.1 XPS Studies and Polarisation Curve Measurements

The Al-2024 samples considered in this sub-section were prepared according to the procedures shown in Figure 3.12. Measured Si 2p and Al 2p photoelectron spectra from a selection of these samples are shown in Figure 3.13. Sample E has been alkaline

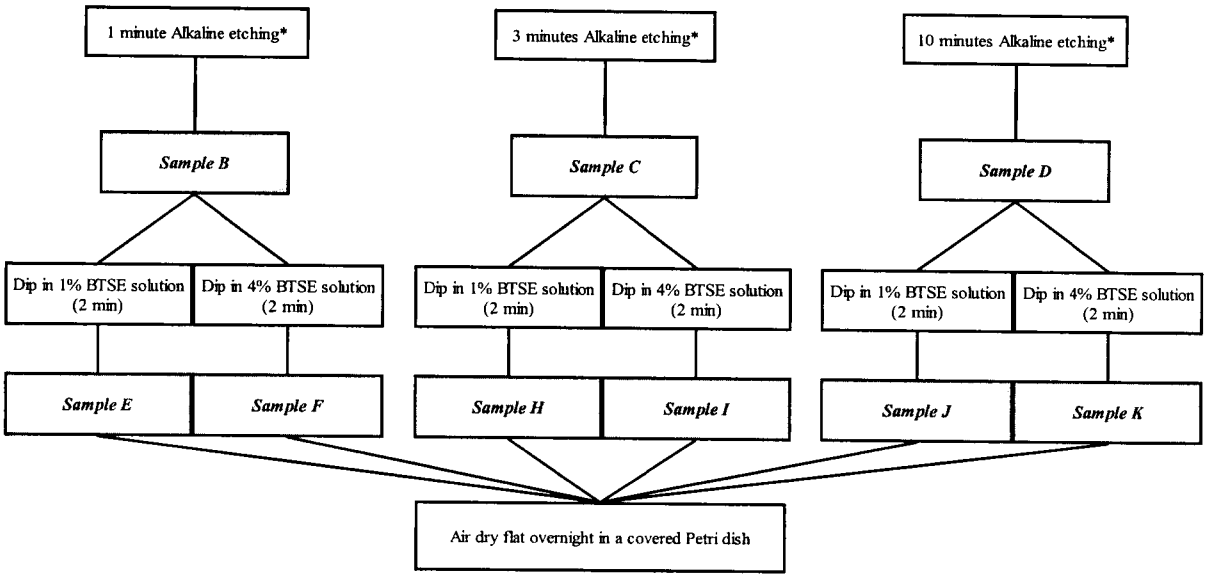

* Complete specification of samples B, C, and D are given in Figure 3.2

Figure 3.12 Flowchart of procedures and sample designations used to study the effects of different pretreatments on BTSE deposition on Al-2024 samples

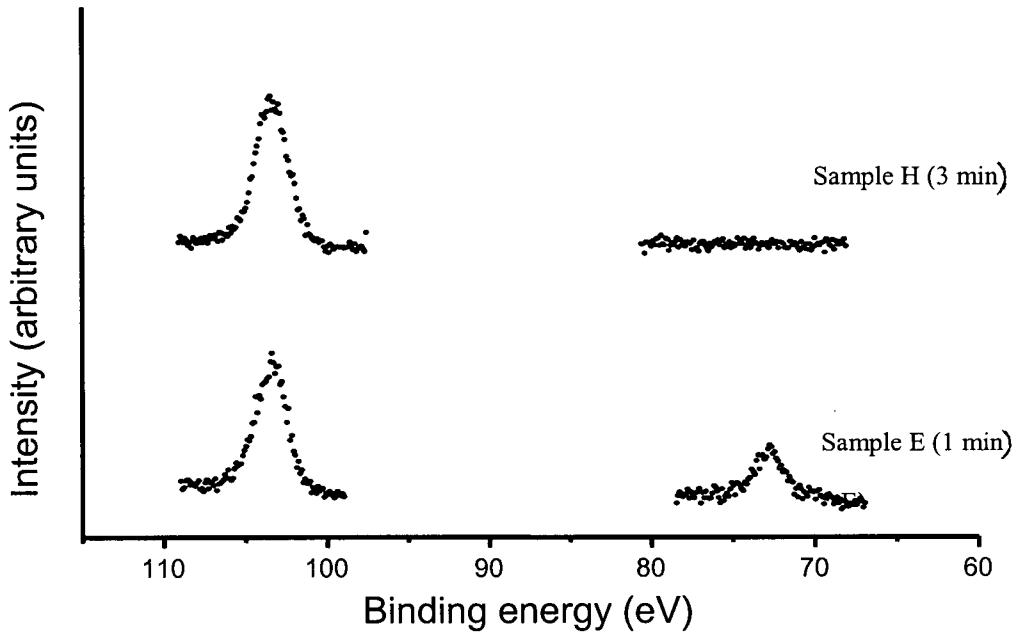

Figure 3.13 Si 2p and Al 2p spectra from Al-2024 samples alkaline etched for different times followed by coating with 1% BTSE solution

etched for 1 minute, and it shows both the Si 2p peak at around 103.4 eV and the Al 2p peak at around 75.6 eV. These observations show that the silane coating must be quite thin since the Al 2p peak can still be detected. With sample H, the alkaline etching was done for 3 minutes and then coated with the 1% BTSE solution. However, the Al 2p peak is not now detected by XPS, and that indicates the presence of a thicker coating. This observation emphasizes the importance of the length of the alkaline etch in preconditioning a surface for BTSE deposition.

Figure 3.14 reports polarisation curve measurements for samples which have been alkaline etched for different times, and then dipped in 4% BTSE for a fixed time, to observe the effects of etching time on silane deposition and possible corrosion protection. Sample F, alkaline-etched for 1 minute before coating, has a measured E_{corr} value (~ -0.91 V) and a cathodic arm that exhibits Tafel behaviour. Samples I and K, etched for 3 and 10 minutes, respectively, prior to silane deposition, however, have cathodic arms that do not follow Tafel behaviour, and the measured E_{corr} values for these samples are very close to the pitting potential (~ -0.67 V). Thus, i_o cannot be measured. A similar observation was seen with the samples dipped in the 1% BTSE solution (Figure 3.15), where any sample etched longer than 1 minute, and then coated with silane, did not exhibit Tafel behaviour. This makes the measured polarisation curves less helpful for assessing the effects of changing parameters on corrosion stability.

3.5.2 Discussion

XPS spectra for experiments performed in Section 3.5 to observe the interrelationship between changes in alkaline etching time and silane deposition are

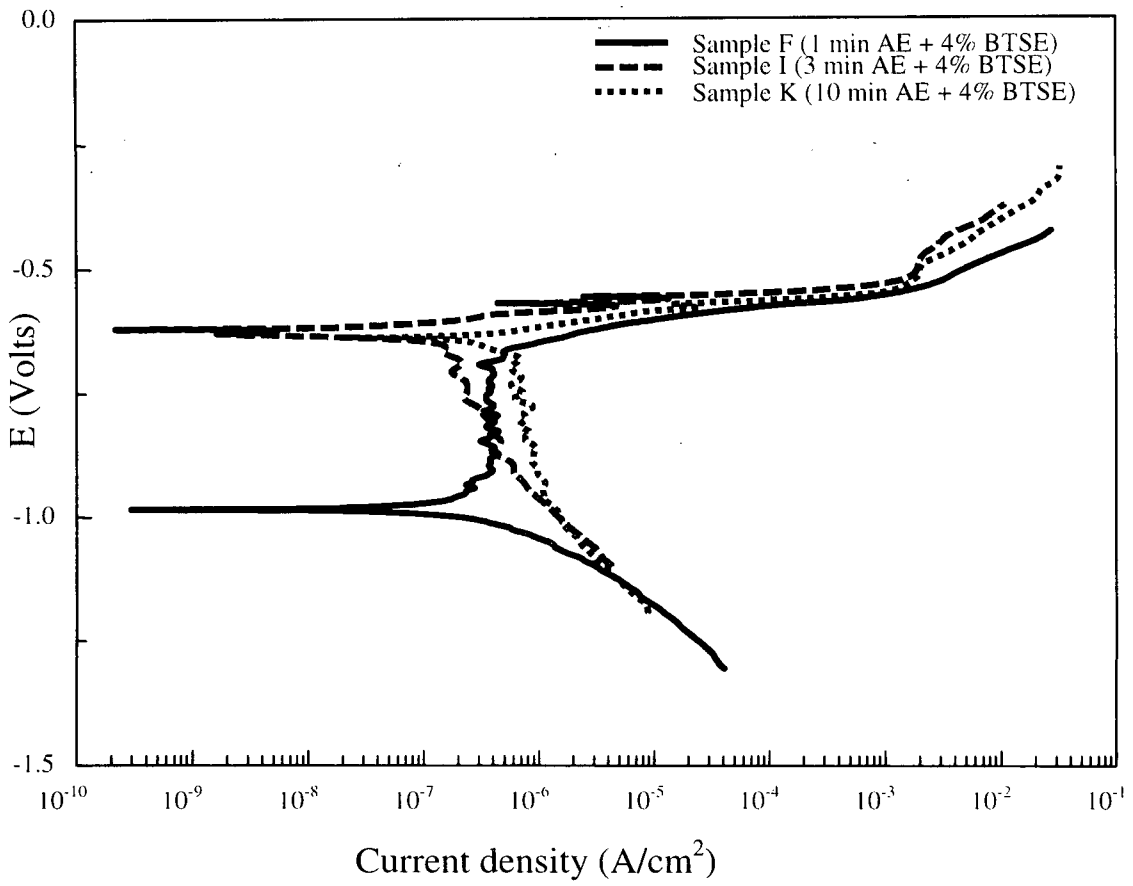

Figure 3.14 Polarisation curves measured for Al-2024 samples after etching for different times followed by coating with 4% BTSE solution

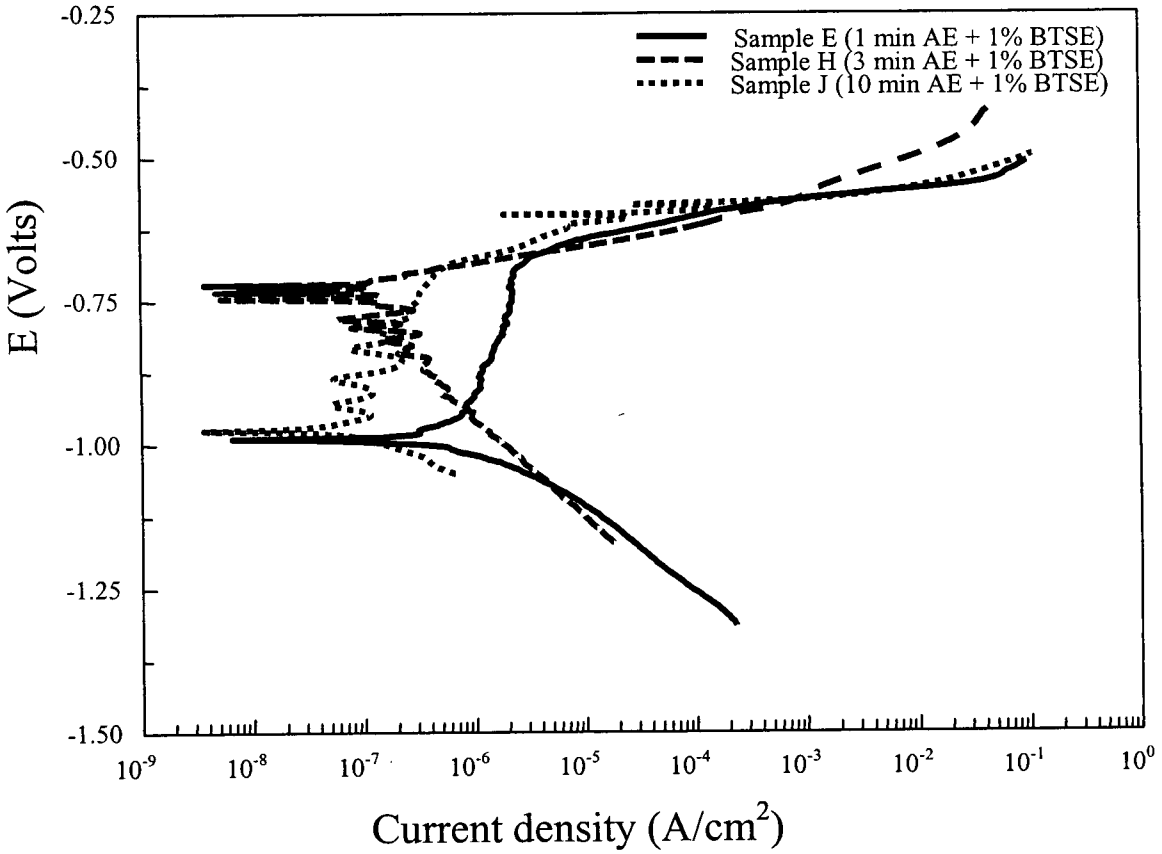

Figure 3.15 Polarisation curves measured for Al-2024 samples after etching for different times followed by coating with 1% BTSE solution

consistent with theories proposed by Venables and Hulser [3.22, 3.27]. While both researchers agree that increasing the alkaline etching time creates conditions that allow more silane to be deposited onto the surface from the same solution, each has his own view as to why.

Venables reports that a rougher surface morphology allows for more silane to be deposited with better mechanical interlocking to the substrate surface. Section 3.3 has demonstrated that increasing the alkaline etching time changes the surface morphology and creates more pits and crevices. Consistently, with the theory of Venables, XPS results reported here show that more silane is deposited on a sample which has been alkaline etched for a longer time (sample H vs. E). Hulser, on the other hand, believes that an increase in alkaline etching time produces more nucleation sites (etching products) for a coating to bond to. This is also consistent with the XPS results reported.

The differences between the theories of Hulser and Venables should be seen more in terms of the nature of the silane bonding. Indeed, the etching products considered by Hulser may be chemically similar to the pits and crevices considered by Venables, as they both contain metal hydroxyl groups to which a coating can bond to [3.1, 3.2]. However, Hulser emphasizes direct bonding between the coating and metal hydroxyl groups on etching products poorly-bonded to the substrate [3.22], whereas Venables believes that the silane is bonded to metal hydroxyl sites firmly anchored in the substrate oxide layer [3.27]. XPS results alone cannot distinguish between these two possible situations.

In an attempt to determine the effectiveness for corrosion protection of BTSE deposited onto Al-2024 for longer etching times, with a constant silane concentration,

polarisation curves were measured. However, the results are inconclusive insofar as Tafel behaviour was not observed and hence i_o values could not be determined. Increasing the alkaline etching time does lead to conditions where more BTSE is deposited on the Al-2024 substrate from the same silane solution, but it is not yet clear whether this "enhanced" silane deposition aids in the passivation of the substrate. Equally, it is not known why the polarisation curves measured for samples etched for durations longer than 1 minute do not exhibit Tafel behaviour for the 1% and 4% BTSE solutions reported in Figures 3.14 and 3.15, but it is considered further in Chapter 4.

Chapter 4 Effects of Nitric Acid Treatment Times on BTSE Bonding to Al-2024 Alloy

4.1 Introduction

Section 3.5 has shown that increasing the alkaline etching time in the pretreatment step creates conditions where more silane can be deposited on Al-2024 alloy using a constant BTSE solution. However, polarisation curve measurements were inconclusive as to whether the longer etching times produce a more corrosion-resistant coating. Thus, a fundamental question must still be answered: With the longer etching times, was all the silane deposited securely bonded to the substrate? If not, then using the amount of silane detected on the surface to assess the coating's potential performance, as done in Section 3.4, may have a weakness insofar as it does not provide a true gauge of the amount of securely-bonded silane.

According to the Pape and Van Ooij theories, silanes bond to metals via condensation reactions to surface hydroxide groups. In principle, more free hydroxyl groups can be created by increasing alkaline etching, and this can lead to more silane deposited onto the substrate surface [4.1 – 4.3]. Section 3.3 has shown that increasing the alkaline etching time increases the amount of loosely-bound etching products with more free hydroxyl groups, that act as nucleation sites for bonding to organic coatings [4.4, 4.5]. More coating is deposited onto this substrate as demonstrated in Section 3.5. However, to make a stable coating, the silane should be bonded to metal hydroxyl groups in the substrate oxide layer rather than to loose etching products on the surface. An ideal alkaline-etching pretreatment, prior to the silane deposition, should therefore minimize

the amount of etching product formed in the first place, while optimizing the sites at the oxide surface for bonding to the silane.

HNO_3 is used in industry after the alkaline etching step to remove weakly-bound aluminate, the etching product, on aluminum alloys [4.6]. In addition, this desmutting step is known to remove many second-phase particles responsible for alloy enrichment [4.7]. Recent studies have also shown that NO_3^- has been successfully added to anodising agents, such as H_2SO_4, to enhance the thickness and hardness of the oxide layer. Additionally, it is known that NO_3^- in acid, is itself an anodizing agent [4.8].

The objectives of this chapter are:

(i) to examine the effects of varying the HNO_3-treatment time on the bonding characteristics of BTSE to Al-2024 which had been alkaline-etched for 1 minute in NaOH (to minimize the amount of corrosion product formed); and

(ii) to investigate the effect HNO_3 has on the Al-2024 alloy surface prior to coating with BTSE.

All of this is done to study the silane bonding at the metal oxide-to-coating interface in order to optimize the alkaline etching process for maximizing the securely-bonded BTSE deposited onto the Al-2024 surface. This, in turn, should lead to increased corrosion resistance imparted to the treated alloy.

4.2 Experimental

Figure 4.1 gives the experimental procedures, sample preparations, and sample designations used for the sonicating test to examine the BTSE bonding on the different pre-conditioned Al-2024 surfaces.

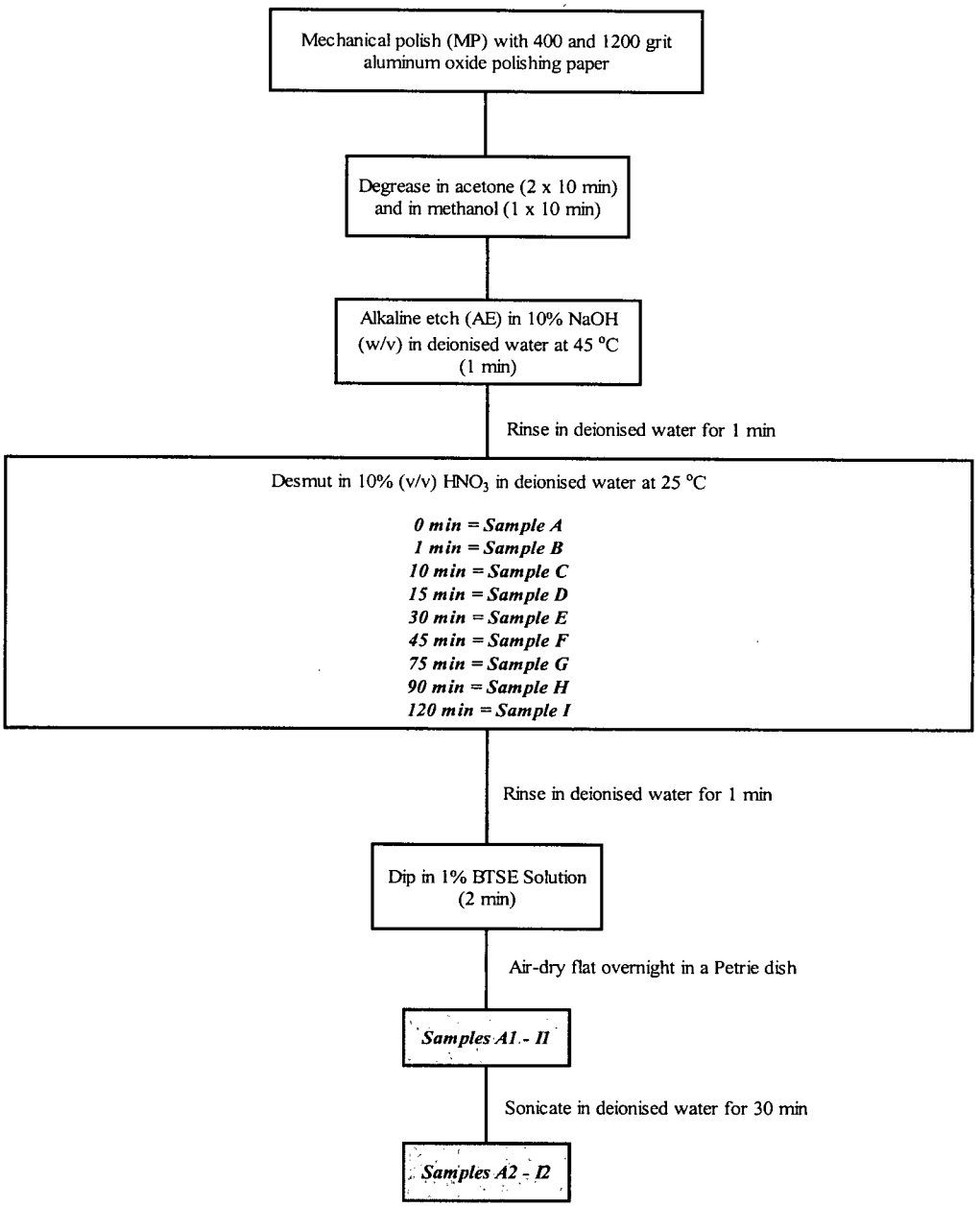

Figure 4.1 Experimental procedure flowchart, with sample designations, for studying the effects of HNO_3 treatment time on silane bonded to Al-2024

1% BTSE solutions were prepared according to the methods specified in Chapter 3. XPS spectra of samples were scanned and analysed according to the specifications set in Chapter 2. The Mg Kα source (1253.6 eV) was used with an emission current of 20 mA at 10 kV. SEM micrographs were scanned according to the parameters set in Chapter 3.

4.3 Results: Effects of Nitric Acid Treatment Time on BTSE Bonding to Al-2024 Alloy

4.3.1 XPS Studies

Various samples were prepared according to the designations in Figure 4.1. Figure 4.2 is a labeled survey scan of a typical sample prior to sonicating. Major photoelectron peaks present include C 1s, C Auger peak, Si 2p, Si 2s, O 1s and an O Auger peak. In all cases, a strong Si 2p signal is detected around 103.4 eV, and this indicates the presence of silane adsorbed on the surface. In addition, a small, but definite, Al oxide signal from the substrate is detected at 75.6 eV [4.9]. This indicates that the deposited film on the substrate is less than about 60 Å thick. Other HNO_3-treated samples (B1 – I1) revealed similar spectra to that shown in Figure 4.2. This indicates, that prior to sonicating, all the HNO_3-treated samples have comparable amounts of silane adsorbed on the substrate surface.

A parallel set of samples were prepared, and then sonicated for 30 minutes in deionised water (A2 – I2). This serves to test for the strength of the silane bonding to the Al-2024 surface. Since the silane film is chemically inert to water, any silane remaining on the surface after the sonication is more securely-bonded than that which is lost.

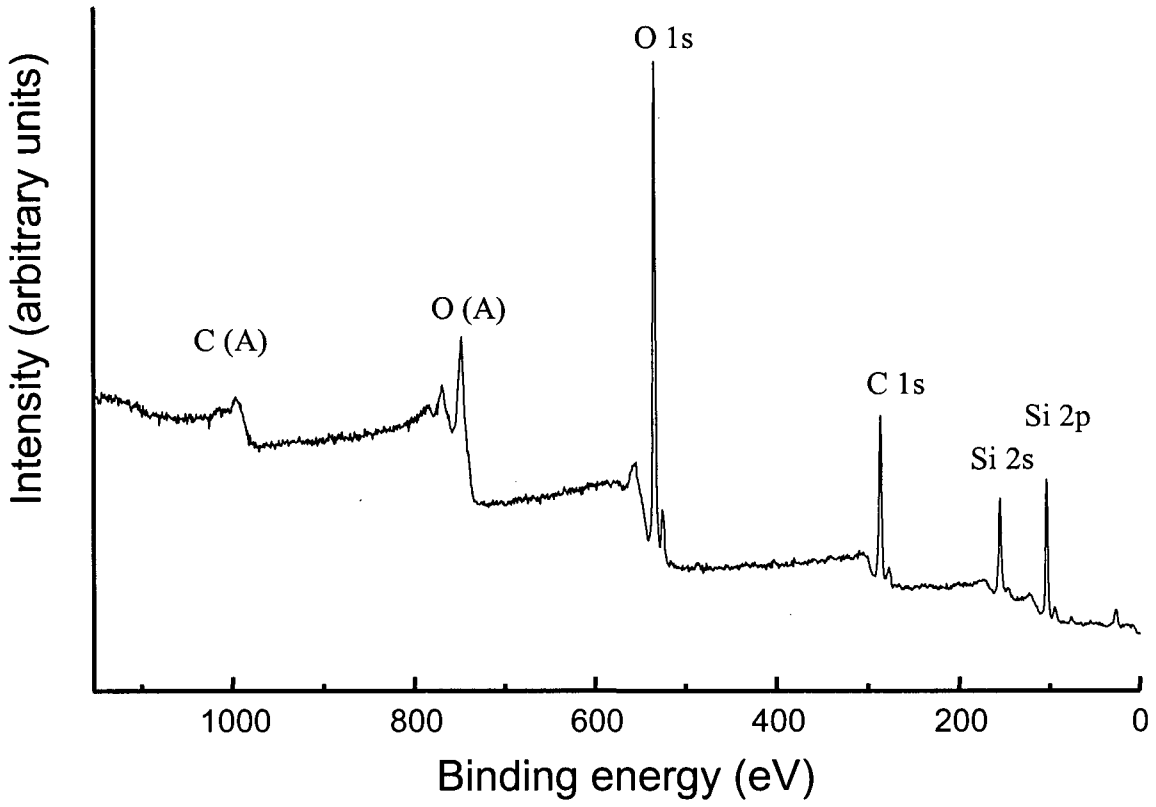

Figure 4.2 XPS survey scan from a typical Al-2024 sample coated with 1% BTSE before sonicating

Figure 4.3 shows selected survey scans for various HNO_3 treatment times before and after sonicating. Figure 4.3 (a) shows samples A1 and A2, treated for 0 minutes in HNO_3. For sample A2, a high intensity Al 2p peak is detected at 75.6 eV, but no Si 2p peak at 103.4 eV. This indicates the presence of Al oxide from the substrate, and the fact that all the BTSE was removed from the sample after sonicating.

Figure 4.3 (b) shows a comparison of survey scans from samples E1 and E2, treated in HNO_3 for 30 minutes prior to BTSE deposition. These spectra are virtually identical, so indicating that essentially all of the BTSE remains adsorbed on the substrate after the sonication.

Figure 4.3 (c) shows a comparison of the survey scans from samples I1 and I2, where the HNO_3 treatment is for 120 minutes prior to the BTSE deposition. The Al oxide peak is clearly seen in the spectrum of sample I2, indicating that a significant amount of the silane was removed. However, there is still a prominent Si 2p peak present after sonicating, so indicating that some BTSE is still adhered.

Semi-quantitative results to determine the amount of silane adsorbed, after the sonication, were assessed by measuring higher-resolution spectra for the Si 2p and Al 2p peaks. In Figure 4.4, samples B2 and C2 still have significant Al 2p peaks and lower Si/Al ratios compared to most of the other samples. Sample D2, treated with HNO_3 for 15 minutes, appears to have significantly more silane left on the substrate, since the Al 2p peak is less prominent. Sample E2, treated with HNO_3 for 30 minutes, appears to correspond to the optimal HNO_3 treatment time for the systems tested. For example, Table 4.1 shows that this sample has the highest Si/Al ratio after sonication.

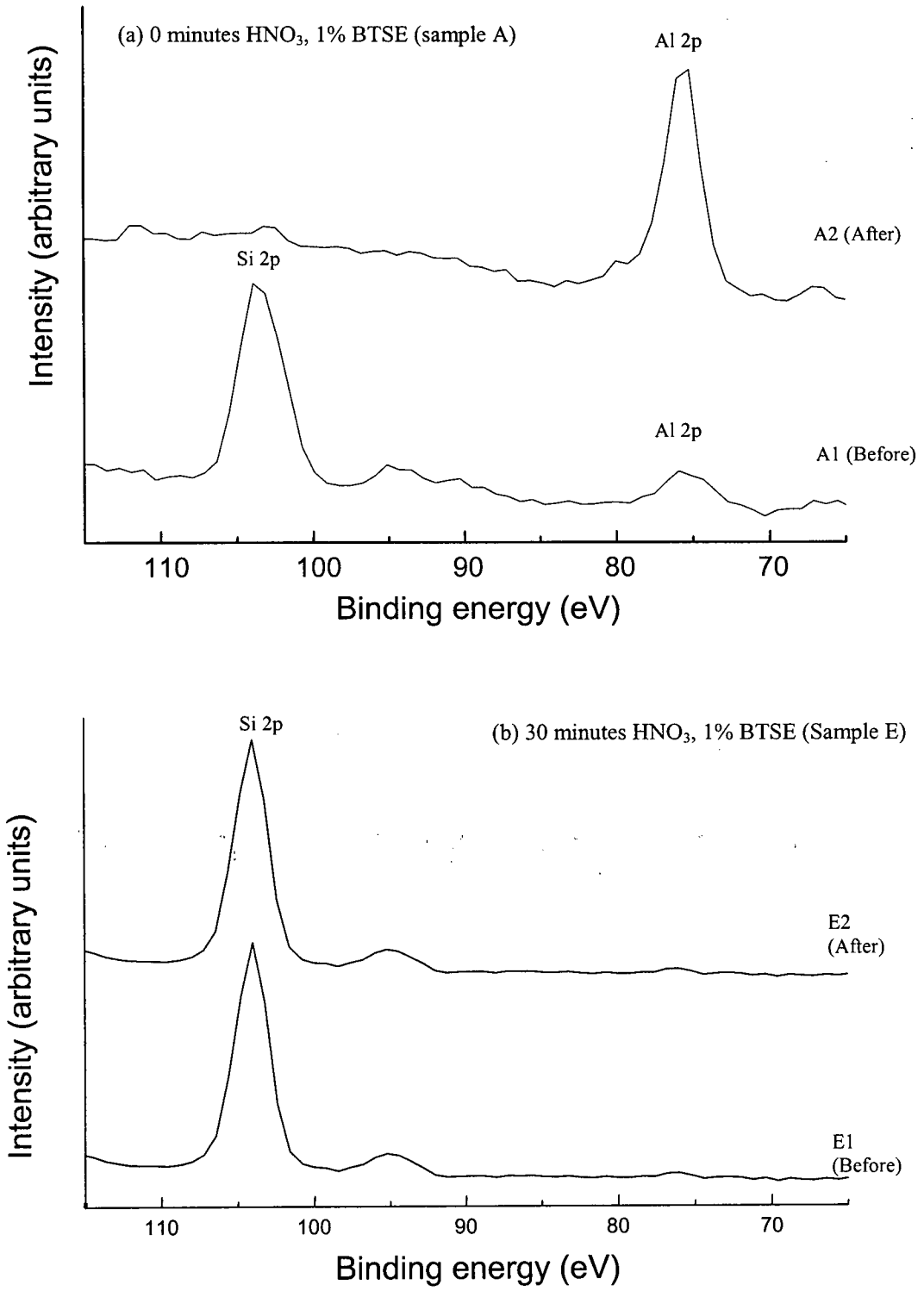

Figure 4.3 Survey scans of samples before and after sonicating for selected samples (a) A, (b) E, and (c) I

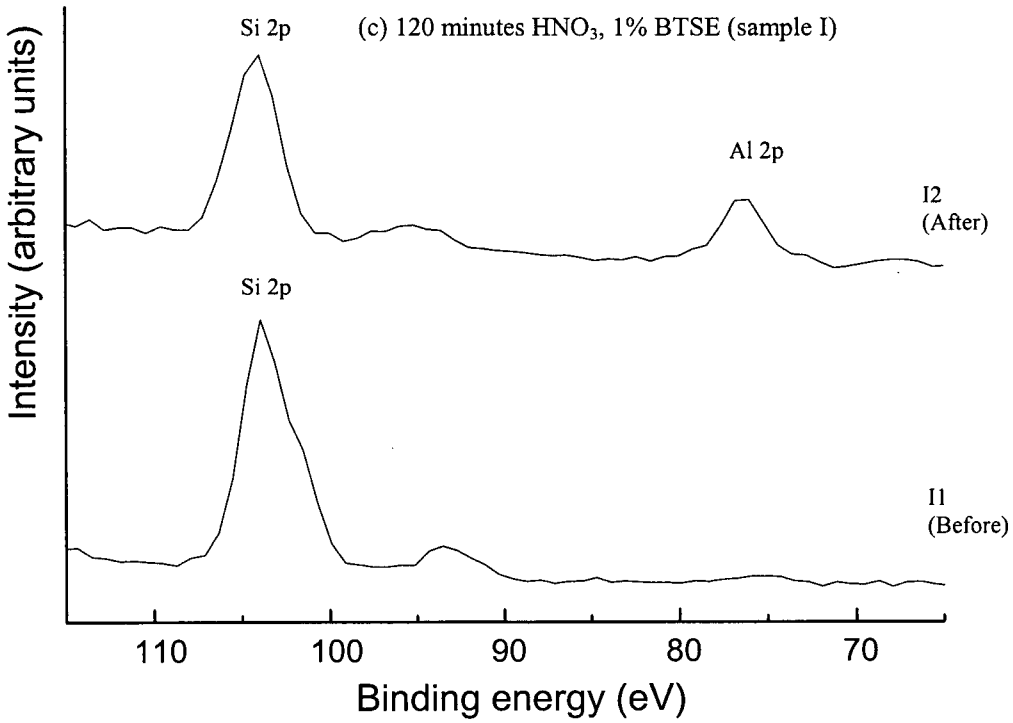

Figure 4.3 continued

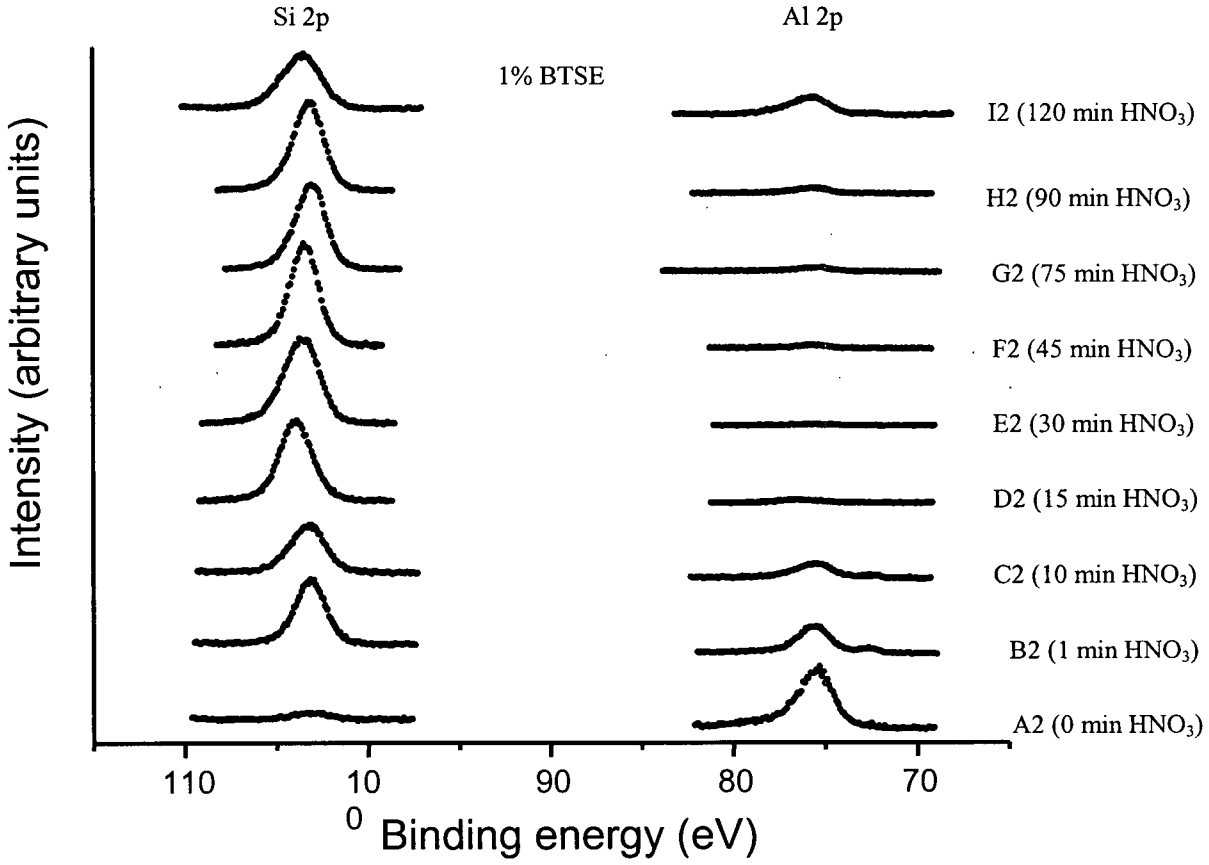

Figure 4.4 Si 2p and Al 2p peaks of various samples after sonicating

Table 4.1 Si/Al ratios of silane-coated samples after sonicating tests

Sample *	Si/Al
A2	0.0
B2	1.3
C2	1.8
D2	13
E2	34
F2	22
G2	12
H2	9.4
I2	1.8

* Sample preparation and designations are described in Figure 4.1

For more than 30 minutes of sonicating, the Si/Al ratio is shown to gradually decrease through the samples F2 to H2. This indicates that the amount of silane remaining on the substrate after sonicating actually decreases if the substrate is left in the HNO_3 dip for longer times. The very long HNO_3 treatment (120 minutes) does not promote effective silane bonding to the alloy surface, as shown by sample I2.

4.3.2 Discussion

The results from this set of experiments on pretreated Al-2024 surfaces indicate that a suitable working range for the HNO_3 dip for creating securely-bonded silane films is to treat the surface for 15 to 90 minutes in HNO_3, with the optimum treatment time being about 30 minutes. In general, some of the silane deposited was removed by sonication in pure water, meaning that only part of the silane deposited is strongly bonded to the surface. It therefore follows that the amount of silane measured prior to testing can be a misleading indicator of the potential performance of the coating where, for the experiments in this section and in Section 3.5, the concentration of the BTSE solution was kept constant.

The question to ask now is: What is happening on the Al-2024 substrate surface, after the HNO_3 treatment, to cause these observations for the deposition of BTSE.

4.4 Results: Effects of Nitric Acid on Uncoated Al-2024 Alloy Etched with NaOH

4.4.1 XPS Studies

Selected Al-2024 samples were immersed in 10% (w/v) NaOH for 1 minute and in 10% (v/v) HNO_3 for various durations. A flowchart for the procedures used is shown in Figure 4.5.

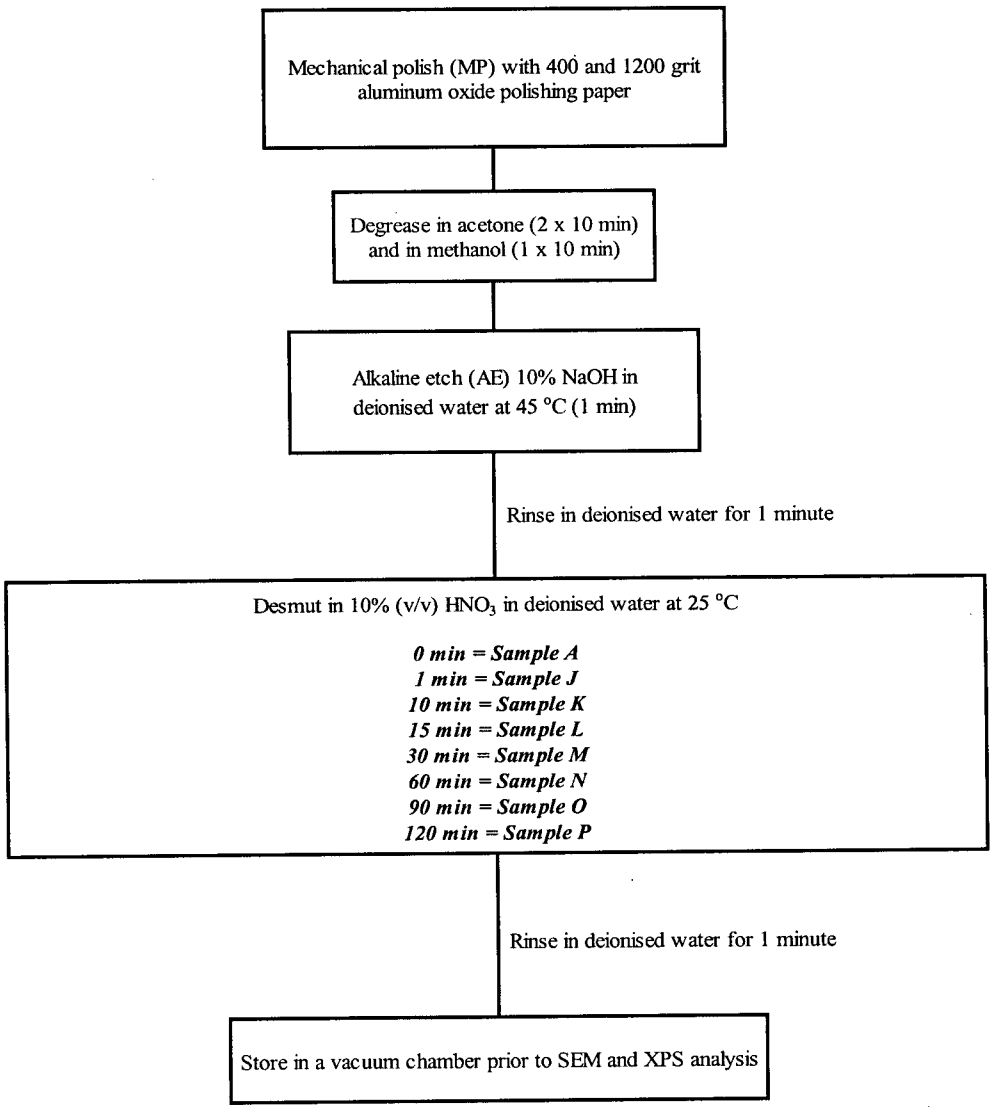

Figure 4.5 Experimental procedure flowchart, with sample designations, for studying the effects of HNO_3 treatment time on Al-2024

Figure 4.6 (a) shows the Al 2p peak for sample A, which was not treated in HNO_3. There is only one peak present at 75.6 eV, indicating the presence of oxidized aluminum, and that the oxide layer must be at least 60 Å thick. The full-width-at-half-maximum (FWHM) value for this peak (1.9 eV), is larger than that (1.7 eV) seen in Figure 4.6 (b) for sample M (treated for 30 minutes in HNO_3). This indicates either there are two types of oxide present or there is some peak broadening because of sample charging [4.10]. The sonicating tests in Section 4.3 show that the silane washes off the substrate, an observation that suggests the BTSE is adsorbed on loosely bound etching product formed during the alkaline etching.

Figure 4.6 (b) shows the Al 2p peak for sample M, treated for 30 minutes in HNO_3. Again, the oxide peak at 75.6 eV is seen, but this appears different from that of sample A. Sample M has a shiny metallic colour, rather than black as seen for sample A, and the FWHM value for the Al 2p peak is smaller. Sample M's oxide layer must also be at least 60 Å thick as no metallic signal is detected. This oxide is the passive oxide, $Al_2O_3 \cdot 3H_2O$ [4.9], and the sonicating tests, in the previous section, indicate that BTSE bonds well to this oxide.

Figure 4.6 (c) shows the Al 2p spectrum for sample P, which has been treated for 120 minutes in HNO_3. Now two peaks are detected. The first is the oxide peak at 75.6 eV for which the FWHM value (1.9 eV) is again greater than that of sample M (1.7 eV). The second peak at 72.7 eV indicates the presence of metallic Al (which is not seen in samples A or M). The oxide-to-metal ratio is decreased for sample P, compared to sample M, indicating that the former has a thinner and more uniform oxide layer. Results from the sonicating tests are consistent with this model since the silane bonded to the adhered

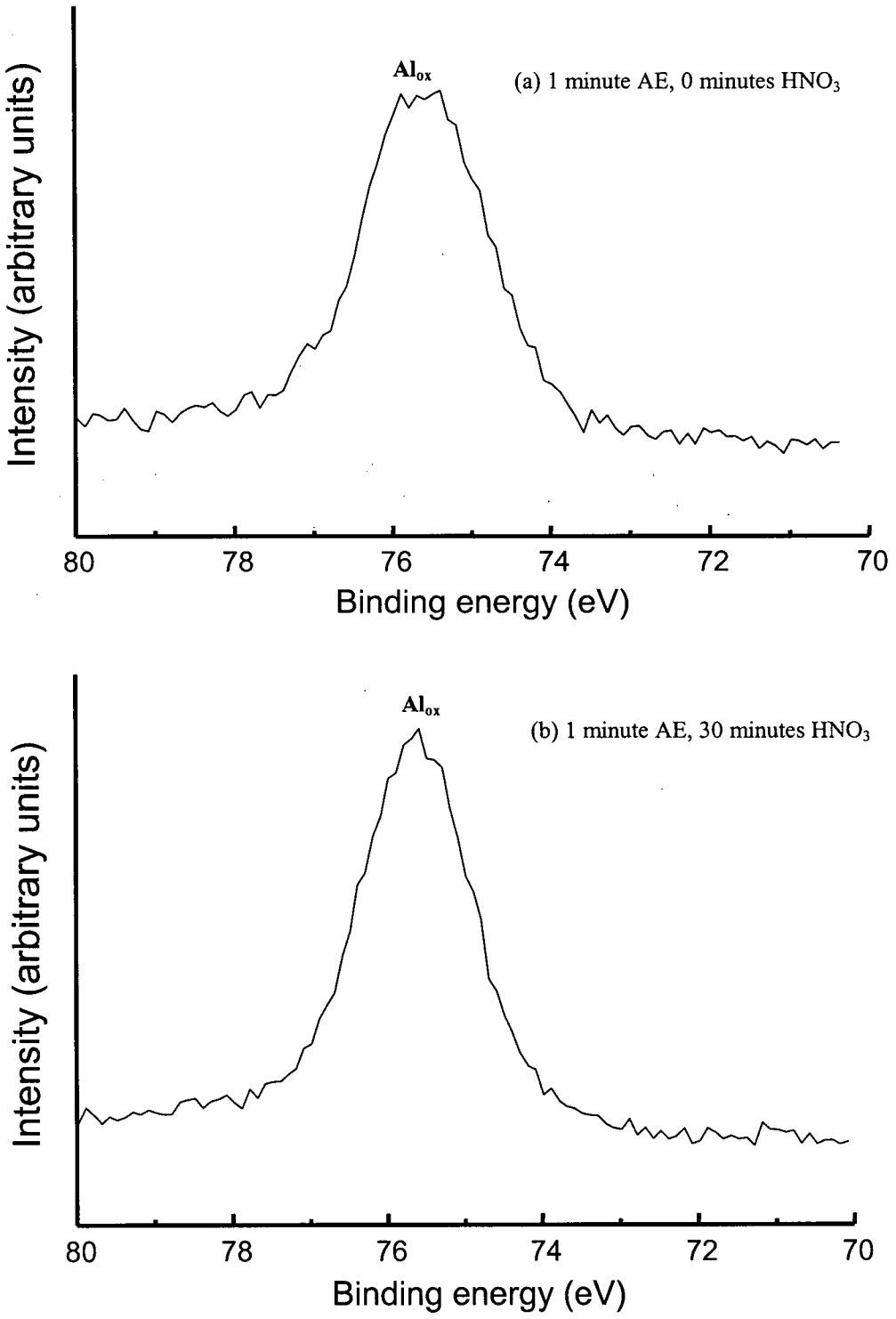

Figure 4.6 Al 2p spectra from samples: (a) A, (b) M, and (c) P

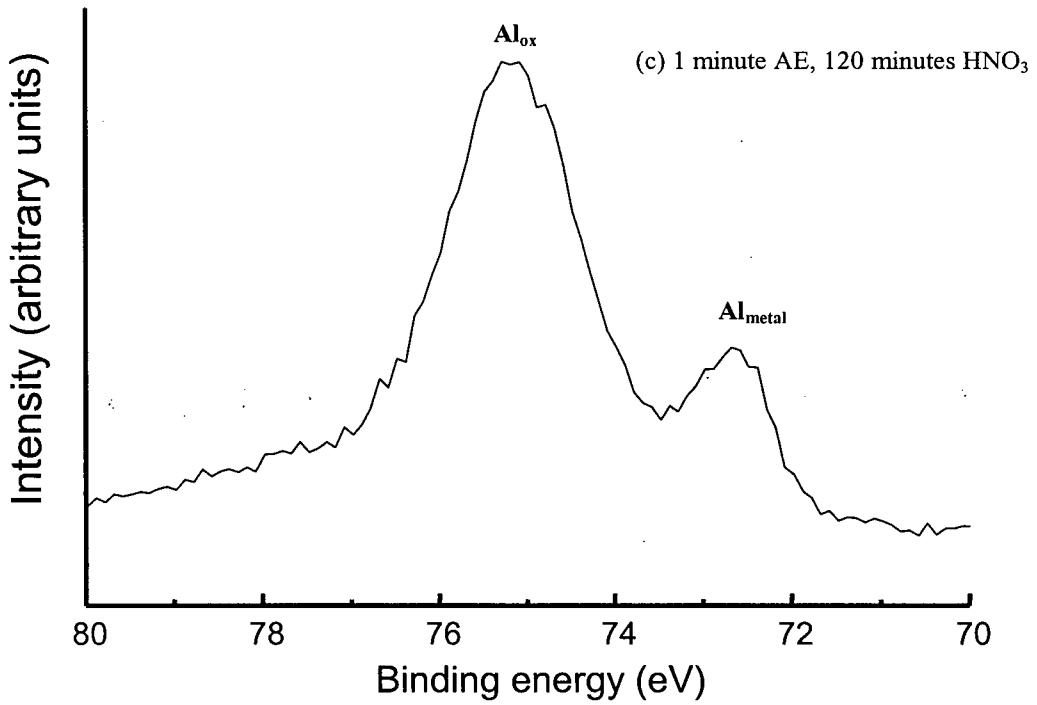

Figure 4.6 continued

oxide layer is secure, whereas any silane bonded to the more corroded product was removed easily.

4.4.2 SEM Studies

Figures 4.7 (a) – (h) show SEM micrographs taken from panels treated in HNO_3 for various times. Figure 4.7 (a) for sample A shows the presence of etching product, which is consistent with the XPS results shown in Sections 4.3.1 and 4.4.1. Figures 4.7 (b) to (d) show images of samples J, K, and L, which have been treated in HNO_3 for 1, 10, and 15 minutes, respectively. The aluminate is removed, and the lines from the mechanical polishing step are seen. Some etching product remains on the surface; however, as the HNO_3 treatment times increase, less etching product is seen and the pitting frequency also decreases. Again, this appears consistent with the observations in Section 4.3.1.

Figures 4.7 (e), (f), (g), and (h) show micrographs measured from samples M, N, O, and P (treated for 30, 60, 90, and 120 minutes in HNO_3, respectively). Sample M has the least amount of etching product for all samples treated in this batch for various HNO_3 treatment times studied with a constant amount of alkaline etching. This suggests that more BTSE should bond directly to the substrate compared to the other samples. Longer HNO_3-treatment times, on the other hand, produce samples with an increased amount of pitting, indicating that the oxide film must be dissolving and that the metal is attacked to form Al^{3+} ions and begin the creation of pits. The lower oxide-to-metal ratio seen in the XPS narrow scan for the 120-minute HNO_3-dipped sample (sample P) in Figure 4.6 (c) is consistent with the HNO_3 now acting as a corrosion agent.

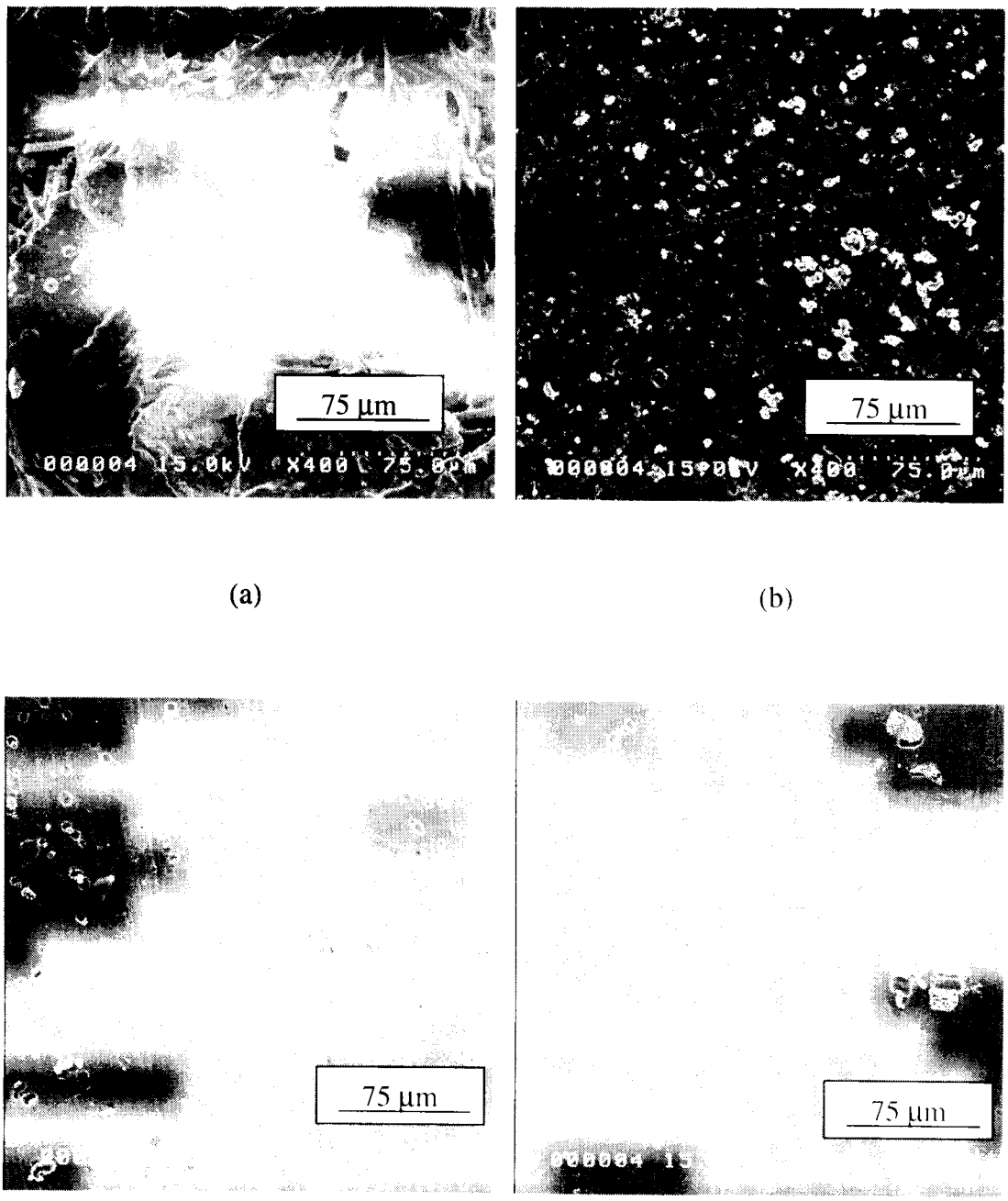

Figure 4.7 SEM micrographs of Al-2024 samples after various HNO_3 treatment times (400x) (a) A (0 min); (b) J (1 min); (c) K (10 min); (d) L (15 min)

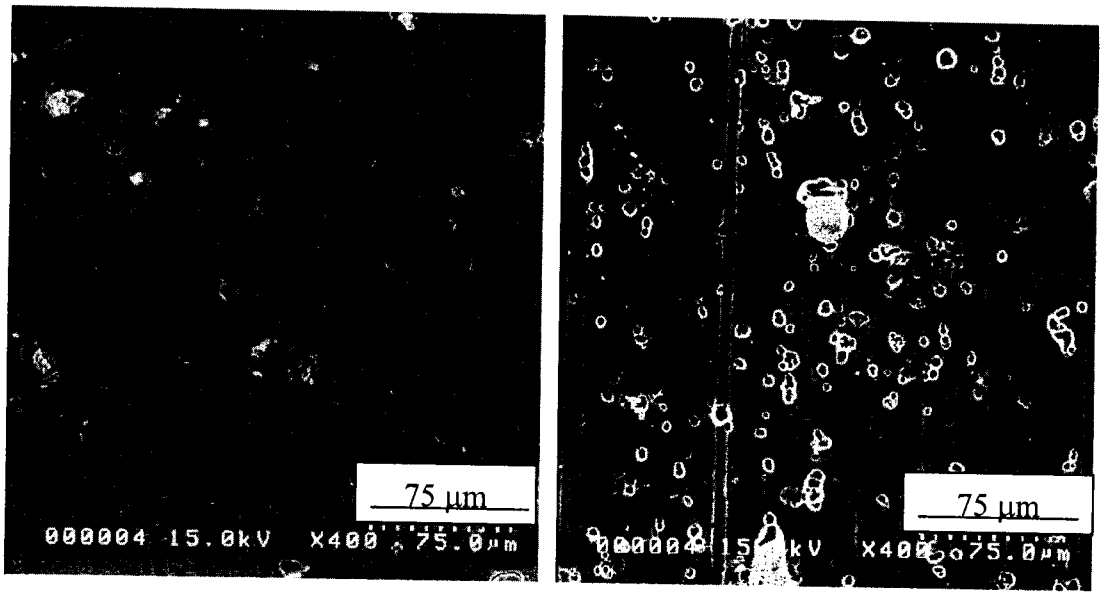

(e) (f)

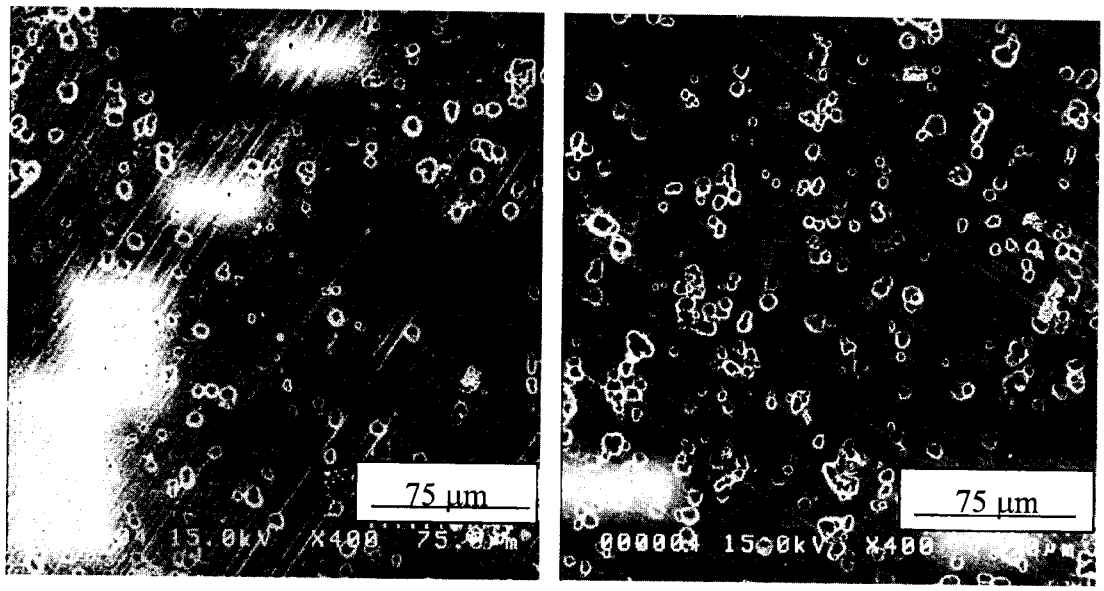

(g) (h)

Figure 4.7 SEM micrographs of Al-2024 with various HNO_3 treatment times (400x) continued (e) M (30 min); (f) N (60 min); (g) O (90 min); (h) P (120 min)

4.4.3 Discussion

The SEM micrographs in Section 4.4.2 appear to show less etching product on an uncoated Al-2024 substrate as the HNO_3 treatment time increases up to 30 minutes. Section 4.3.1 has shown that the amount of securely-bonded silane remaining after sonication also increases when the HNO_3 treatment time increases, again, up to 30 minutes. The trends from these two sections complement each other, and they are consistent with Hulser's theory that etching products act as nucleation sites for the coating. With less etching product on the surface, more silane can bond to hydroxyl groups in the oxide layer, rather than to the loosely-bound etching product. This is consistent with more silane remaining securely-bonded after the sonicating tests.

The anodizing effects of HNO_3 have also been demonstrated to increase the thickness and hardness of the passivating oxide layer with increasing treatment times [4.8, 4.11, 4.12]. In principle, that could provide an alternative to the current chromic acid anodizing processes. The HNO_3 treatment appears to create more hydroxyl sites in the oxide layer, and this should allow more silane bonding and better passivation. XPS results presented with the sonicating tests in Section 4.3.1 and for the uncoated alloy in Section 4.4.1 are consistent with this hypothesis.

However, HNO_3 is also a known corrosion agent for Al-Cu systems, where it may breakdown the oxide film, leaving the metal prone to acidic attack. This occurs independent of the HNO_3 concentration used when the metal is in unstirred conditions. This is a situation for these experiments and for metal pretreatments in many industrial processes [4.13 – 4.17]. For longer treatment times (e.g. 30 minutes in this work), HNO_3 acts as a corrosion agent, and the subsequently applied silane does not bond well to the

substrate. The etching caused by HNO_3 in a long treatment time produces a thinner oxide layer, removes bonding sites, and increases etching products on the surface. This hypothesis is consistent with results obtained in Section 4.4 for treatment times greater than 30 minutes. For example, XPS results (Section 4.4.1) show that sample P (120 minutes of HNO_3 treatment) has a thinner oxide layer than sample M (30 minutes of HNO_3 treatment). SEM micrographs (Section 4.4.2) show increased amounts of pitting and possible etching products for all HNO_3 treatments greater than 30 minutes. Section 4.3.1 demonstrated that the Si/Al ratio from XPS also decreases after 30 minutes of HNO_3 treatment. These observations together support the concept that for more than 30 minutes of treatment time, HNO_3 acts as a corrosion agent rather than as an anodizing agent. It is not yet clear why this balance between anodizing (forming a passivating oxide layer) and corrosion agent (breaking down the oxide) behaviour changes at the 30-minute mark for treatment in HNO_3. Similar observations, however, have been made by Shih and Tzou [4.8].

The pits created with longer HNO_3 treatment times increase the surface roughness of the sample. While other researchers have considered this to be important for the mechanical interlocking of organic or silane coatings to the substrate [4.18 – 4.20], the results in this chapter show that chemical bonding effects, dependant on the state of the oxide layer, are more important for creating a securely-bonded BTSE coating.
Finally, while polarisation curve measurements from Section 3.5 were less helpful, the results from this chapter offer a possible explanation to the question posed in Section 3.5 regarding the effectiveness of silane coatings deposited from the same silane solution for different alkaline etching times. It is known from Section 3.3 that increasing the alkaline

etching time increases the amount of etching product on the surface. XPS results from Sections 3.5 and 4.3 show that silane will bond to etching products on the surface.

However, XPS results from sonicating tests in Section 4.3 also show that this etching product, and any silane bonded to it, is easily removed with water thereby exposing the metal and leaving it prone to attack. This confirms the ideas presented by Hulser [4.4]. Thus, increasing the alkaline etching time, while enhancing silane deposition onto the substrate, is not beneficial to the passivation of the metal as it does not create a securely-bonded BTSE film on the metal. It is best to use a more-concentrated silane solution if a thicker coating is desired.

Chapter 5 Concluding Remarks and Future Directions

5.1 Concluding Remarks

The work presented in this thesis looked at an industrial-style alkaline etching process for Al-2024 alloy prior to silane deposition. The consequences and effects of the various stages in an alkaline etching process, as it pertains to silane deposition, have not been previously discussed in the literature. The objective of this work was to gain some new insight into this process, to observe how various pretreatment methods affect the corrosion performance of both the coated and uncoated alloy, and to possibly optimize this pretreatment method, if it is to be used for silane deposition, as suggested by Van Ooij [5.1 – 5.6].

The first study considered the effect of varying the alkaline etching time on the properties of an uncoated Al-2024 panel, with an emphasis on its surface chemistry, morphology, and corrosion resistance. Using a 10% (w/v) NaOH solution, separate etchings were carried out for 1, 3, and 10 minute durations; the first two represent typical etching times used in industry, while the final time represents an extreme case for comparison. The following trends were observed for increasing the etching time: (i) more pits and crevices were created, making a rougher surface; (ii) more etching product was created on the surface; (iii) copper enrichment on the surface increased; and finally, (iv) the corrosion resistance of the treated alloy decreased. It is not clear, however, whether the increase in susceptibility to corrosion was due to the morphological changes caused by the etching, or to chemical changes from the copper enrichment at the surface. Indeed, these two factors may reinforce each other.

The second parameter for study involved varying the concentration of the BTSE solution used to coat Al-2024 panels, which were first given a standardized 1 minute alkaline etch. This was done to observe what effects more-concentrated silane solutions have on the amount of silane deposited onto the substrate; and to measure the corrosion performance of the various coated samples. It is found, in general, that the BTSE coating aids in the passivation of the alloy. XPS results revealed that increasing the silane concentration created thicker coatings, with more silane being deposited onto the substrate. In addition, the corrosion resistance of the coated sample increases with the use of more-concentrated solutions. This demonstrates that thicker coatings on identically pretreated panels will increase the corrosion protection of the panel.

With the information gathered from the first two tasks, an attempt to study the interrelationship between alkaline etching and silane deposition was performed. These experiments provided new information showing that the method of pretreatment used greatly affects the deposition and performance of a silane film. A 1% BTSE solution was used to coat Al-2024 samples that had been alkaline etched for 1, 3, and 10 minute durations. XPS results showed that more silane was deposited on samples etched for longer times (e. g. 3 minutes vs. 1 minute). However, these "enhanced" coatings did not lead to better passivation of the substrate since the coatings were indicated to be attached to weakly-bound etching products, created by the longer alkaline etching times. When all of the results above are combined, it is concluded that shorter alkaline etching times (e. g. 1 minute vs. 3 or 10 minutes) should be used.

The next parameter studied was the length of HNO_3 treatment after the alkaline etching. In addition to its desmutting properties, HNO_3 is also known to build up the

thickness and hardness of the oxide layer. This will potentially affect the number of sites available for silane bonding. It was found that HNO_3 has a significant impact on the effectiveness of the deposited silane film. More silane will bond securely to the Al-2024 substrate when the amount of hydroxyl groups in the oxide layer is maximized, and the amount of loosely-bound etching product on the substrate, created by either the nitric acid or alkaline etching, is minimized. Increasing the nitric acid treatment time, up to 30 minutes for this system (alkaline etched for 1 minute), is shown to both remove much of the etching product created by the NaOH solution, and create a thicker oxide layer containing many sites for silane bonding. This layer appears to be greater than ~ 60 Å, according to XPS. Treatment times greater than 30 minutes, however, will remove the newly-formed oxide layer, leaving fewer sites available for silane bonding. This indicates that a balance is needed between the two roles that HNO_3 can play; and that not only fine-tuning the alkaline etching time, but also the HNO_3 treatment time, is important for an effective pretreatment prior to silane deposition.

The results presented in this thesis contribute information (from a chemical point of view) in the search for an appropriate pretreatment method for Al-2024 alloy as it relates to BTSE deposition. They also show how pretreatment significantly affects the chemical and morphological properties of the substrate. Both of these factors affect the subsequent deposition of the silane and ultimately the coating's performance. More importantly, this research supports Van Ooij's observations regarding the use of BTSE as a potential corrosion inhibitor for Al-2024. These studies together suggest that if appropriate pretreatment methods are used to prepare the Al-2024 substrate, BTSE has

the potential to be a green alternative to the current chromating and phosphating processes used for corrosion protection.

5.2 Future Directions

5.2.1 Further Studies on Copper Enrichment

The XPS study in this thesis shows that alkaline etching of Al-2024 alloy results in an increase in copper enrichment at the surface. It is also known that the corrosion rate of uncoated Al-2024 increases with the increasing alkaline etching time. However, it is not known to what degree the copper enrichment alone affects the corrosion rate; nor is it known how, or whether, copper enrichment affects the silane bonding. Further studies using panels that were not etched, but which contain varying amounts of copper, could be done using methods such as immersion testing, polarisation curve measurements, and sonicating, to assess the effects independently of morphology and etching product, on silane bonding and corrosion resistance. In addition, if copper enrichment is indeed a major factor in affecting the corrosion rate and silane bonding, research into an alternative method to optimize silane bonding, that does not cause alloy enrichment, is worth looking into.

5.2.2 Addition of a Second Silane

This thesis has demonstrated the potential of BTSE as a corrosion inhibitor. However, as mentioned in the previous chapters, BTSE lacks organofunctional groups which may be a reason why other authors have shown limited interest in this compound. Van Ooij and co-workers have published some papers dealing with adding subsequent coatings of different silanes such as VS and γ-APS to BTSE-coated panels [5.1 – 5.5].

However, the interface between two silanes has not been studied by these authors. Again, surface science experiments, (e.g. with SIMS depth profiling) would be useful to examine this silane-silane interface and to optimize the preparation and formation of a two-silane coating.

5.2.3 Evaluation of Coatings and Coating Effectiveness

Section 3.5 has shown the limitations of using only one technique for semi-quantitative measurement of the effects on corrosion performance due to different treatments. Other techniques, such as electrochemical impedance spectroscopy, salt-spray tests, and weight loss measurements, can be used to compare with the electrochemical polarisation curve measurements, in order to evaluate further the performances of the coatings formed. In addition, while the simple sonication tests performed in Chapter 4 provided information, in combination with XPS, for a semi-quantitative measure of the amount of securely-bonded silane, other techniques such as SIMS could be used to complement these results by offering direct evidence for the amount of silane bonding at the substrate surface.

5.2.4 Further Studies of Nitric Acid on Al-2024 Alloy

The balance between HNO_3 acting as an anodizing agent and as a corrosion agent has been demonstrated in Chapter 4 and reported elsewhere in the literature [5.7]. The factors that determine this balance are not well understood. Further studies of this phenomenon via surface science techniques would be beneficial, not only for the understanding of this mechanism, but also for optimizing its application to industrial processes, such as metal coating.

References

Chapter 1

[1.1] Wernick, S., Pinner, R., The Surface Treatment and Finishing of Aluminum and its Alloys, Robert Draper, Ltd.; Teddington (1972) 4th ed. Vol 1

[1.2] Callister, W. D., Materials Science and Engineering An Introduction, John Wiley and Sons; Toronto (1997) 4th ed.

[1.3] Wood, G. C., Sutton, W. H., Richardson, J. A., Riley, T. N. K., Malherbe, A. G., Proceeding Conference on Localized Corrosion, Huston (1974)

[1.4] Galvele, J. R., Corros. Sci. **21** (1981) 551

[1.5] Thompson, G. E., Doherty, P. E., Wood, G. C., J. Electrochem. Soc., **192** (1982) 1515

[1.6] Chawla, S. L., Gupta, R. K., Materials Selection for Corrosion Control, ASM International; Ohio (1993)

[1.7] Jones, D. A., Principles and Prevention of Corrosion, Prentice-Hall; New Jersey (1996) 2nd ed.

[1.8] Pourbaix, M., Atlas of Electrochemical Equilibria in Aqueous Solutions, NACE; Huston (1974)

[1.9] Bond, A. P., Bolling, G. F., Domian, H. A., Biloni, H., J. Electrochem. Soc., **113** (1966) 773

[1.10] Wu, X., Hebert, K., J. Electrochem. Soc., **143** (1996) 83

[1.11] Blestek, T., Webber, J., Conversion Coatings, C. R. Draper, ed., Portcullis Press; Redhill, (1976)

[1.12] Shier, L. L., Corrosion, Butterworth-Heinmann (1994) 3rd ed. Vol 2

[1.13] Stricklen, R., Mater.and Meth., **35** (1952) 91

[1.14] Foster, T., Blenkinsop, G. N., Blattler, P., Szandorowski, M., J. Coatings Technol., **66** (1991) 91

[1.15] Heung, W. F. Yang, Y. P., Zhou, M. Y., Wong, P. C., Mitchell, K. A. R., Foster, T., J. Mat. Sci., **29** (1994) 3653

[1.16] Ying, J. F., Flinn, B. J., Zhou, M. Y., Wong, P. C., Mitchell, K. A. R., Foster, T., Prog. Surf. Sci., **50** (1995) 259

[1.17] Leung, Y. L., Zhou, M. Y., Wong, P. C., Mitchell, K. A. R., Foster, T., Appl. Surf. Sci., **59** (1992) 23

[1.18] Ying, J. F., Zhou, M. Y., Flinn, B. J., Wong, P. C., Mitchell, K. A.R., Foster, T., J. Mat. Sci. **31** (1996) 565

[1.19] Sun, X., Kok, W. H., Wong, K. C., Li, R., Mitchell, K. A. R., Foster, T., ATB Metallurgie **40-41** (2001) 503

[1.20] Kok, W. H., Sun, X., Shi, L., Wong, K. C., Mitchell, K. A. R., Foster,T., J. Mat. Sci., **36** (2001) 3941

[1.21] Van Ooij, W. J., Sabata, A., J. Adhes. Sci. Technol., **5** (1991) 843

[1.22] Sundararajan, G. P., Van Ooij, W. J., Surf. Eng., **16** (2000) 315

[1.23] Leidheiser, H., De Costa, M., Granata, R. D., Corrosion **43** (1987) 382

[1.24] Van Ooij, W. J., Surf. Eng., **16** (2000) 385

[1.25] Puomi, P., Fagerholm, H. M, J. Adhes. Sci. Technol., **15** (2001) 869

[1.26] Subramanian, V., Van Ooij, W. J., Surf. Eng.,, **15** (1999) 168

[1.27] Matienzo, L. J., Shaffer, D. K., Moshier, W. C., Davis, G. D., J. Mat. Sci., **21** (1986) 1601

[1.28] Sabata, A., Van Ooij, W. J., Koch, R. J., J. Adhes. Sci. Technol.,**7** (1993) 1153

[1.29] Van Ooij, W. J., Sabata, A., Scand. J. Metall., **21** (1992) 32

[1.30] Waldman, B. A., Modern Paint and Coatings, (1996) 34

[1.31] Plueddemann, E. P., Silane Coupling Agents, Plenum Publishing Corp.; New York (1991) 2nd ed.

[1.32] Pape, P. G., Plueddemann, E. P., Eng. Plast., **6** (1993) 196

[1.33] Van Ooij, W. J., Child, T., Chemtech, **28** (1998) 26

[1.34] Boerio, F. J., Gosselin, C. A., Dillingham, R. G., Liu, H. W., J. Adhes., **13** (1981) 159

[1.35] Plato, Timaeus, R. D. Archer Hinds, ed., McMillan; London (1888)

[1.36] Plueddemann, E. P., Clark, H. A., Nelson, L. E., Hoffmann, K. R., Mod. Plast., **39** (1962) 136

[1.37] Allen, K. W., Hansrani, A. K., Wake, W. C., J. Adhes., **12** (1981) 199

[1.38] Rider, A. N., Arnott, D. R., Int. J. Adhes. Adhes., **20** (2000) 209

[1.39] Wu, H. F., Dwight, D. W., Huff, N. T., Compos. Sci. Technol., **57** (1997) 975

[1.40] Allen, K. W., Stevens, M. G., J. Adhes., **14** (1982) 137

[1.41] Cave, N. G., Kinloch, A. J., J. Adhes., **34** (1991) 175

[1.42] Lund, C. J., Murphy, P. D., J. Adhes. Sci. Technol., **6** (1992) 33

[1.43] Horner, M. R., Boerio, F. J.; Clearfield, H. M., J. Adhes. Sci. Technol., **6** (1992) 1

[1.44] Chiang, C. H., Koenig, J. L., J. Colloid Interface Sci., **83** (1981) 361

[1.45] Stralin, A., Hjertberg, T., J. Adhes., **41** (1993) 51

[1.46] Horr, T. J., Reynolds, G. D., J. Adhes. Sci. Technol., **11** (1997) 995

[1.47] Huang, Y, Yu, Y., Bell, J. P., J. Appl. Polym. Sci., **56** (1995) 1

[1.48] Subramanian, V., Van Ooij, W. J., Corrosion, **54** (1998) 204

[1.49] Hornstrom, S. E., Karlsson, J., Van Ooij, W. J., Tang, N., Klang, H. J. Adhes. Sci, Technol., **10** (1996) 883

[1.50] Lu, F., Van Ooij, W. J., Acta Metall. Sin., **12** (1999) 221

[1.51] Ghiazza, M., Beccaria, A. M., Poggi, G, Castello, G, Br. Corros. J., **29** (1994) 210

[1.52] Kono, M., Sun, X., Li, R., Wong, K. C., Mitchell, K. A. R., Foster, T., Surf. Rev. Lett., **8** (2001) 43

[1.53] Van Ooij, W. J., Zhang, C., Zhang, J. Q., Yuan, W., Electrochemical Society Proceedings, **97** (1998) 222

[1.54] Tang, N., Van Ooij, W. J., Gorecki, G., Prog. Org. Coat., **30** (1997) 255

[1.55] Pu, Z., Van Ooij, W. J., Mark, J. E., J. Adhes. Sci. Technol., **11** (1997) 29

[1.56] Child, T. F., Van Ooij, W. J., Trans. IMF, **77** (1999) 64

[1.57] Sabata, A., Knueppel, B. A., Van Ooij, W. J., J. Test. Eval., **23** (1995) 119

[1.58] Treverton, J. A., Thomas, M. P., Int. J. Adhes. Adhes., **9** (1989) 211

[1.59] Bishopp, J. A., Sim, E. K., Thompson, G. E., Wood, G. C., Adhesion 13, Ed. K. W. Allen, (1989) 201

[1.60] Venables, J. D., McNamara, D. K., Chen, J. M., Sun, T. S., Hopping, R. L., App. Surf. Sci., **3** (1979) 88

[1.61] Kozma, L., Olefjord, I., Mater. Sci. Technol., **3** (1987) 860

[1.62] Critchlow, G. W., Brewis, D. M., Int. J. Adhes. Adhes., **16** (1996) 355

[1.63] Digby, R. P., Packham, D. E., Int. J. Adhes. Adhes., **15** (1995) 61

[1.64] Pires, I., Quintino, L., Rangel, C. M., Thompson, G. E., Skeldon, P., Zhou, X., Trans IMF, **78** (2000) 179

[1.65] De Rosa, R. L., Grant, J. T., Katsen, L., Donley, M., Bierwagen, G. P., Corrosion, **56** (2000) 395

[1.66] Hulser, P., Kruger, U. A., Beck, F., Corr. Sci., **38** (1996) 47

[1.67] Ijomah, M. N. C., Indian J. Tech., **27** (1989) 9

Chapter 2

[2.1] Ratner, B.D., Castner, D., Electron Spectroscopy for Chemical Analysis, Vickerman, J. C., ed., John Wiley and Sons; Toronto (1997)

[2.2] Andrade, J. D., Surface and Interfacial Aspects of Biomedical Polymers, Plenum Press; New York (1985)

[2.3] Wagner, C. D., Riggs, W. M., Davis, L. E., Moulder, J. F., Handbook of X-Ray Photoelectron Spectroscopy, Ed. G. E. Muilenberg, Perkin-Elmer Corp., Physical Electronics Division (1979)

[2.4] Walls, J. M., Christie, A. B., Surface Analysis by Auger and X-Ray Photoelectron Spectrscopy, Brewis, D. M., ed., Applied Science Publishers; London (1982)

[2.5] Briggs, D., Seah, M. P., Practical Surface Analysis, John Wiley and Sons Ltd., West Sussex (1990) 2nd ed.

[2.6] Attard, G., Barnes, C., Surfaces, Oxford University Press; Toronto (1998)

[2.7] MAX 200 User Manual, Leybold, Koln

[2.8] Seah, M. P., Dench, W. A., Surf. Interface Anal., **1** (1979) 2

[2.9] Somorjai, G. A., Chemistry in Two-Dimentions: Surfaces, Cornell University; Ithaca (1981)

[2.10] Susac, D., Interfaces for Polymer Light Emitting Diodes, M. Sc. Thesis, UBC (1999)

[2.11] Leung, Y. L., XPS Studies of Silane/Aluminum Interfaces, M. Sc. Thesis, UBC (1992)

[2.12] Shirley, D. A., Phys. Rev. B., **5** (1972) 4709

[2.13] http://www.phy.cuhk.edu.hk/~surface/XPSPEAK/

[2.14] Cowley, J. M., Electron Microscopy, Hubbard, A. T., ed., CRC Press Inc.; Boca Raton (1995)

[2.15] Dykstra, M. J., Biological Electron Microscopy: Theory, Techniques, and Troubleshooting, Plenum Press, New York (1992)

[2.16] Shi, L., Zinc Phosphating on 6061-T6 Aluminum Alloy, M. Sc. Thesis, UBC (2000)

[2.17] Black, J. T., Principles and Techniques of Scanning Electron Microscopy, Hayat, M. A., ed., Van Nostrand Reinhold Co., Toronto (1974)

[2.18] Attard, G., Barnes, C., Surfaces, Oxford University Press; Toronto (1998)

[2.19] Wells, O. C., Scanning Electron Microscopy, McGraw-Hill Book Co.; New York (1974)

[2.20] Flegler, S. L., Heckman, J. W., Jr., Klomparens, K. L., Scanning and Transmission Electron Microscopy An Introduction, W. H. Freeman and Co.; New York (1993)

[2.21] Tromans, D., MMAT 456 Course Lecture Notes, (2000)

[2.22] Hitachi S4100 User's Manual

[2.23] Goldstein, J. I., Newbury, D. E., Echlin, P., Joy, D. C., Romig, A. D., Lyman, C. E., Fiori, C., Lifshin, E., Scanning Electron Microscopy and X-Ray Microanalysis 2nd Edition, Plenum Press; New York (1992)

[2.24] Jones, D. A., Principles and Prevention of Corrosion, Prentice-Hall; New Jersey (1996) 2nd ed.

[2.25] Bard, A. J., Faulkner, L. R., Electrochemical Methods: Fundamentals and Applications, John Wiley and Sons; New York (1980)

[2.26] Trethewey, K. R., et al, Corrosion for Science and Engineering, Longman Ltd.; Essex (1995) 2nd ed.

[2.27] Butler, J. A. V., Trans. Faraday Soc., **19** (1924) 734

[2.28] Fisher, A. C., Electrode Dynamics, Oxford University Press; New York (1996)

[2.29] Tafel, J., Z. Physik Chem, **50** (1905) 641

[2.30] Fontana, M. G., Corrosion Engineering, McGraw-Hill Book Co.; Toronto (1987) 3rd ed.

[2.31] Scully, J. C., The Fundamentals of Corrosion, Pergamon Press; Toronto (1990) 3rd ed.

Chapter 3

[3.1] Child, T. F., Van Ooij, W. J., Trans. IMF, **77** (1999) 64

[3.2] Van Ooij, W. J., Child, T., Chemtech, **28** (1998) 26

[3.3] Sabata, A., Knueppel, B. A., Van Ooij, W. J., J. Test. Eval., **23** (1995) 119

[3.4] Pu, Z., Van Ooij, W. J., Mark, J. E., J. Adhes. Sci. Technol., **11** (1997) 29

[3.5] Cave, N. G., Kinlock, A. J., J. Adhes., **34** (1991) 175

[3.6] Allen, K. W., Hansrani, A. K., Wake, W. C., J. Adhes., **12** (1981) 199

[3.7] Boerio, F. J., Gosselin, C. A., Williams, J. W., Dillingham, R. G., Burkstrand, J. M., Molecular Characterization of Composite Interfaces, Ed. H. Ishida, G. Kumar, (1983) 171

[3.8] Quinton, J. S., Dastoor, P. C., Surf. Interface Anal., **30** (2000) 21

[3.9] Boerio, F. J., Gosselin, C. A., Dillingham, R. G., Liu, H. W., J. Adhes., **13** (1981) 159

[3.10] Underhill, P. R., Goring, G., DuQuesnay, D. L., Int. J. Adhes. Adhes., **20** (2000) 195

[3.11] Underhill, P. R., Goring, G., DuQuesnay, D. L., Int. J. Adhes. Adhes., **18** (1998) 313

[3.12] Underhill, P. R., Goring, G., DuQuesnay, D. L., App. Surf. Sci., **134** (1998) 247

[3.13] Digby, R. P., Shaw, S. J., Int. J. Adhes. Adhes., **18** (1998) 261

[3.14] Riegal, B., Blittersdorf, S., Kiefer, W., Hofacker, S., Muller, M., Schottner, G., J. Non-Cryst. Solids, **226** (1998) 76

[3.15] Wernick, S., Pinner, R., The Surface Treatment and Finishing of Aluminum and its Alloys, Robert Draper, Ltd.; Teddington (1972) 4th ed. Vol 1

[3.16] Li, R., M. Sc. Thesis, UMIST (1998)

[3.17] Wagner, C. D., Riggs, W. M., Davis, L. E., Moulder, J. F., Handbook of X-Ray Photoelectron Spectroscopy, Ed. G. E. Muilenberg, Perkin-Elmer Corp., Physical Electronics Division (1979)

[3.18] Wu, X., Hebert, K., J. Electrochem. Soc., **143** (1996) 83

[3.19] Dimitrov, N., Mann, J. A., Sieradzki, K., J. Electrochem. Soc., **146** (1999) 98

[3.20] Zhou, X., Thompson, G. E., Habazaki, H., Shimizu, K., Skeldon, P., Wood, G. C., Thin Solid Films, **293** (1997) 327

[3.21] Bond, A. P., Bolling, G. F., Domian, H. A., Biloni, H., J. Electrochem. Soc., **113** (1966) 773

[3.22] Hulser, P., Kruger, U. A., Beck, F., Corr. Sci., **38** (1996) 47

[3.23] Ijomah, M. N. C., Indian J. Tech., **27** (1989) 9

[3.24] Pires, I., Quintino, L., Rangel, C. M., Thompson, G. E., Skeldon, P., Zhou, X., Trans IMF, **78** (2000) 179

[3.25] Bishopp, J. A., Sim, E. K., Thompson, G. E., Wood, G. C., Adhesion 13, Ed. K. W. Allen, (1989) 201

[3.26] Fontana, M. G., Corrosion Engineering, McGraw-Hill Book Co.; Toronto (1987) 3rd ed.

[3.27] Venables, J. D., McNamara, D. K., Chen, J. M., Sun, T. S., Hopping, R. L., App. Surf. Sci., **3** (1979) 88

[3.28] Subramanian, V., Van Ooij, W. J., Corrosion, **54** (1998) 204

[3.29] Hornstrom, S. E., Karlsson, J., Van Ooij, W. J., Tang, N., Klang, H. J. Adhes. Sci, Technol., **10** (1996) 883

[3.30] Lu, F., Van Ooij, W. J., Acta Metall. Sin., **12** (1999) 221

[3.31] Van Ooij, W. J., Zhang, C., Zhang, J. Q., Yuan, W., Electrochemical Society Proceedings, **97** (1998) 222

[3.32] Tang, N., Van Ooij, W. J., Gorecki, G., Prog. Org. Coat., **30** (1997) 255

[3.33] Van Ooij, W. J., Song, J., Subramanian, V., ATB Metallurgie, **40-41** (2000-2001) 503

Chapter 4

[4.1] Plueddemann, E. P., Silane Coupling Agents, Plenum Publishing Corp.; New York (1991) 2nd ed.

[4.2] Pape, P. G., Plueddemann, E. P., Eng. Plast., **6** (1993) 196

[4.3] Van Ooij, W. J., Child, T., Chemtech, **28** (1998) 26

[4.4] Hulser, P., Kruger, U. A., Beck, F., Corr. Sci., **38** (1996) 47

[4.5] Ijomah, M. N. C., Indian J. Tech., **27** (1989) 9

[4.6] Wernick, S., Pinner, R., The Surface Treatment and Finishing of Aluminum and its Alloys, Robert Draper, Ltd.; Teddington (1972) 4th ed. Vol 1

[4.7] Pires, I., Quintino, L., Rangel, C. M., Thompson, G. E., Skeldon, P., Zhou, X., Trans IMF, **78** (2000) 179

[4.8] Shih, H. H., Tzou, S. L., Surf. Coat. Technol., **124** (2000) 278

[4.9] Wagner, C. D., Riggs, W. M., Davis, L. E., Moulder, J. F., Handbook of X-Ray Photoelectron Spectroscopy, Ed. G. E. Muilenberg, Perkin-Elmer Corp., Physical Electronics Division (1979)

[4.10] Briggs, D., Seah, M. P., Practical Surface Analysis, John Wiley and Sons Ltd., West Sussex (1990) 2nd ed.

[4.11] Lee, S. M., Pyun, S. I., J. Appl. Electrochem., **22** (1992) 151

[4.12] Nelson, K. J. H., Hughes, A. E., Taylor, R. J., Hinton, B. R. W., Wilson, L., Henderson, M., Mater. Sci. Technol., **17** (2001) 1211

[4.13] Al-Kharafi, F. M., Badawy, W. A., Indian J. Chem. Technol., **3** (1996) 212

[4.14] Chen, C., Mansfeld, F., Corr. Sci., **39** (1997) 1075

[4.15] Al-Kharafi, F. M., Badawy, W. A., Kuwait J. Sci. Eng., **24** (1997) 93

[4.16] Badawy, W. A., Al-Kharafi, F. M., Bull. Electrochem., **11** (1995) 505

[4.17] Fouda, A. S., Gouda, M. M., Abd El-Rahman, S. I., Bull. Korean Chem. Soc., **21** (2000) 1085

[4.18] Venables, J. D., McNamara, D. K., Chen, J. M., Sun, T. S., Hopping, R. L., App. Surf. Sci., **3** (1979) 88

[4.19] Kozma, L., Olefjord, I., Mater. Sci. Technol., **3** (1987) 860

[4.20] Kono, M., Sun, X., Li, R., Wong, K. C., Mitchell, K. A. R., Foster, T., Surf. Rev. Lett., **8** (2001) 43

Chapter 5

[5.1] Subramanian, V., Van Ooij, W. J., Corrosion, **54** (1998) 204

[5.2] Hornstrom, S. E., Karlsson, J., Van Ooij, W. J., Tang, N., Klang, H. J. Adhes. Sci, Technol., **10** (1996) 883

[5.3] Lu, F., Van Ooij, W. J., Acta Metall. Sin., **12** (1999) 221

[5.4] Van Ooij, W. J., Zhang, C., Zhang, J. Q., Yuan, W., Electrochemical Society Proceedings, **97** (1998) 222

[5.5] Tang, N., Van Ooij, W. J., Gorecki, G., Prog. Org. Coat., **30** (1997) 255

[5.6] Van Ooij, W. J., Song, J., Subramanian, V., ATB Metallurgie, **40-41** (2000-2001) 503

[5.7] Shih, H. H., Tzou, S. L., Surf. Coat. Technol., **124** (2000) 278